Post-starburst galaxies in simulations and observations

Yirui Zheng

A thesis submitted for the degree of PhD
at the
University of St Andrews

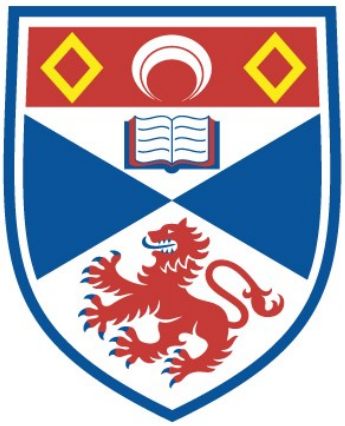

2022

Declaration

Candidate's declaration

I, Yirui Zheng, do hereby certify that this thesis, submitted for the degree of PhD, which is approximately 40,000 words in length, has been written by me, and that it is the record of work carried out by me, or principally by myself in collaboration with others as acknowledged, and that it has not been submitted in any previous application for any degree. I confirm that any appendices included in my thesis contain only material permitted by the 'Assessment of Postgraduate Research Students' policy.

I was admitted as a research student at the University of St Andrews in August 2017.

I received funding from an organisation or institution and have acknowledged the funder(s) in the full text of my thesis.

Date 26/08/2021 Signature of candidate

Supervisor's declaration

I hereby certify that the candidate has fulfilled the conditions of the Resolution and Regulations appropriate for the degree of PhD in the University of St Andrews and that the candidate is qualified to submit this thesis in application for that degree. I confirm that any appendices included in the thesis contain only material permitted by the 'Assessment of Postgraduate Research Students' policy.

Date 26/08/2021 Signature of supervisor

Permission for publication

In submitting this thesis to the University of St Andrews we understand that we are giving permission for it to be made available for use in accordance with the regulations of the University Library for the time being in force, subject to any copyright vested in the work not being affected thereby. We also understand, unless exempt by an award of an embargo as requested below, that the title and the abstract will be published, and that a copy of the work may be made and supplied to any bona fide library or research worker, that this thesis will be electronically accessible for personal or research use and that the library has the right to migrate this thesis into new electronic forms as required to ensure continued access to the thesis.

I, Yirui Zheng, confirm that my thesis does not contain any third-party material that requires copyright clearance.

The following is an agreed request by candidate and supervisor regarding the publication of this thesis:

Printed copy

No embargo on print copy.

Electronic copy

No embargo on electronic copy.

Date 26/08/2021 Signature of candidate

Date 26/08/2021 Signature of supervisor

Underpinning Research Data or Digital Outputs

Candidate's declaration

I, Yirui Zheng, understand that by declaring that I have original research data or digital outputs, I should make every effort in meeting the University's and research funders' requirements on the deposit and sharing of research data or research digital outputs.

Date 26/08/2021 Signature of candidate

Permission for publication of underpinning research data or digital outputs

We understand that for any original research data or digital outputs which are deposited, we are giving permission for them to be made available for use in accordance with the requirements of the University and research funders, for the time being in force.

We also understand that the title and the description will be published, and that the underpinning research data or digital outputs will be electronically accessible for use in accordance with the license specified at the point of deposit, unless exempt by award of an embargo as requested below.

The following is an agreed request by candidate and supervisor regarding the publication of underpinning research data or digital outputs: No embargo on underpinning research data or digital outputs.

Date 26/08/2021 Signature of candidate

Date 26/08/2021 Signature of supervisor

Abstract

Post-starburst (PSB) galaxies are the galaxies in which star formation has recently been sharply truncated, as indicated by strong Balmer absorption lines alongside weak or absent nebular emission lines. PSBs are believed to be an important transitional state between the star-forming and quiescent populations, and could be important candidates for the "fast" quenching route. From observations alone, it is challenging to figure out what mechanisms produce PSBs and how important PSBs are to the growth of the red sequence. Combining simulations and observations is one of the most important methodologies to answers these questions.

In this thesis, I run a set of binary merger simulations, with a variety of black hole feedback models, progenitor galaxies, orbits and mass ratios, to reproduce PSBs. I find that only major mergers on prograde-prograde or retrograde-prograde orbits in combination with a mechanical black hole feedback model can form galaxies that can be selected by the traditional PSB selection method. The difficulty in reproducing the very young PSBs in simulations potentially indicates that new sub-resolution star formation recipes are required to properly model the process of star formation quenching. I develop the SEDmorph code to create mock datacubes of the simulated galaxies, in order to investigate the radial gradients in the spectral indices of PSBs. In my simulations, I find the gradients are caused by the fact that the starburst peaks at the same time at all radii, but is stronger and more prolonged in the inner regions.

To find out the contribution of the fast quenching route to the growth of the red sequence, I study the population of rapidly quenched galaxies (RQGs) in the SIMBA cosmological hydrodynamic simulation at $0.5 < z < 2$, comparing directly to observational PSBs in the UKIDSS Ultra Deep Survey via their colour distributions and mass functions. I find that the fraction of quiescent galaxies that are rapidly quenched in SIMBA is 59% (or 48% in terms of stellar mass), which is higher than observed. A similar "downsizing" of RQGs is observed in both SIMBA and the UDS, with RQGs at higher redshift having a higher average mass. However, SIMBA produces too many RQGs at $1 < z_q < 1.5$ and too few low mass RQGs at $0.5 < z_q < 1$. SIMBA also shows various inconsistencies in star formation and chemical enrichment histories, including an absence of short, intense starbursts. These results will help inform the next generation of galaxy evolution models, particularly with respect to the quenching mechanisms employed.

Acknowledgements

General acknowledgements

I would firstly like to thank my supervisor, Vivienne Wild, for her unparalleled support and guidance throughout the project. Vivienne has been so helpful, nice, and patient for the past four years. I have benefited so much from her, both in work and life. She sets an example of an excellent researcher for me. It is really my fortune to have her as the supervisor.

I would like to thank my collaborators, including Peter H. Johansson, Romeel Dave, Natalia Lahén, David Law, Francisco Rodríguez Montero, John R. Weaver, Noelia Jimenez, Ena Choi, Ariel Werle and many others. This project would not be done properly without their help. Special thanks go out to Prof. Peter H. Johansson and Prof. Romeel Dave: Peter supervised me when I visit the University of Helsinki and Romeel supervised me when Vivienne is on maternity leave.

I would love to thank everyone in the astronomy group at St Andrews. You are the greatest colleagues in the world. I do enjoy your company in these four years. Special thanks go out to Dr Anne-Marie Weijmans for taking care of me when Vivienne is on maternity leave. Carl Roberts, Carolina Villarreal D'Angelo, Chris Duckworth, Dominic Bates, Dominic Samra, and Oliver Herbort, you guys are mentioned as we had so many great chats together.

Mr Wei Xu and Mr Jianbo Zhou put a seed in my heart, that's why I become an (Astro)physicist. Thank you! Prof. Xufen Wu supervised my senior project four years ago and continue encouraging my research and providing supports during my PhD project. You opened the door of astronomy for me!

I would love to thank my friends. You guys give me four colourful years in St Andrews. Wenbo Li and Ying Cheng helped me settling down in St Andrews, they are also my greatest flatmates. Meng Yang, Suinan Zhang, and Xiao Zheng, you are far beyond colleagues to me, I think it is better to thank you here. I do appreciate your help and enjoy the time with you.

Finally, I would like to thank my parents and my brothers. It would be impossible for me to complete this project without their support. With the deepest love, this thesis is dedicated to you. Thank you!

Funding

My postgraduate study was supported by the China Scholarship Council-University of St Andrews Scholarships (PhD programmes) [File No. 201703780003].

My research in this thesis received grant from the Scottish Universities Physics Alliance [Postdoctoral and Early Career Researcher Exchange Program] and the European Research Council Starting Grant SEDMorph (P.I. V. Wild). Besides, I am supported by the SDSS grant, to which the University of St Andrews contributes via the United Kingdom Participation Group.

Funding for the Sloan Digital Sky Survey IV has been provided by the Alfred P. Sloan Foundation, the U.S. Department of Energy Office of Science, and the Participating Institutions. SDSS-IV acknowledges support and resources from the Center for High-Performance Computing at the University of Utah. The SDSS web site is www.sdss.org.

SDSS-IV is managed by the Astrophysical Research Consortium for the Participating Institutions of the SDSS Collaboration including the Brazilian Participation Group, the Carnegie Institution for Science, Carnegie Mellon University, the Chilean Participation Group, the French Participation Group, Harvard-Smithsonian Center for Astrophysics, Instituto de Astrofísica de Canarias, The Johns Hopkins University, Kavli Institute for the Physics and Mathematics of the Universe (IPMU) / University of Tokyo, the Korean Participation Group, Lawrence Berkeley National Laboratory, Leibniz Institut für Astrophysik Potsdam (AIP), Max-Planck-Institut für Astronomie (MPIA Heidelberg), Max-Planck-Institut für Astrophysik (MPA Garching), Max-Planck-Institut für Extraterrestrische Physik (MPE), National Astronomical Observatories of China, New Mexico State University, New York University, University of Notre Dame, Observatário Nacional / MCTI, The Ohio State University, Pennsylvania State University, Shanghai Astronomical Observatory, United Kingdom Participation Group, Universidad Nacional Autónoma de México, University of Arizona, University of Colorado Boulder, University of Oxford, University of Portsmouth, University of Utah, University of Virginia, University of Washington, University of Wisconsin, Vanderbilt University, and Yale University.

Research Data/Digital Outputs access statement

- The related binary merger simulation data, including snapshots, black hole activity, mock spectra and mock MaNGA datacube are available at `https://doi.org/10.17630/ff244265-6540-494e-af3e-0969fdc5ff24`.
- The related MaNGA data used in Chapter 4 are available at the SDSS data base(`https://www.sdss.org/dr16/`).
- The SEDMorph code is available at `https://github.com/SEDMORPH`. My code for mock

datacube creation is available at https://github.com/SEDMORPH/YZCube.

- The SDSS DR7 galaxy data in PC1-PC2 space are available at http://www-star.st-andrews.ac.uk/~vw8/downloads/DR7PCA.html
- Research data underpinning Chapter 5 are available at: https://doi.org/10.17630/3d5bbf39-fe0a-4997-987c-d2407f791118. The data include the SFHs and super-colours of the SIMBA galaxies, and the alternative super-colour data computed with pseudo-burst or with BC03 SPS model.
- The SIMBA galaxy catalogue and photometry data are available at http://simba.roe.ac.uk/simdata/m100n1024/s50/catalogs/

Contents

List of Figures

List of Tables

1

INTRODUCTION

Galaxies are the bridge between the universe and the stars. Figuring out galaxy formation and evolution helps us understand not only galaxies themselves but also the universe they live in and the stars they host. How galaxies shut down their star formation and migrate onto the red sequence is one of the key problems in astrophysics. A crucial part of this puzzle is to understand the galaxy quenching mechanisms and the transiting galaxy populations (e.g., post-starburst galaxies, PSBs). Analysis of the star formation histories (SFHs) of quiescent galaxies has revealed at least two different quenching mechanisms that operate on different timescales, fast and slow quenching. While observations provide the ground truths for galaxy quenching problems, simulations work as a great tool to interpret observations, constrain theories, and understand galaxies and the Universe. Combining simulations and observations is one of the most important methodologies for astronomy research.

1.1 Galaxy evolution

Galaxies in the local Universe display a strong bimodality in the colour-magnitude diagram (Baldry et al., 2004; Schawinski et al., 2014)), which is illustrated in Figure 1.1 Most massive galaxies in the local Universe can be classified into two distinct groups: the red sequence (quiescent, elliptical galaxies) and the blue cloud (star-forming, spiral galaxies), with a small population populating the green valley, the intermediate region in the colour-magnitude diagram. However, it should be noted that there are exceptions like blue ellipticals and red spirals (see e.g. Schawinski et al., 2009; Masters et al., 2010)

The galaxies in the red sequence are different from those in the blue cloud in many aspects. The red sequence galaxies tend to have morphologies of earlier types (ellipticals or lenticulars), while blue cloud galaxies are usually in morphologies of late types featuring a rotating disc, a spiral structure, and a more or less prominent bulge. The red galaxies are usually gas-poor with little/no star formation, occupying the high-mass galaxy population, while the blue galaxies are usually gas-rich with active star formation, dominating the low-mass galaxy population. In terms of stellar populations, the red sequence galaxies are dominated by older, low-mass stars, resulting red colours, very little UV flux and strong 4000 Å break, which blue cloud galaxies have more younger, high-mass stars, leading to the blue optical colour, strong UV flux, strong Lyman and Balmer breaks. As for kinematical properties, the red early-type galaxies are supported by the random motion of stars with high velocity dispersion, although also have rotating components. 1/3 of local early-type galaxies are confirmed to be slow rotators and the remaining 2/3 are actually fast rotators (Cappellari et al., 2011; Emsellem et al., 2011). In contrast, star-forming late-type galaxies are generally dominated by ordered rotation.

The galaxy bimodality is found at both lower redshifts (e.g. Baldry et al., 2004; Schawinski et al., 2014) and higher redshifts (e.g. Williams et al., 2009; Brammer et al., 2011) but dominant galaxy types are different. The early-type galaxies dominate the high-stellar mass galaxies at the lower redshift but their relative number density decreases with the increasing redshift. The early-type galaxies lose the dominating role around $z \sim 1$: the late-type galaxies start to dominate the high-mass end. At the low-mass end, the population of quiescent galaxies also shows a decreasing trend at higher redshift, as a result, the star-forming galaxies dominate the stellar function at all masses at $z > 2.5$ (Muzzin et al., 2013).

The importance of quiescent galaxies shows a similar trend to the early-type galaxies when

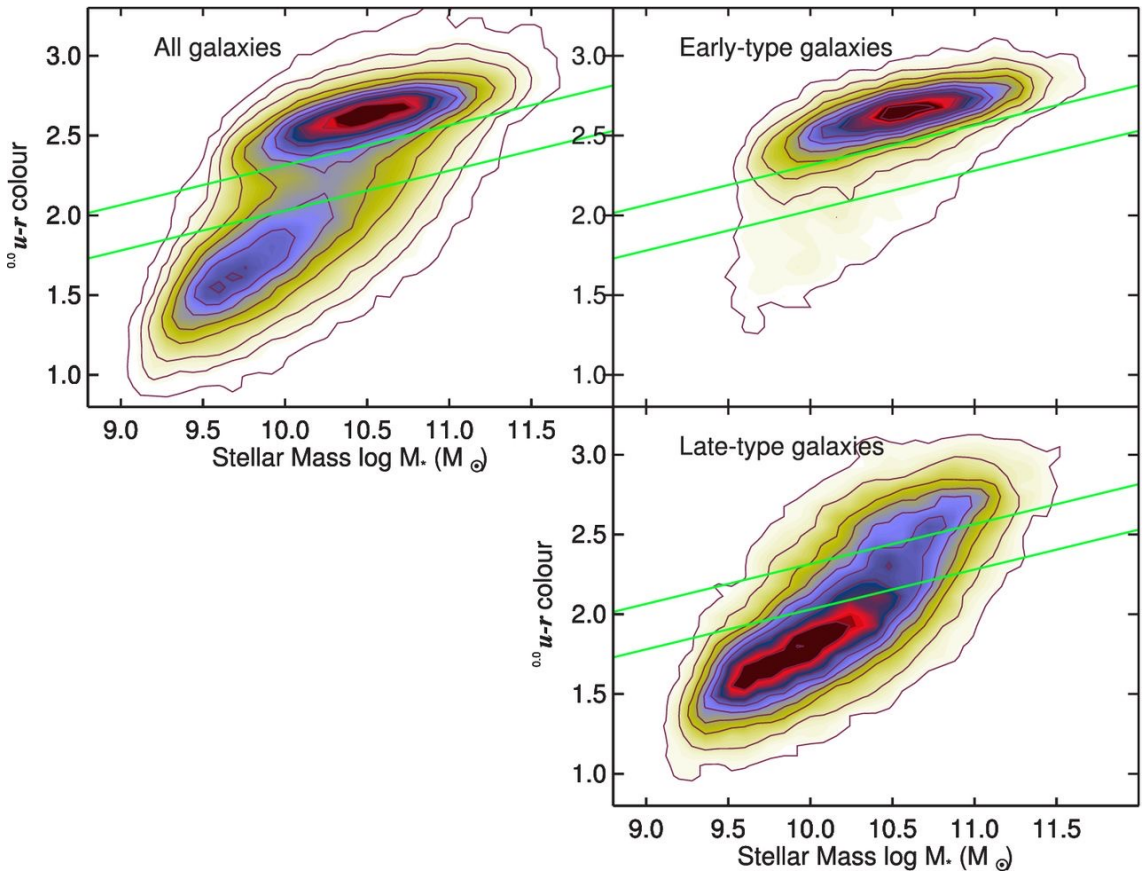

Figure 1.1: The $u-r$ colour–mass diagram for a SDSS sample (with $0.02 < z < 0.05$ and $M_z < -19.5$) discussed in Schawinski et al. (2014). The left-top panel shows all galaxies in the sample while the right panels show the subsamples of early-type galaxies (right-top) and late-type ones (right-bottom). The galaxies show a clear bimodality distribution in $u-r$ colour-mass space as seen in the left-top panel. Most of the early-type galaxies lie in the red sequence with a long tail extending to the blue cloud at lower stellar masses. The contours on this figure are linear and scaled to the highest value in each panel. Figure obtained from Schawinski et al. (2014)

considering the redshift evolution. The quiescent galaxies make up the majority of the high-mass population in the local universe but their dominating role is challenged at higher redshift: at $z = 1-2$, the star-forming galaxies contribute to about a half of the most luminous objects Williams et al. (2009). As for stars, observations have also revealed results that the total number of stars that live in quiescent galaxies (i.e. the total stellar mass), as well as the total number of quiescent galaxies, continue to increase since a redshift of $z \sim 1$; in contrast, the stellar mass density of star-forming galaxies remains almost constant (see Figure 1.2 and related papers: Bell et al., 2004; Ilbert et al., 2013; Muzzin et al., 2013). Quiescent galaxies have little in-situ star formation activity, thus, the steady growth of the red sequence implies a steady conversion of star-forming galaxies into quiescent ones.

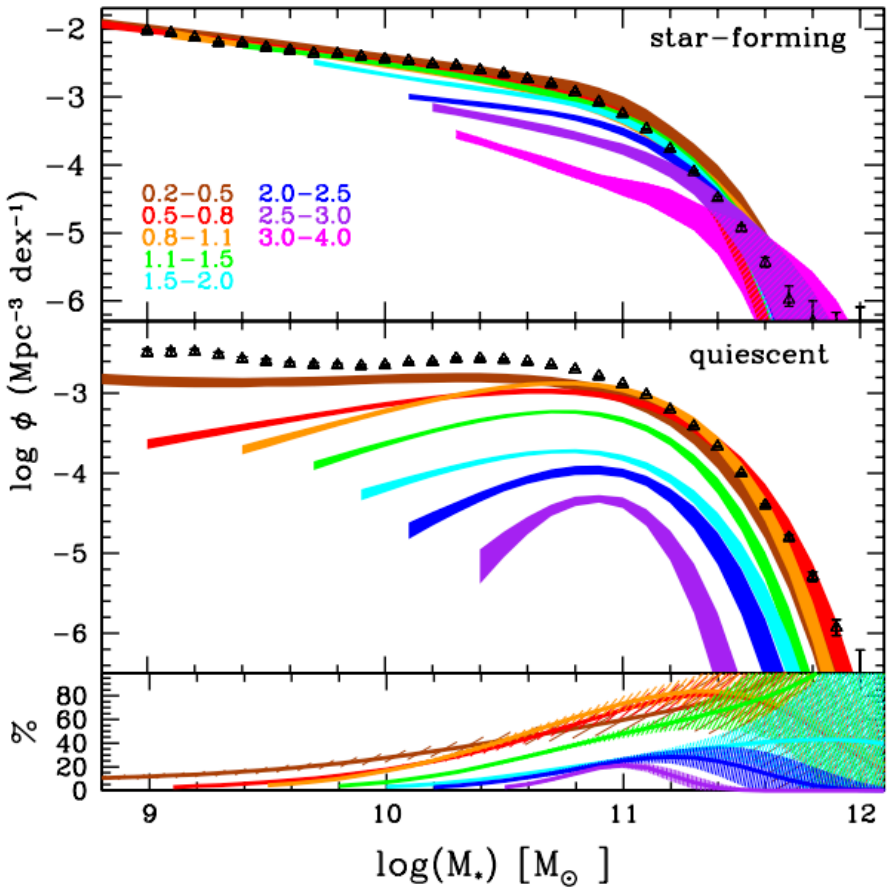

Figure 1.2: Galaxy stellar mass function up to z = 4 for the star-forming population (top panel) and for the quiescent population (middle panel). Each colour represents a redshift bin of variable step size with the exact values shown in the top panel. The number density of star-forming galaxies remains almost constant since a redshift of $z \sim 1$, while the total number of quiescent galaxies continues to increase. The bottom panel shows the percentage of quiescent galaxies as a function of stellar mass in the same redshift bins. Figure obtained from Ilbert et al. (2013).

The discussion above has showed strong evidences of the conversion of star-forming galax-

ies into quiescent ones. However, how and why galaxies shut off their star formation and build up the red sequence remains unclear. A natural idea is that the star-forming galaxies deplete their gas supply and the star formation is gradually quenched. As shown in Figure 1.3, the Universe's global star formation rate density has declined by a factor of ~ 10 since $z \sim 2$ (Madau & Dickinson, 2014), and as the number density of star-forming galaxies has remained relatively constant during the same time, this strongly indicates that typical star-forming galaxies are gradually decreasing their star formation rate over the past several billion years (Gyr). However, morphological observations suggest that gas depletion is probably **not** the dominant quenching mechanism. A blue spiral galaxy is unlikely to experience a morphological transformation when it is quenched by simple gas depletion, while observations reveal a strong correlation between quiescent galaxies and a predominantly spheroid morphology at all redshifts (e.g. Bell et al., 2012; Lang et al., 2014; Bruce et al., 2014; Brennan et al., 2015; Ownsworth et al., 2016). Meanwhile, simple gas depletion can take a timescale of several Gyr, which makes it hard to explain the existence of quiescent galaxies in the relatively young Universe (out to $z \sim 4$ or more, e.g. Straatman et al., 2014). Further analysis of the star formation histories (SFHs) of quiescent galaxies leads to growing evidence of the existence of fast quenching mechanisms, alongside other relatively slow quenching mechanisms such as depletion of gas supply (e.g. Moutard et al., 2016; Pacifici et al., 2016; Maltby et al., 2018; Rowlands et al., 2018b; Wu et al., 2018; Belli et al., 2019). Many mechanisms can be responsible for the quenching of a galaxy. They broadly fall into two categories, internal and external. Popular internal mechanisms to shut off star-formation are active galactic nucleus (AGN) feedback and morphological quenching. AGN can heat up the cold gas in the galaxies by thermal feedback and/or expel the cold gas by kinetic feedback, leading to a reduced gas content for star formation (Kaviraj et al., 2007a; Smethurst et al., 2017; French et al., 2018; Pawlik et al., 2018). The morphology of galaxies can likewise prevent star formation or accelerate gas depletion. Once a galaxy acquires a spheroid-dominated morphology, disc stabilisation may stop gas cloud fragmentation and therefore halt the star formation (Martig et al., 2009). A prominent bulge is argued to be an important condition for quenching star formation Bell et al. (2012). In contrast, the presence of bars is believed to funnel gas content into the galaxy centres (Athanassoula, 1992) and increase the gas depletion efficiency. For massive halos above $10^{12}M_{\odot}$, the inflowing gas can be heat up by the viral shock, thus the accreted gas does not collapse to form new stars (Birnboim & Dekel, 2003; Kereš et al., 2005).

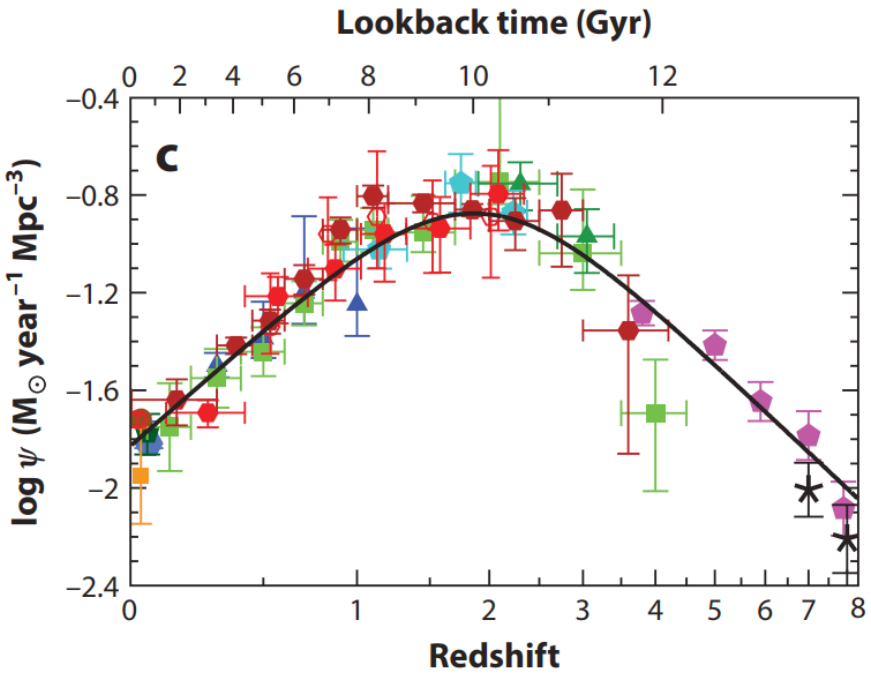

Figure 1.3: The history of cosmic star formation. The Universe's global star formation rate density has declined by a factor of ~ 10 since $z \sim 2$. Figure obtained from Madau & Dickinson (2014).

The hot gas in the halo fails to cool down because of radio mode AGN feedback (Croton et al., 2006) or "gravitational" heating of the intracluster medium (Khochfar & Ostriker, 2008). The hot gas halo is promoted to drive both mass quenching and environment quenching (Gabor & Davé, 2015).

Various external mechanisms can shut-off star formation and make galaxies quiescent, depending on the intermediate environment of the galaxies. Ram-pressure stripping can remove the cold gas content of satellite galaxies when they fall into a group or cluster (Gunn & Gott III, 1972); 'strangulation' prevents the galaxies from retaining a gaseous halo that is required to continually fuel the disc in the cluster environment (Larson et al., 1980; Balogh & Morris, 2000); fast encounters with other galaxies might disturb the star formation within the galaxies ('harassment', Gallagher III & Ostriker, 1972; Moore et al., 1998). In less dense environments, mergers are more likely to be responsible for quenching: the powerful starbursts triggered by a merger may quickly consume the gas content and the following stellar feedback (and possibly AGN feedback) could violently heat and expel the remaining gas (e.g. Barnes, 1992; Naab & Burkert, 2003; Bournaud et al., 2005).

1.2 Post-starburst galaxies

1.2.1 Definition and properties

Post-starburst (PSB) galaxies, also sometimes referred to as E+A or K+A galaxies, may occupy an important transitional state between the star-forming and quiescent populations, and could be an important candidate for the "fast" quenching route. These galaxies have experienced a rapid decline in their star formation following a previous period of very rapid star formation. Catching these galaxies as they transition to quiescence may provide important constraints on the causes of the rapid quenching which is not possible from archaeological studies of already-quiescent galaxies. They are identified by their excess population of intermediate-age (A- or F-type stars), but deficit or absence of hotter, younger stars (O- and B- types) leading to strong Balmer absorption lines, a strong Balmer break, and weak or absent nebular emission lines from star formation. An example spectrum of a PSB is shown in Figure 1.4. PSBs account for only about 1 per cent of local galaxies (Goto et al., 2008; Wong et al., 2012), however they may account for a significantly larger fraction of the galaxy population at higher redshifts (Tran et al., 2004a; Wild et al., 2009; Vergani et al., 2010; Whitaker et al., 2012; Wild et al., 2016; Rowlands et al., 2018b; Belli et al., 2019). Despite being rare, their number density is sufficient to account for a significant fraction of the growth of the red-sequence at $z < 2$, although the precise fraction is still debated (Tran et al., 2004a; Wild et al., 2009, 2010; Belli et al., 2019).

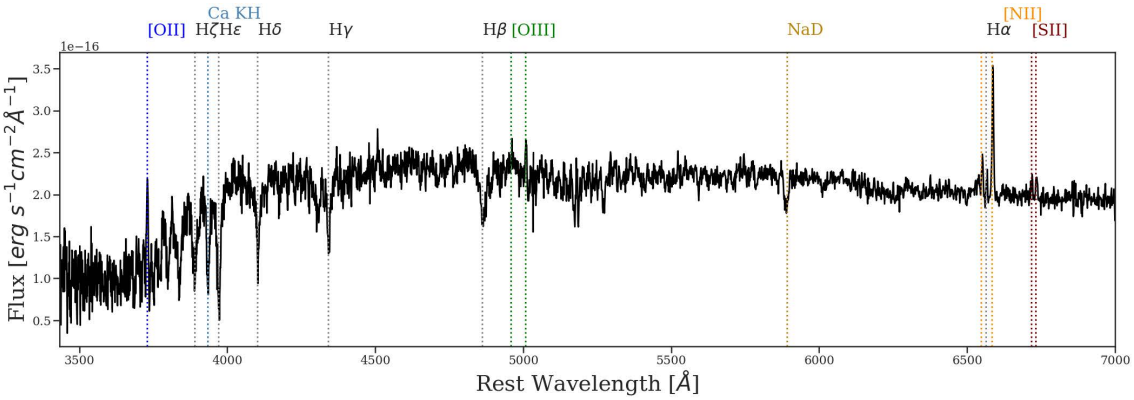

Figure 1.4: An Example spectrum of a PSB from the SDSS (spec-0524-52027-0492). This galaxy has strong Balmer absorption and weak emission lines. The short-lived O- and B- types leave the main sequence and go as supernovae after the starburst (in $\sim 10^7$ yr), resulting in weak or absent nebular emission lines from star formation. The intermediate-age populations (A- or F-type stars) dominate the galaxy spectrum after the death of the O- and B- types stars, leading to the strong Balmer break. The weak emission lines in this spectrum are more consistent with shock or AGN-dominated ionization than ionization from star formation. Figure obtained from French (2021).

Post-starburst galaxies are believed to be a transiting type between star-forming and quiescent populations for many reasons. PSBs at $0.5 < z < 1.0$ have intermediate values of the structural asymmetry and concentration parameters in between quiescent and star forming galaxies (Vergani et al., 2010). The Sérsic indices of PSBs also have an intermediate value of as revealed in Mendel et al. (2013). In visually inspections, PSBs are also reported to have intermediate morphologies in the Galaxy Zoo project (Wong et al., 2012). Structural analysis of post-starburst galaxies often reveals a connection with quiescent galaxies: they are more likely to have high central concentration and be more bulge-dominated than an average field galaxy with similar stellar mass(Tran et al., 2004b; Goto, 2005). Lack of disk-like structures is commonly found in PSBs Mendel et al. (2013). The findings motivate astronomers to take PSBs as a possible migrating path from the star-forming blue cloud to the quiescent red sequence. The contribution of PSBs to the growth of the red sequence is under debate, which I discuss more in the next section.

1.2.2 Identifying post-starburst galaxies

Traditional selection criteria

Traditionally, post-starburst candidates are selected based on strong Balmer absorption lines like H$\delta_{\rm A}$ absorption line or H$\gamma_{\rm A}$absorption line, with weak or absent nebular emission lines, usually Hα line (e.g. Goto et al., 2003; Quintero et al., 2004; Balogh et al., 2005) or the [OII] emission line (e.g. Dressler & Gunn, 1983; Zabludoff et al., 1996; Poggianti et al., 1999). However, Yan et al. (2006) warn that using [OII] line directly as a proxy for star formation rate may end up with seriously incompleteness sets of PSBs since the W[OII] in AGN-like galaxies can be as large as those in star-forming galaxies. On the other hand, Wild et al. (2020) find that using H$\delta_{\rm A}$ and W[OII] alone results in a high contamination rate in their samples, possibly due to dust attenuation of the OII line.

For galaxies at high redshift, for which spectra cannot be easily obtained, people suggest alternative PSB identification criteria based on broad-band multi-wavelength photometry. Whitaker et al. (2012) use the $U-V$ and $V-J$ rest-frame colours to select quiescent galaxies and the transitional younger quiescent galaxies, based on the fact that quiescent galaxies have a strong 4000 Å break, resulting red $U-V$ colours and blue $V-J$ colours compared with star-forming galaxies at the same $U-V$ colour.

Principal component analysis

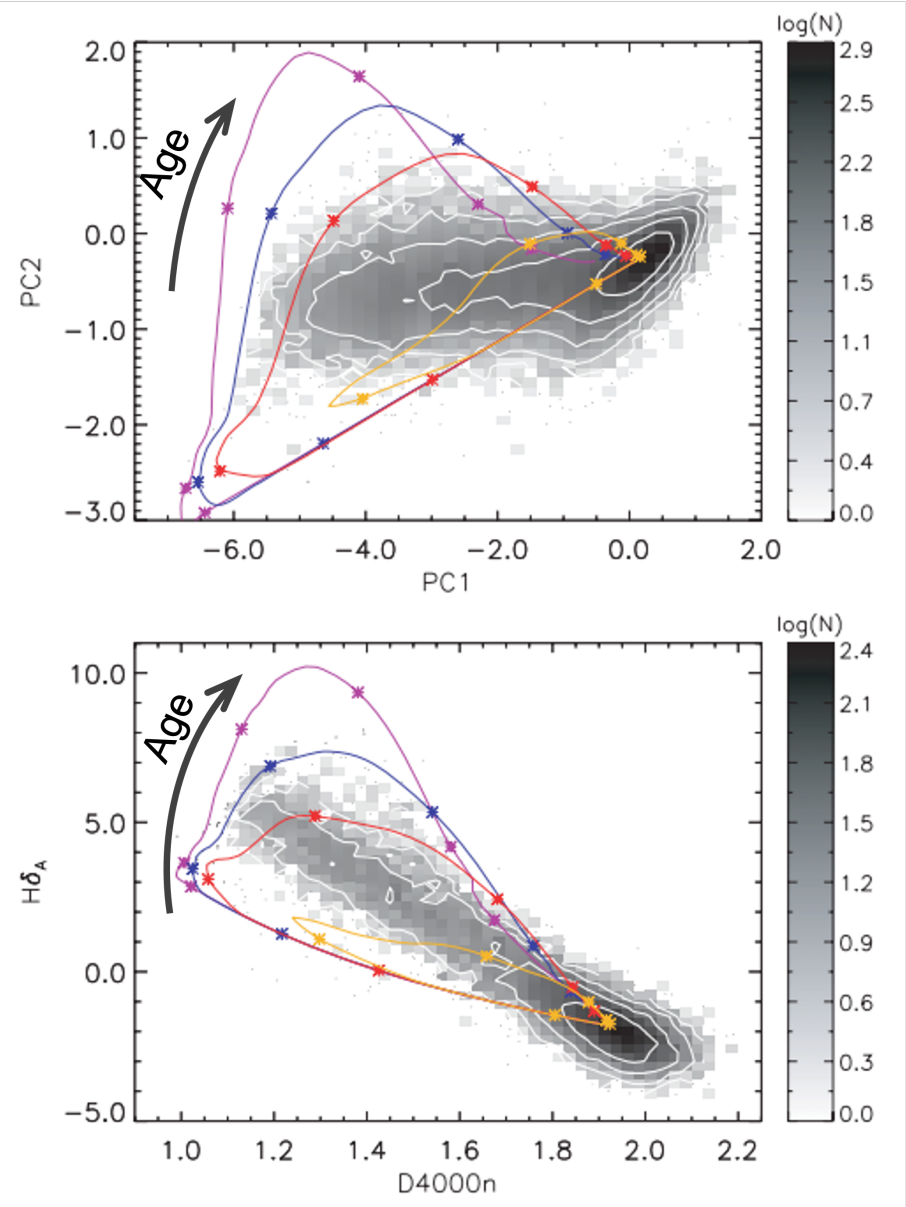

Figure 1.5: The tracks in PC1 vs PC2 (top panel) and D_n4000 vs Hδ_A (lower panel) of model (BC03) top-hat starbursts of 0.03 Gyr duration, superimposed on a composite early-type galaxy spectrum. The tracks are coloured by the burst mass fractions of the model: 0.5 per cent (orange), 1 per cent (red) and 3 per cent (blue) and 20 per cent (purple). Asterisks indicate times after the initial starburst of 0.001, 0.01, 0.1, 0.5, 1.0 and 1.5 Gyr. The grey-scale contours show the distribution for the spectra of high stellar surface mass density, low-z SDSS galaxies in the spectral indices spaces. PC1 is equivalent to Dn(4000), PC2 measures excess Balmer line strength. The PCA method can detect older and weaker PSBs compared to Hδ_A alone. Figure obtained from Wild et al. (2007).

The traditional method that employs emission lines will not select post-starburst galaxies with low-level residual star formation, or those that contain a narrow line AGN (Yan et al., 2006; Wild et al., 2007), and the samples can be contaminated by dust obscured star-forming

galaxies (Poggianti & Wu, 2000; Wild et al., 2020). Hence, Wild et al. (2007) promote a second spectroscopic diagnostic using the stellar continuum alone to identify galaxies with stronger Balmer absorption than expected, following previous studies using D_n4000 and $H\delta_A$ (Kauffmann et al., 2003)

Wild et al. (2007) applied a Principal Component Analysis (PCA) to the stellar continuum of model spectra between 3750 and 4150Å, finding the first component (PC1) to correlate strongly with the 4000Å break strength, while the second component (PC2) provided the excess Balmer absorption line strength over that expected for the 4000Å break strength. The method is analogous to using D_n4000 vs. $H\delta_A$, however has the added benefit of being able to combine information from all the Balmer absorption lines as well as the shape of the continuum in order to increase the SNR of the measurement, as well as rotating the parameter space so that the PSBs are easily identified lying above the star-forming main sequence. This means that older and weaker PSBs can be detected with the PCA compared to $H\delta_A$ alone (see Figure 1.5 and Wild et al., 2007, for a direct comparison). As the emission lines are not used, the method is sensitive to galaxies that contain narrow line AGN, and those galaxies that do not completely shut off their star formation.

Super-colour analysis

When galaxy spectra are unavailable, multi-wavelength photometry can be used to identify post-starburst galaxies. Wild et al. (2014) introduce a super-colour technique to classify galaxy spectral energy distribution (SED) shapes, in which principal component analysis is applied to the observed photometry. The PCA method compresses the complicated SEDs into a few linear combinations of observed bands, called super-colours. In Wild et al. (2016), super-colour analysis is slightly updated to classify galaxies in a slightly wider redshift range ($0.5 < z < 2$). Details of the super-colour technique can be found in the two papers cited above, here I provide a brief summary of the key features.

The super-colour analysis involves projecting the multi-wavelength photometry onto pre-computed eigenvectors (or equivalently eigenspectra) that were determined from a large library of 44,000 model SEDs created by combining the Bruzual & Charlot (2003) stellar population synthesis model with ‘stochastic star formation histories (Kauffmann et al., 2003; Gallazzi et al., 2005) and two component dust attenuation (Charlot & Fall, 2000). The precise details of this library are irrelevant, as it simply defines the weighting vectors for the projection of

any other dataset. This method therefore allows the direct comparison of simulated and real data so long as the same observed wavebands are used. Wild et al. convolve the model SEDs with a filter set that covers a wide wavelength range from blue-optical to near-infrared. However, each galaxy is observed at a single redshift in reality, with only several filters covering the wavelength range of interest. The observation data are sparsely sampled and are massively "gappy" compared to the eigenvectors which are computed using small steps in redshift in order to cover all possible combinations of observed photometry for galaxies over the full redshift range of $0.5 < z < 2$. This is accounted for using the "gappy PCA" method of Connolly & Szalay (1999), leading to formal errors on the final super-colours which depend slightly on redshift.

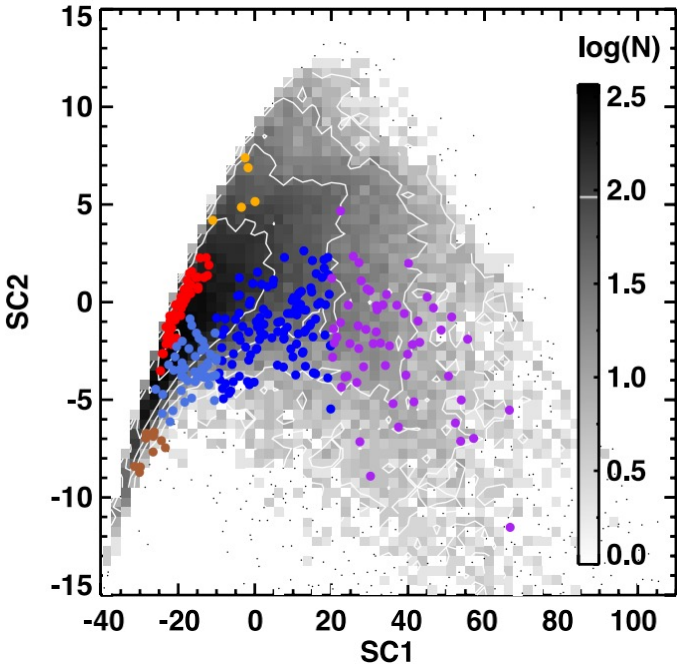

Figure 1.6: A subsample of UDS galaxies with UDSz spectra (coloured dots) in SC1–SC2 space. Each colour stands for a galaxy population: orange for PSBs, red for quiescent galaxies, and others for different type of star-forming galaxies. The distribution of stochastic burst model galaxy in SC1–SC2 space is plotted in grey-scale for comparison. Figure obtained from Wild et al. (2014).

The principal component amplitudes indicate the contribution of each eigenspectrum in the SED and are termed "super-colours" (SC) as they are equivalent to a traditional colour, i.e. they are weighted linear combinations of the observed fluxes. Wild et al. (2014) found that the first three eigenspectra are required to account for $> 99.9\%$ of the variance in the model SEDs, and can thus be used to accurately, succinctly and uniquely describe and reconstruct the shape of all galaxy SEDs. The 10-band observed photometry, for galaxies over a wide redshift

range, are compressed into just 3 numbers with little loss of information. Each super-colour indicates a particular property of the galaxy SEDs: SC1 describes the red-blue slope of the SED, indicating the average sSFR; SC2 changes the strength of the 4000 Å or Balmer break, indicating the fraction of stellar mass formed in the last $\sim$ 1 Gyr as well as the metallicity of star-forming galaxies; SC3 also controls the exact SED shape around the 4000 Å break and helps to break the degeneracy between metallicity and burst fraction.

With the library of 'stochastic burst' model SEDs, Wild et al. (2014) find that post-starburst galaxies tend to locate in specific region in the super-colour space (Figure 1.6). They confirmed that the super-colour technique can detect post-starburst galaxies with similar properties to those detected in high-redshift spectroscopic surveys such as the VVDS.

1.2.3 Potential mechanisms to form PSBs

At high redshift, the morphologies of PSB galaxies are strongly suggestive of an extremely intense and rapid quenching process, such as a major gas-rich merger, multiple mergers or protogalactic collapse. Almaini et al. (2017) find that massive PSBs at redshift ($z > 1$) are significantly smaller than comparable quiescent galaxies at the same stellar mass and epoch which is strongly suggestive of a recent dissipative collapse event associated with the shut off in star formation (see also Yano et al., 2016). This appears to depend on stellar mass and epoch, with lower mass and lower redshift PSBs more similar in structure to equivalent quiescent galaxies (Maltby et al., 2018; Pawlik et al., 2018).

At lower redshift, galaxy mergers have long been proposed as a possible formation mechanism for PSBs shortly after the discovery of E+A galaxies (Lavery & Henry, 1988). A substantial fraction of PSBs are found with faint tidal features or companion galaxies (Zabludoff et al., 1996; Chang et al., 2001; Pawlik et al., 2018). In addition, PSBs at low-redshift can have surprisingly high fractions of mass formed in the starburst of typically 20%, but occasionally as much as 70% (Kaviraj et al., 2007a; Pawlik et al., 2018), which again supports major mergers as the only mechanism known in the local Universe to be able to feed sufficient gas into the central regions of a galaxy in a short enough time (see also the discussion in Weaver et al., 2018). Such a scenario is consistent with the results from the cosmological hydrodynamic simulation EAGLE, where Davis et al. (2019) find that local ($z \sim 0$) simulated post-starburst galaxies are predominantly caused by major mergers. Pawlik et al. (2019) used the same EAGLE simulations, post-processed to produce mock optical spectra, to find that in addition to

classical major mergers, a range of different processes can create weak PSB features detectable in modern spectroscopic surveys. These include harassment by multiple smaller galaxies as well as rejuvenation from gas brought in by infalling small satellites.

During a galaxy merger, the discs of the galaxies are typically destroyed and the gas components are funnelled into the galaxy centre, leading to a powerful centralised starburst followed by rapid quenching of the star formation (e.g. Barnes, 1992; Naab & Burkert, 2003; Bournaud et al., 2005). However, this induced starburst may not cause sufficient quenching to produce remnants with no ongoing star formation, as without a mechanism to expel the gas directly, the remnant typically continues to form stars (e.g. Sanders et al., 1988; Hopkins et al., 2006; Johansson et al., 2009). The more or less complete prevention of star formation in quiescent galaxies is the primary motivation for black hole feedback in the current generation of galaxy evolution simulations. In this model, an active galactic nucleus (AGN) can heat up the cold gas in the galaxies by thermal feedback and/or expel the cold gas by mechanical feedback, resulting in a lack of material for further star formation. Several studies suggest that PSBs may harbour an excess fraction of AGN compared to normal galaxies (e.g. Yan et al., 2006; Wild et al., 2007, 2010; Pawlik et al., 2018), however the short duty cycles of AGN, compared to the observed post-starburst features, hamper any direct comparison.

It is also possible that external conditions play a role in the ultimate quenching of post-merger remnants, which may explain why PSB galaxies are more common in (some) clusters and intermediate density environments (e.g. Zabludoff et al., 1996; Poggianti et al., 2009; Socolovsky et al., 2018; Pawlik et al., 2018; Paccagnella et al., 2019). Ram-pressure stripping, strangulation or harassment may all play a role in suppressing further star formation in merger remnants that find themselves in dense environments.

Starburst in galaxy mergers

Galaxy mergers play an important role in creating the post-starburst galaxies as discussed above; they are one of the major topics of this thesis. Hence it is critical to know what processes happen during the galaxy merger and how these processes lead to the enhancement of star formation activity. Here I give a brief summary below. A more detailed review can be found in Bournaud (2011).

When a galaxy flies through/closely interact with another galaxy, the gravity triggers a

mass accumulation from the latter galaxy along the wake of the first one, the accumulated mass slows down the first galaxy in return. This mechanism is named dynamical friction. The dynamical friction reduces the relative velocity of the interacting galaxies and drives them to merge into a single, more massive one.

During the merger, the stars in merging galaxies experience a rapid and significant variation in the mass distribution and the gravitational potential. Such a violent relaxation dramatically changes the orbits of the stars. Some stars lose their energy and sink into the galaxy centre, resulting in a compact core. Other stars can gain more energy and move onto higher orbits or even become unbound and escape the galaxies. The escaped stars carry away a substantial fraction of the initial energy, leaving a low-energy system, also helping shape a compact remnant. The violent relaxation during the merger effectively destroys the disc components of the progenitor galaxies and produces elliptical-like remnants, or forms new bulges/builds up pre-existing bulges if it is a minor merger (Hopkins et al., 2010).

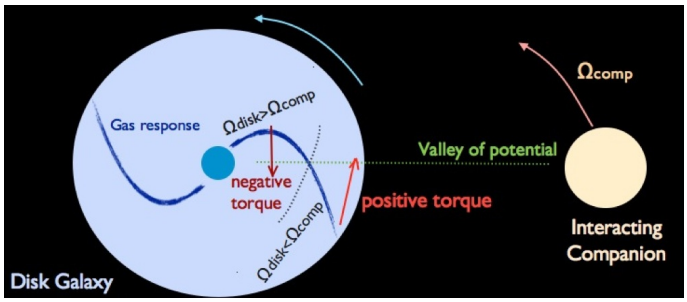

Figure 1.7: Simplified description of the gas response in a galaxy interaction. The gas within the co-rotation radius suffers a negative gravity torque due to the valley of potential, these gas loses their angular momentum and inflows to the galaxy centre, fuelling the centralized starburst during the merger. On the contrary, the gas outside the co-rotation radius undergoes a positive gravity torque and gain more angular momentum, which drives the outer disk material to form the so-called "tidal" tails. Figure obtained from Bournaud (2011).

The tidal field disrupts the gas within the disks and expels the gas to form the so-called "tidal" tails. However, the tidal field is not the only mechanism that affects the distribution of the gas; the gravity torque also plays a critical role. A simplified description of the gas response to gravity torque during the mergers is provided in Figure 1.7. The tidal field from a companion breaks the symmetry of the gravitational potential, creating a valley of potential. The gas within the co-rotation radius suffers a negative gravity torque due to the valley of potential, these gas loses their angular momentum and inflows to the galaxy centre, fuelling the centralized starburst during the merger. On the contrary, the gas outside the co-rotation radius undergoes a positive gravity torque and gain more angular momentum, which drives

the outer disk material to form the so-called "tidal" tails.

Besides the gas inflow and outflow, the interaction between galaxies also increases the turbulence of gas, leading to a dense gas excess and finally a starburst. Such a starburst is spatially extended. Starbursts outside the central kpc are observed in many merging systems, for instance, in the Mice galaxies (Barnes, 2004)and in the Antennae galaxies (Wang et al., 2004).

Mergers can induce centralized starburst via inflowing gas and spatially extended starburst via turbulent gas. Reproducing the latter one could be expensive in SPH simulation since resolving ISM turbulence requests a very high resolution. Hence, I will focus on the nuclear starburst galaxies and their descendant PSBs in this thesis.

1.2.4 PSBs in simulations

The development of spectral synthesis models allowed the first theoretical explorations of the unusual spectral properties of PSB galaxies (e.g. Couch & Sharples, 1987; Poggianti et al., 1999; Shioya et al., 2004) leading to a basic understanding of their star formation histories. However, significant progress on understanding the formation mechanisms was only made once the dynamics of the gas in galaxies could be tracked in detail.

Early hydrodynamic gas-rich merger simulations combined with simple star formation laws showed that gas rich mergers could lead to star formation histories characterized by strong, short bursts (Mihos & Hernquist, 1994a, 1996). Combining hydrodynamical galaxy merger simulations with spectral synthesis models, led Bekki et al. (2005) to reproduce the positive colour gradient and negative radial Hδ gradient observed in local PSBs by Pracy et al. (2005). A similar analysis was carried out by Wild et al. (2009), at higher resolution and using more sophisticated star formation and feedback models, including a comparison between models with and without BH feedback. They also found that the stellar continuum properties of PSB galaxies at $0.5 < z < 1$ could be reproduced by merger simulations with starburst mass fractions larger than $\sim 5-10\%$ and decay times shorter than $\sim 10^8$ yr. BH feedback was not required to reproduce the stellar continuum features of PSB galaxies, although they did not investigate the emission line properties. Similar simulations were carried out by Snyder et al. (2011), who again concluded that the role of AGN feedback in ceasing star formation and producing PSB features was negligible. Since these studies were undertaken the sub-resolution recipes

used in the hydrodynamic simulations have become much more sophisticated and the spatial resolution has increased, motivating a revisit of the question of how the unusual spectral properties of post-starburst galaxies can be reproduced.

1.3 The rapid quenching route

Some proposed quenching mechanisms operate on a short time scale and can cause the rapid quenching of galaxies. For example, AGN feedback has a timescale shorter than 0.2 Gyr (Kaviraj et al., 2011), ram-pressure stripping operates on galaxy cluster crossing time-scales, which is a few ten's of Myr (Abadi et al., 1999). These mechanism could result in a rapid truncation of star formation, or quenching, forming galaxies named as rapidly quenched galaxies (RQGs). As the result of rapid quenching, the light of RQGs is dominated by A- and F-type stars since O- and B-type stars die with supernova a few million years after the quenching event. RQGs have little/no emission lines but strong Balmer absorption lines and break. RQGs have the same spectrum properties as the PSBs, probably the only difference is that PSBs have stronger Balmer absorption features because of the huge population of A- and F-type formed during the starbursts before their rapid quenching. Actually rapidly quenched galaxies are selected by the same method used to select PSBs, therefore, RQGs are equivalent to PSBs in the observational work, this is only a matter of differing terminology.

The contribution of the rapid quenched route to the growth of the red sequence has been a topic of research for the last decade. Wild et al. (2009) used spectra from the VVDS survey to estimate that ∼40% of the mass growth of the quiescent population at $z \sim 0.7$ is contributed by PSBs, and Wild et al. (2020) combine photometry and spectra from the UDS survey to estimate a value of 25-50% at $z \sim 1$. Belli et al. (2019) estimate that fast quenching accounts for $\sim$ 20% of the growth of the red sequence at $z \sim 1.4$ and $\sim$ 50% by $z \sim 2.2$. The importance of the rapid quenching route appears to decrease with decreasing redshift and may rapidly diminish at $z < 1$ (Wild et al., 2016; Rowlands et al., 2018b), and appears to also depend on stellar mass and environment. Socolovsky et al. (2018) find a much higher percentage of $\sim$ 70% of quiescent cluster galaxies with $9.0 < log(\mathrm{M/M_\odot}) < 10.5$ and $0.5 < z < 1.0$ have rapidly quenched. There is a strong link with galaxy morphology, with rapidly quenched galaxies being highly compact (Yano et al., 2016; Almaini et al., 2017; Maltby et al., 2018), and compact galaxies at intermediate redshifts found to have faster quenching times than normal-sized galaxies (Wu et al., 2018; Nogueira-Cavalcante et al., 2019).

The works on the observation side motivate me to investigate the topic with simulations. In this thesis, I run a set of binary merger simulations to reproduce post-starburst galaxies. The merger simulations are also used to investigate radial gradients in the spectral indices of PSBs. In order to study the statistical properties of PSBs/RQGs, a large sample is required. Hence, I research the SIMBA cosmological hydrodynamic simulation. SIMBA is found to reproduce a bimodality in quenching timescales (Rodríguez Montero et al., 2019), which provides a great platform to further investigate the contribution of different pathways to quenching and the growth of the red sequence.

1.4 Thesis outline

In this thesis, I present my work on the analysis of post-starburst galaxies and the fast quenching route using simulations and mock observations. I then compare the results to observations, trying to interpret the formation of PSBs and their importance to the big picture of galaxy evolution.

This thesis is structured as follows:

- In Chapter 2, I introduce the simulations used throughout my PhD projects.
- In Chapter 3, I give the details of SEDmorph, the code I developed to convert simulation results into mock observations.
- Chapter 4 utilises the binary merger simulation set and investigates the origin of the radial gradients in PSBs and constraining their formation mechanism.
- Chapter 5 looks at the SIMBA cosmological simulation and studies the population of rapidly quenched galaxies.
- In Chapter 6, I summarise the work of my thesis and discuss future plans and directions.

2

SIMULATIONS

In this chapter, I will introduce the simulations used throughout my PhD project. The simulations include a set of binary merger simulations run by myself and a cosmological simulation run by my collaborators. The binary mergers simulations are run with a variety of black hole feedback models, progenitor galaxies, orbits and mass ratios; they are used to investigate the properties and the formation of post-starburst galaxies. In this chapter, I will give the details of the sub-resolution physics of the simulations, setting up of the model galaxies and the mergers. The cosmological simulation SIMBA is investigated in order to figure out the contribution of the post-starburst galaxies/rapidly quenched galaxies to the growth of the red sequence. SIMBA is described in the second section of this chapter.

2.1 Binary merger simulations

Our binary merger simulations are run with the N-body smoothed particle hydrodynamics (SPH) code, SPHGal (Hu et al., 2014; Eisenreich et al., 2017), which is an updated version of the Gadget-3 code (Springel, 2005). Like Gadget-3, SPHGal computes gravitational forces

with a hierarchical tree algorithm.[1] Additionally, gravitational softening is applied to reduce artificially strong two-body encounters between the massive particles. Compared with the original Gadget-3 code, SPHGal replaces the spline kernel with a Wendland C^4 kernel and increases the number of neighbours in the SPH kernel to 100. The code employs a set of new features including the pressure-entropy formulation of SPH, an updated estimate of velocity gradients, a modified artificial viscosity switch with a modified strong limiter, artificial conduction of thermal energy and a time step limiter (see Lahén et al., 2018, for more details). Together these changes reduce numerical artefacts in the fluid mixing and improve the convergence rate of the SPH calculation.

2.1.1 Stellar sub-resolution physics

The subresolution astrophysics models in SPHGal are based on those by Scannapieco et al. (2005, 2006), updated by Aumer et al. (2013), and include gas cooling, star formation, chemical evolution and stellar feedback. In this model, the gas component cools with a rate dependent on its temperature, density and metal abundance. Assuming that the gas is optically thin and in ionisation equilibrium, the cooling rates are calculated following Wiersma et al. (2009), on an element-by-element basis. The effects of a uniform redshift-dependent ionising UV/X-ray background (Haardt & Madau, 2001) are also included assuming $z = 0$. The cooling rates are calculated over a temperature range of $10^2 \leq T \leq 10^9\ K$.

Dense and cold gas particles are able to form stars, once the gas density ρ_g is greater than $\rho_{crit} = 1.6\times10^{-23}$ g/cm^3, i.e $n_H = 10$ cm^{-3}, and the gas temperature is less than $T = 12000$ K. For a star-forming gas particle with a mass of m_g, its star formation rate is estimated as

$$SFR = \epsilon_{SFR}\frac{m_g}{t_{ff}}, \tag{2.1}$$

where $\epsilon_{SFR} = m_*/m_g$ is the star formation efficiency, and t_{ff} is the free-fall time derived from the harmonic oscillator frequency in a spherically symmetric cloud:

$$t_{ff} = \sqrt{\frac{3\pi}{32G\rho_g}}. \tag{2.2}$$

The free-fall time t_{ff} is often replaced with a similar estimate of the dynamical time-scale

[1] SPHGal offers an option to combine the standard tree algorithm with a particle-mesh (PM) scheme for long-range gravitational forces, but I turned PM off as it is unnecessary in my merger simulations.

$t_{dyn} \sim (4\pi G\rho_g)^{-1/2}$. Hence, the volume density of SFR can be given by

$$\frac{d\rho_*}{dt} = -\frac{d\rho_g}{dt} = \epsilon_{SFR}\frac{\rho_g}{t_{dyn}}. \tag{2.3}$$

Equation 2.3 implies a star formation rate proportional to $\rho_g^{3/2}$, matching the Kennicutt-Schmidt law for star-forming galaxies (Schmidt, 1959; Kennicutt Jr, 1998). Equation 2.3 can be rewritten into

$$\frac{d\ln\rho_g}{dt} = -\frac{\epsilon_{SFR}}{t_{dyn}}. \tag{2.4}$$

Integrating Equation 2.4 over Δt, the length of the current time step, the probability P that a gas particle converts into a stellar particle in the current time step is:

$$P = 1 - \exp\left(\epsilon_{SFR}\frac{\Delta t}{t_{dyn}}\right) = 1 - \exp\left(\epsilon_{SFR}\Delta t\sqrt{4\pi G\rho_g}\right). \tag{2.5}$$

Here I adopt a fixed efficiency of $\epsilon_{SFR} = 0.02$ in the merger simulations. At each time step, SPHGal computes P from Equation 2.5 for gas particles that are eligible to form stars. The code then draws random numbers to decide which gas particles actually form stars during the time step.

To track the chemical evolution in the simulations, every baryonic particle contains 11 elements (H, He, C, Mg, O, Fe, Si, N, Ne, S, Ca) that evolve based on models of chemical release rates from Iwamoto et al. (1999) for supernovae type Ia (SNIa), Woosley & Weaver (1995) for supernovae type II (SNII) and Karakas (2010) for asymptotic giant branch (AGB) stars. The star particles distribute the metals to the surrounding gas particles by the stellar feedback of SNIa, SNII and AGB stars. The metallicity diffusion implementation by Aumer et al. (2013) is included here to smooth the variations in the metallicity between neighbouring gas particles.

The stellar particles provide feedback the surrounding gas via SNII 3 Myr after their formation, followed by the SNIa for which feedback is released repeatedly every 50 Myr from a stellar age of 50 Myr until 10 Gyr, with the assumption that the ejecta mass decays proportionally to t^{-1} Maoz et al. (2011) and the total release is 2 SNIa per $1000 M\odot$ of stellar mass. The total feedback energy by SN to the interstellar matter (ISM) is given by

$$E_{SN} = \frac{1}{2}m_{eject}v_{SN}^2 \tag{2.6}$$

where m_{eject} is the mass of SN ejecta, v_{SN} is the velocity of SN ejecta (we adopt $v_{SN} =$ 4000 km/s here) and the SN ejecta in our model is metallicity dependent.

The thermal and kinetic feedback of SN are achieved by a distance dependent multiphase method. The phases here are the free expansion (FE) phase, the adiabatic SedovTaylor (ST) phase (Taylor, 1950; Sedov, 1959) and the snowplow (SP) phase (McKee & Ostriker, 1977; Blondin et al., 1998). The gas particles that are closest to the SN receive the feedback in the FE phase with momentum conservation and the feedback energy is in kinetic form only. At greater distances, the shocked ISM mass exceeds the SN ejecta mass, gas particles in this outer region then receive feedback in the ST phase with heating. In the ST phase, the feedback energy are in both thermal (70%) and kinetic (30%) forms. At even larger distances, the velocity of the SN ejecta decreases further, finally dispersing the shock. Gas particles in this outermost region receive feedback in the SP phase with efficient radiative cooling. Again both thermal (70%) and kinetic (30%) energy is assumed, however the total amount of energy decreases with distance from the SN.

Both the energy and enrichment feedback from AGB stars are dealt with in the same fashion as that from the type Ia SNe. However, as the wind velocity of AGB ejecta is just 25 km/s, much smaller than v_{SN}, only the FE phase is included for AGB feedback.

2.1.2 Thermal black hole feedback model

We run a set of merger simulations without black hole (BH) feedback and find that extra centrally injected energy is required in order to suppress the star formation in the merger remnants sufficiently to obtain the small Hα equivalent widths observed in many post-starburst galaxies. I investigate two different black hole models: a "classical" model with thermal energy injection only (Springel et al., 2005; Johansson et al., 2009), and an "updated" model with both thermal and mechanical energy injection (Choi et al., 2012).

In the classic model the unresolved gas accretion onto the BH is parameterised by the BondiHoyleLyttleton model (Hoyle & Lyttleton, 1939; Bondi & Hoyle, 1944; Bondi, 1952), in which the BH accretion rate is given by:

$$\dot{M}_B = \frac{4\pi\alpha M_{BH}^2 \rho}{(c_s^2 + v^2)^{3/2}} \tag{2.7}$$

where ρ is the gas density, c_s is the sound speed of the surrounding gas, v is the velocity of

the BH relative to the surrounding gas, and α is a dimensionless efficiency parameter set to enable the self-regulation of the BH mass growth and ensure that the BH accretion reaches the Eddington regime in a gas-rich environment (Johansson et al., 2009). Physically, we should have $\alpha = 1$, however Springel et al. (2005) and Johansson et al. (2009) use a value of $\alpha = 100$ to account for the underestimated gas density or the overestimated gas temperature near the Bondi radius. As the spatial resolution of the simulations is increased, the local gas density and temperature is more accurately modelled, and α must be decreased. Here I set $\alpha = 25$ and confirmed that this value allows the BHs in the merger remnants to grow onto, and stay on, the $M_{BH} - \sigma$ relation (van den Bosch, 2016).

The accretion rate is limited to the Eddington accretion rate:

$$\dot{M}_{edd} = \frac{4\pi G M_{BH} m_p}{\epsilon_r \sigma_T c} \tag{2.8}$$

where m_p is the proton mass, σ_T is the Thomson cross-section and ϵ_r is the radiative efficiency. Here I adopt $\epsilon_r = 0.1$, the mean value of radiatively efficient accretion onto a Schwarzschild BH (Shakura & Sunyaev, 1973). Thus, the final (inflowing) accretion rate is given by:

$$\dot{M}_{in} = min(\dot{M}_B,\ \dot{M}_{edd}). \tag{2.9}$$

The radiated luminosity of the BH is given by:

$$L_r = \epsilon_r \dot{M}_{in} c^2. \tag{2.10}$$

We assume that a fraction, ϵ_f, of radiated energy couples with the surrounding gas leading to the feedback energy:

$$E_{\text{feed}} = \epsilon_f L_r = \epsilon_f \epsilon_r \dot{M}_{in} c^2. \tag{2.11}$$

We adopt a fixed value of $\epsilon_f = 0.05$, a value that is widely chosen in the literature (Springel et al., 2005; Di Matteo et al., 2005; Johansson et al., 2009; Johansson et al., 2009; Choi et al., 2012). The choice of this value for ϵ_f is motivated by the fact that in combination with the thermal feedback model the simulations are able to reproduce the observed $M_{BH} - \sigma$ relation.

In this classical thermal black hole feedback model, all the feedback energy is distributed as thermal energy into the ~ 100 gas particles closest to the BH, weighted by the SPH kernel. The

gas around the BH is therefore heated by the BH feedback and expands, reducing its density, which leads to a cessation in star formation.

In my merger simulations, I assume that the binary BHs merge as soon as their separation drops below the smoothing length and their relative velocity drops below the local sound speed of the surrounding gas. Due to the limited spatial resolution the BHs can wander away from the centre of the galaxies, especially in unequal-mass mergers. To ensure the successful merging of the BHs during the final coalescence of their host galaxies, at every time step I re-locate the BH to the minimum potential in the central region of the galaxy (see Johansson et al., 2009, for more discussion on this procedure).

2.1.3 Mechanical black hole feedback model

It has been suggested that a strong wind from an accreting BH might convey energy, mass and momentum from the centre to the surrounding gas (De Kool et al., 2001; Moe et al., 2009; Dunn et al., 2010), causing the gas outflows and the regulation of star formation in the host galaxies (Tremonti et al., 2007; Feruglio et al., 2010). To simulate this effect I create a third set of simulations in which I adopt the mechanical BH feedback model developed by Choi et al. (2012; 2014).

In this model the total accretion rate onto the BH is given by:

$$\dot{M}_{acc} = \dot{M}_{in} - \dot{M}_{out} \tag{2.12}$$

where $\dot{M}_{out}$ is the outflowing mass loss rate, and $\dot{M}_{in}$ is calculated as above (Eqn. 2.9) with $\dot{M}_B$ computed with an 'alternative averaging (AA)' method (see Choi et al., 2012). We further define the kinetic energy rate of the outflowing wind:

$$\dot{E}_w = \epsilon_f \epsilon_r \dot{M}_{acc} c^2 = \frac{1}{2} \dot{M}_{out} v_w^2 \tag{2.13}$$

where ϵ_r and ϵ_f are, respectively, the radiative efficiency and fraction of the radiated energy that couples to the surrounding gas (as above), and v_w is the velocity of the wind assuming energy conservation and a single wind velocity.

Following Choi et al. (2012) I define the ratio of the mass outflow rate to the mass accretion

rate as:

$$\psi \equiv \dot{M}_{out}/\dot{M}_{acc} = 2\epsilon_f \epsilon_r c^2/v_w^2. \tag{2.14}$$

Since the momentum is conserved, the total accretion rate $\dot{M}_{acc}$ and the kinetic energy rate $\dot{E}_w$ can be solved out as:

$$\dot{M}_{acc} = \dot{M}_{in}\frac{1}{1+\psi} \tag{2.15a}$$

$$\dot{E}_w = \epsilon_f \epsilon_r c^2 \dot{M}_{in}\frac{1}{1+\psi} \tag{2.15b}$$

Inspired by observations of broad absorption line winds (Crenshaw et al., 2003; Moe et al., 2009), we assume a wind velocity of $v_w = 10,000\,\mathrm{km/s}$. With the widely adopted feedback efficiencies of $\epsilon_f \epsilon_r = 0.1 \times 0.05 = 0.005$, Eqn. 2.14 gives $\psi = 0.9$, i.e., 90% of the inflowing mass is ejected in an AGN wind, with both energy and mass carried from the BH to the outskirts of the galaxy. This outflowing gas collides with the ambient ISM on its way out, resulting in a momentum-driven flow. I simulate this phenomenon by allowing the emitted wind particle to share its momentum with its 2 nearest neighbouring gas particles. As the gas particles all have the same mass in my simulation, all three gas particles gain the same velocity increment of $\Delta v \sim (v_w/3)$ km/s. This treatment conserves the momentum but decreases the total kinetic energy. To conserve the total energy, the residual energy is deposited into these three particles in form of thermal energy.

Choi et al. (2012) include an additional thermal feedback component in their simulations to simulate the effect of X-ray radiation from the AGN on the surrounding gas. However, I found that this was too effective at suppressing star formation, eliminating the starburst during the merger phase and preventing the appearance of the strong Balmer absorption lines seen in PSB galaxies. I therefore only ran one simulation with this effect included. I note that the updated stellar feedback model used in this project, compared to the stellar feedback model used in Choi et al. (2012), may in part be responsible for the dramatic suppression of star formation seen in my simulations when including this additional thermal X-ray BH feedback component.

2.1.4 Galaxy models

The progenitor galaxies are set up following the method given in Johansson et al. (2009) assuming a ΛCDM cosmology with $\Omega_m = 0.30$, $\Omega_\Lambda = 0.70$, and $H_0 = 71\,\mathrm{km/s/Mpc}$, with

Table 2.1: Parameters for the progenitor disc galaxies. Total masses, M, are given in units of $10^{10} M_{\odot}$, scale radii and heights are in kpc, N is particle number, m gives the individual particle masses, ϵ the gravitational softening lengths and SFR is in $M_{\odot}$/yr. Other parameters are defined in the text.

Property	Sa	Sc	Sd	Scp3
M_{vir}	134.1	134.1	134.1	44.7
$M_{disc,*}$	2.5	3.2	3.5	1.17
M_{gas}	0.5	0.9	1.6	0.3
M_{bulge}	2.5	1.4	0.4	0.47
M_{DM}	128.6	128.6	128.6	42.9
B/T	0.5	0.3	0.1	0.3333
f_{gas}	0.17	0.22	0.31	0.22
r_{disc}	3.75	3.79	3.85	2.63
z_{disc}	0.75	0.76	0.77	0.53
r_{bulge}	0.75	0.76	0.77	0.53
c		9		
λ		0.33		
N_{total}	800000	800000	800000	266666
N_{DM}	400000	400000	400000	133333
$N_{disc,*}$	181818	233333	257143	77778
N_{gas}	36364	66667	114286	22222
N_{bulge}	181818	100000	28571	33333
m_{DM}		$3.2 \times 10^6 M_{\odot}$		
m_{baryon}		$1.4 \times 10^5 M_{\odot}$		
ϵ_{DM}		137 pc		
ϵ_b		28 pc		
SFR	$\sim$1	$\sim$2	$\sim$5	$\sim$0.5

the aim to mimic disc galaxies observed in the local Universe. A summary of the progenitor galaxy parameters used in this project can be found in Table 2.1. The primary galaxies have a virial velocity of $v_{vir} = 160\,\mathrm{km/s}$, resulting in a total virial mass of $M_{vir} = v_{vir}^3/10GH_0 = 1.34 \times 10^{12}\ M_\odot$. The majority of this mass ($M_{DM} = 1.286 \times 10^{12} M_\odot$) is in the dark matter (DM) halo, which has a Hernquist density profile with a concentration parameter of $c = 9$ (Hernquist, 1990). The baryonic mass fraction is 0.041, distributed between a gaseous disc (M_{gas}), a stellar disc ($M_{disc,*}$) and a stellar bulge (M_{bulge}), with $f_{gas} = M_{gas}/(M_{gas} + M_{disc,*})$ determining the gas fraction in the disc. Each progenitor galaxy has a total particle number of 8×10^5. Half are DM particles and half baryonic, yielding a mass resolution of $1.4 \times 10^5 \mathrm{M}_\odot$ and $3.2 \times 10^6 \mathrm{M}_\odot$ for baryonic and DM particles respectively. The gravitational softening lengths are $\epsilon_{\mathrm{bar}} = 28\,\mathrm{pc}$ and $\epsilon_{\mathrm{DM}} = 137\,\mathrm{pc}$ for the baryonic and dark matter components respectively.

The disc has an exponential mass profile with scale length r_{disc}, determined by assuming that the disc material conserves specific angular momentum during the disc formation with a constant halo spin of $\lambda = 0.033$ (Mo et al., 1998). The scale height of the stellar disc is set to $z_{disc} = 0.2\, r_{disc}$. The gaseous disc has the same scale length as that of the stellar disc and the vertical structure of the gaseous disc is determined such that it is in hydrostatic equilibrium (Springel et al., 2005). The stellar bulges follow a Hernquist (1990) profile with a scale length of $r_{bulge} = 0.2 r_{disc}$. The mass of the bulges are determined by the parameter B/T, the stellar bulge-to-total stellar mass ratio. By choosing different bulge-to-total stellar mass ratios and corresponding gas fractions, I create 3 progenitor galaxies of different morphology types, aiming to roughly mimic the average properties of Sa, Sc, and Sd galaxies. The specific values are chosen loosely based on values for local SDSS galaxies, by combining the range of i-band luminosity B/T values from Gadotti (2009), with the range of atomic and molecular gas mass fractions from Saintonge et al. (2016).

For the simulations with BH feedback the progenitor galaxies host BHs at their potential minima. The mass of the BH is given by the $M_{BH} - \sigma$ relation, with σ calculated from the distribution of the bulge star velocities (van den Bosch, 2016).

In order to build accurate spectral models, as well as include the feedback from old stars, we must initialise the stellar particles with their ages and metallicities. For the stellar particles in the bulge, I adopt an exponentially decaying star formation rate (SFR) over the time:

$$SFR_b(t) = Ce^{-(t-t_0)/\tau}, \tag{2.16}$$

where $t_0 = 10.2\,\mathrm{Gyr}$ is the start of the simulation, C is a normalisation factor, and $\tau = 1\,\mathrm{Gyr}$ is the timescale of the exponential decline. I assume that the star formation in the bulge started at a cosmic time of $t = 0.5\,\mathrm{Gyr}$, leading to a negligible SFR compared to the disc by t_0.

For the stellar particles in the disc, I follow Lahén et al. (2018) and adopt a linearly decaying SFR with an initial SFR at $t_0 = 10.2\,\mathrm{Gyr}$ similar to that found in local star-forming disc galaxies. I then run the galaxies in isolation and iteratively adjust the initial SFR estimate until the SFR transitions continuously from the initial value to the actual SFR at the start of the simulation (see Table 2.1). By requiring that the integration of the star formation rate history ove time is equal to the total stellar mass at the start of the simulation, the age distribution of the stellar particles can be obtained.

To be fully consistent with the employed sub-resolution models, we must also initialise the metallicity distribution. Here I adopt a uniform, log-linear radially decaying metallicity profile with the Milky Way as a reference (Zaritsky et al., 1994). Using the observed Oxygen gradient of 0.0585 dex/kpc, I set up the galaxies with roughly solar total metallicities. When assigning metal elements to individual stellar particles, I assume a scatter of 0.2 dex motivated by the the maximum measurement error in Kilian-Montenbruck et al. (1994) and fix an upper limit on the metal mass fraction of 5% to prevent the stellar particles from becoming unphysically metal heavy.

Due to element recycling, stars with later cosmic formation times tend to have higher metallicities. To reproduce this phenomenon, I firstly randomly sample the age of individual stellar particles from the age distributions with an age scatter of $\Delta t = 100\,\mathrm{Myr}$. I then sort the stellar particles by their assigned metal mass fraction, and re-assign their ages keeping the same overall age distribution.

We additionally create a lower mass galaxy (Scp3), a smaller version of the Sc galaxy with a mass of one third that of the Sc galaxy. This is done by reducing v_{vir} to $160/\sqrt[3]{3}\,\mathrm{km/s} \sim 111\,\mathrm{km/s}$. The particle numbers of each component are reduced by one third to keep the mass resolution per particle constant.

2.1.5 Merger Simulations

After initialising the progenitor galaxies, I run the galaxy models in isolation for 0.5 Gyr to even out any numerical artefacts from the initial idealised setup. I then set up the merger

simulation with these relaxed galaxies at $t_{m0} = 10.7\,\mathrm{Gyr}$, on parabolic trajectories with three different initial orbital configurations as introduced by Naab & Burkert (2003):

1. G00: $i_1 = 0°$, $i_2 = 0°$, $\omega_1 = 0°$, $\omega_2 = 0°$;
2. G07: $i_1 = -109°$, $i_2 = 71°$, $\omega_1 = -60°$, $\omega_2 = -30°$;
3. G13: $i_1 = -109°$, $i_2 = 180°$, $\omega_1 = 60°$, $\omega_2 = 0°$.

where i_1 and i_2 denote the inclinations of the two discs relative to the orbital plane, and ω_1 and ω_2 denote the arguments of the orbits' pericenter. G00 is a symmetric prograde-prograde orbit. Both galaxies are orientated in the orbit plane and their angular momenta are parallel to the orbital angular momentum. G07 is a retrograde-prograde orbit with both galaxies inclined with respect to the orbital plane. G13 is retrograde-retrograde orbit, with one galaxy inclined while the other is not. The angular momentum of the second galaxy is anti-parallel to the orbital angular momentum.

The initial separation r_{sep} of the two progenitor galaxies is given by their average virial radii while the pericentre distance r_p is given by the sum of their disc scale lengths. Thus, for the equal-mass mergers (1:1) the initial separation is $r_{\mathrm{sep}} = (160 + 160)/2\,\mathrm{kpc/h} \sim 225\,\mathrm{kpc}$, the pericentre distance is $r_p = 2 \times 2.7\,\mathrm{kpc/h} \sim 7.6\,\mathrm{kpc}$. For the unequal-mass merger (3:1), the initial separation is $r_{\mathrm{sep}} = (160 + 111)/2\,\mathrm{kpc/h} \sim 135.5\,\mathrm{kpc}$, and the pericentre distance is $r_p = (2.7 + 1.90)\,\mathrm{kpc/h} \sim 6.5\,\mathrm{kpc}$. The progenitor galaxies approach each other following nearly parabolic orbits and interact under their own gravity.

We run a set of simulations with different progenitor galaxies and orbits. For the equal-mass mergers I select 6 illustrative combinations of progenitor galaxies (2xSa, Sa_Sc, Sa_Sd, 2xSc, Sc_Sd, 2xSd), and for the 3:1 mass ratio mergers I choose one high mass progenitor of each type and merge it with the lower mass Sc galaxy giving three further combinations (Sa_Scp3, Sc_Scp3, Sd_Scp3). Each pair is set on 3 different orbits G00, G07, and G13 (Section 2.1.5), giving 18 equal-mass and 9 unequal-mass merger simulations in total. The exhaustive table of the parameters for the merger simulations can be found in the Appendix (Table 2.2).

Each merger simulation is run for 3 Gyr until the current cosmic time $t = 13.7\,\mathrm{Gyr}$. Snapshots are output every 2×10^7 years, giving 150 snapshots per simulation.

Table 2.2: Parameters for the merger simulations, where i is the inclination relative to the orbit plane, ω is the argument of the orbits' pericentre. For the equal-mass mergers (1:1) the initial separation is $r_{\rm sep} = 225\,$kpc, the pericentre distance is $r_p = 7.6\,$kpc. For the unequal-mass mergers (3:1), the initial separation is $r_{\rm sep} = 135.5\,$kpc, and the pericentre distance is $r_p = 6.5\,$kpc.

Equal-mass mergers

Simulation	First galaxy	Second galaxy	Orbit	i_1	i_2	ω_1	ω_2
2xSa_00	Sa	Sa	G00	0°	0°	0°	0°
2xSa_07	Sa	Sa	G07	−109°	71°	−60°	−30°
2xSa_13	Sa	Sa	G13	−109°	180°	60°	0°
2xSc_00	Sc	Sc	G00	0°	0°	0°	0°
2xSc_07	Sc	Sc	G07	−109°	71°	−60°	−30°
2xSc_13	Sc	Sc	G13	−109°	180°	60°	0°
2xSd_00	Sd	Sd	G00	0°	0°	0°	0°
2xSd_07	Sd	Sd	G07	−109°	71°	−60°	−30°
2xSd_13	Sd	Sd	G13	−109°	180°	60°	0°
Sa_Sc_00	Sa	Sc	G00	0°	0°	0°	0°
Sa_Sc_07	Sa	Sc	G07	−109°	71°	−60°	−30°
Sa_Sc_13	Sa	Sc	G13	−109°	180°	60°	0°
Sa_Sd_00	Sa	Sd	G00	0°	0°	0°	0°
Sa_Sd_07	Sa	Sd	G07	−109°	71°	−60°	−30°
Sa_Sd_13	Sa	Sd	G13	−109°	180°	60°	0°
Sc_Sd_00	Sa	Sd	G00	0°	0°	0°	0°
Sc_Sd_07	Sa	Sd	G07	−109°	71°	−60°	−30°
Sc_Sd_13	Sa	Sd	G13	−109°	180°	60°	0°

Unequal-mass (3:1) mergers

Simulation	First galaxy	Second galaxy	Orbit	i_1	i_2	ω_1	ω_2
Sa_Scp3_00	Sa	Scp3	G00	0°	0°	0°	0°
Sa_Scp3_07	Sa	Scp3	G07	−109°	71°	−60°	−30°
Sa_Scp3_13	Sa	Scp3	G13	−109°	180°	60°	0°
Sc_Scp3_00	Sc	Scp3	G00	0°	0°	0°	0°
Sc_Scp3_07	Sc	Scp3	G07	−109°	71°	−60°	−30°
Sc_Scp3_13	Sc	Scp3	G13	−109°	180°	60°	0°
Sd_Scp3_00	Sd	Scp3	G00	0°	0°	0°	0°
Sd_Scp3_07	Sd	Scp3	G07	−109°	71°	−60°	−30°
Sd_Scp3_13	Sd	Scp3	G13	−109°	180°	60°	0°

2.1.6 Parameters for the merger simulations

We run 18 equal-mass and 9 unequal-mass merger simulations each with 3 different orbits, giving 27 merger simulations summarised in Table 2.2.

2.2 The SIMBA simulation

In this project, I study the SIMBA cosmological hydrodynamic simulation (Davé et al., 2019), the next generation of the MUFASA simulation (Davé et al., 2016). Like MUFASA, SIMBA employs a forked version of GIZMO, a mesh-less finite mass hydrodynamics code (Hopkins, 2015) based on Gadget-3 (Springel, 2005). Like MUFASA, SIMBA uses a set of state-of-the-art sub-resolution prescriptions, including H_2 based star formation rate (Krumholz & Gnedin, 2011), supernova feedback, star formation-driven galactic winds, a chemical enrichment model that tracks 11 elements, radiative cooling and photoionisation heating. These models are slightly updated to match the recent theoretical and observation results (see Davé et al., 2019 for more details).

The major updates of SIMBA compared to MUFASA are in two aspects. Firstly, SIMBA has a better and more realistic treatment to dust compared with MUFASA, the new model deals with on-the-fly dust production, growth and destruction. Secondly, the super massive black hole (SMBH) accretion and feedback models have been improved. Davé et al. (2019) describes the improved accretion model which deals with gas of different temperatures. Hot gas with a temperature of $T > 10^5$K that is not part of the interstellar medium is accreted onto the central black hole via the standard BondiHoyleLyttleton accretion mode (Bondi, 1952). The cold gas accretion is driven by gravitational torques of the accretion disc (Hopkins & Quataert, 2011). SIMBA adopts two different SMBH feedback models, depending on the Eddington ratio. If the SMBH is in a high Eddington ratio state ($f_{\rm Edd}$>0.2), the SMBH will feedback via radiative AGN winds, eject gas without heating it or changing its temperature. This is broadly similar to the AGN model introduced in Anglés-Alcázar et al. (2017). In the low Eddington ratio state the AGN feedback transitions to a jet mode, in which the outflow velocity is strongly increased. The feedback becomes entirely jet mode when the Eddington ratio is lower than 0.02 and SMBH mass is higher than $10^{7.5}$ $M_\odot$. Davé et al. (2019) showed that massive quiescent galaxies are primarily quenched by the jet feedback from the SMBH at the galaxy centre.

I use the fiducial run of the SIMBA simulation suite, which has a box length of 100 comoving h^{-1} Mpc and a minimum gravitational softening length of 0.5 comoving h^{-1} kpc. The simulation has 2×1024^3 particles, with equal numbers of baryonic and dark matter particles. The particle mass resolution is 9.6×10^7 $M_\odot$for dark matter and 1.2×10^7 for the initial gas particles. In the fiducial run, the simulation begins at a redshift of $z = 249$ and ends at $z = 0$, thus

simulating present day Universe. The first snapshot is output at $z = 20$ and snapshots are then output with a time spacing that is comparable to galaxy dynamical timescales, which yields 151 snapshots in total. We are interested in the redshift range of $z = 2$ to $z = 0.5$, where the snapshots have a time spacing of ~ 100 Myr and ~ 150 Myr respectively. SIMBA takes a Planck Collaboration XIII (2016) concordant cosmology of $\Omega_m = 0.3$, $\Omega_\Lambda = 0.7$, $\Omega_b = 0.048, H_0 = 68$ km s^{-1} Mpc^{-1}, $\sigma_8 = 0.82$ and $n_s = 0.97$.

We use the CAESAR[2] package to resolve the galaxies by firstly grouping stars and interstellar medium (ISM) gas into baryonic galaxies via a 6D friends-of-friends (FOF) algorithm. The FOF adopts a spatial linking length of 0.0056 times the mean inter-particle spacing and a velocity linking length of the local velocity dispersion. A resolved galaxy has a minimum number of 32 particles, which yields a minimum stellar mass of 5.8×10^8 M$_\odot$.

Many galaxy properties in SIMBA are in good agreement with observations (Davé et al., 2019). A wide range of galaxy statistics are well reproduced, including the galaxy stellar mass function evolution, and the star-forming main sequence (giving a good match at $z = 0$ as a function of stellar mass.) etc. The great agreement between SIMBA and observations makes SIMBA an ideal platform for investigating the specific physical processes driving galaxy evolution in more detail.

[2] `https://caesar.readthedocs.io/en/latest/`

3

The SEDMORPH CODE

Our group has been developing the SEDmorph code[1] standing for *Spectral Energy Distribution and morphology*, to turn the particle data from simulations into mock datasets. I developed and extended this code to create integral field datacubes following the MaNGA observational strategy. I created stellar continuum with the BC03 spectral synthesis models and apply a two-component dust attenuation model. A seeing (atmospheric) point spread function (PSF) and a dither pattern are included when building the row stacked spectrum (RSS) files. Finally, I combine the RSS into a regularly gridded datacube. The mock galaxies are placed at a redshift of $z \sim 0.04$, close to the median redshift of the MaNGA survey. The 1 arcsec radius MaNGA fibres are equivalent to 0.79 kpc at this redshift. Thanks to the methods and settings, our mock datacubes closely match the properties of the MaNGA survey. In this chapter, I provide details on the components of the code that are developed by me and used in the binary merger simulations in this thesis.

[1]The project web page: `https://github.com/SEDMORPH`. The code for mock datacube creation `https://github.com/SEDMORPH/YZCube`.

3.1 Stellar continuum creation

To build the stellar continuum spectra I use the Bruzual & Charlot (2003, BC03 hereafter) spectral synthesis models, updated in 2016[2]. These models provide integrated light spectra for simple stellar populations (SSPs) which represent coeval, single metallicity stellar populations, assuming an initial mass function (IMF), evolutionary tracks and stellar input spectra. This version of the BC03 models are built from both observed and theoretical stellar spectra, assuming a Chabrier (2003) IMF and "Padova-1994" evolutionary tracks (Alongi et al., 1993; Bressan et al., 1993; Fagotto et al., 1994a,b; Girardi et al., 1996). The observed spectra most relevant for the wavelength range of the MaNGA spectra are taken from the MILES stellar library (Sánchez-Blázquez et al., 2006; Falcón-Barroso et al., 2011) in the wavelength range 3540Å- 7350Å, extended with the STELIB stellar library (Le Borgne et al., 2003) out to 8750Å.

I assume that each stellar particle in the simulations is composed of a single coeval, fixed metallicity stellar population, with an age and metallicity corresponding to when the progenitor gas particle becomes a stellar particle. The SSPs have already been interpolated onto an optimum age grid, I therefore refrain from any further interpolation in age and each stellar particle is assigned the closest SSP in age. The BC03 models provide SSPs for seven different metallicity values (with metal mass fractions of Z =0.0001, 0.0004, 0.004, 0.008, 0.02, 0.05, 0.1, where $Z_\odot = 0.02$). The metallicity distribution of particles in the simulations is such that most particles have metallicities in the 2 bins around solar metallicity ($0.08 < Z < 0.05$), which is not sufficient to accurately reproduce the changes in spectral indices caused by the metallicity gradient of the galaxies (see Figure 3.1 for the gradient in the left panel and for the metallicity distribution in the right one). I therefore decided to interpolate the spectra between the central metallicity bins. For a targeted new Z value (marked as Z_t for *target*), I find the two closest Z values (marked as Z_l and Z_u for *lower* and *upper*) in the original BC03 models that meet with $Z_l < Z_t < Z_u$. A linear interpolation is employed in log flux at each wavelength λ in the model spectra:

$$\lg T(\lambda) = \lg L(\lambda) + \frac{Z_t - Z_l}{Z_u - Z_l}(\lg U(\lambda) - \lg L(\lambda)) \tag{3.1}$$

where L, T and U is the luminosity density of the lower, target and upper Z models at λ respectively.

[2]These are available at `http://www.bruzual.org/~gbruzual/bc03/Updated_version_2016/`

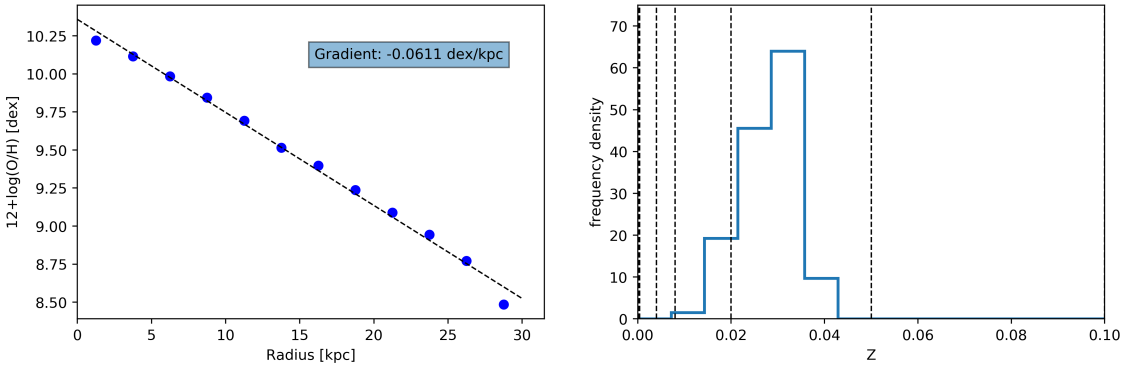

Figure 3.1: Metallicity distribution. *Left panel:* the metallicity gradient that is set up in the galaxies in the 2xSc_07 simulation at the beginning of the simulation. *Right panel:* the frequency density distribution as a function of Z. Dash lines are the Z values available in the BC03 models. Most particles have a Z value between 0.008 and 0.05, which motivates me to interpolate between models with different Z values.

The equation naturally creates the interpolated spectrum “between" the two original ones. An example is given in the left panel of Figure 3.2: the interpolated spectrum $Z = 0.035$ (black) stays somewhere between the two original ones (blue and orange for $Z = 0.02$ and $Z = 0.05$ respectively). I further verify the success of the interpolation by computing the H$\delta_{\rm A}$ and H$\gamma_{\rm A}$ spectral indices of the 1 Gyr old interpolated spectrum, finding that the indices vary smoothly between the new SSPs as expected. This result can be found in the right panel of Figure 3.2.

The interpolation is aimed to distribute the stellar particles between metallicity bins as equally as possible. This leads to additional SSPs with $Z = 0.012$, 0.016, 0.023, 0.026, 0.035 and 0.04 besides the original seven ones.

The stellar particles contain 11 different elements as described in Section 2.1.1. I calculate the metallicity of each stellar particle as $Z_* = (1 - M_H - M_{He})/M_*$, where M_H and M_{He} are the total masses of Hydrogen and Helium respectively and M_* is the mass of the star particle, and assign the closest interpolated SSP in metallicity. Finally, the integrated spectrum (luminosity density) of the simulated galaxy or part thereof, can be written as:

$$l_\lambda = \sum_{i=1}^{N_*} M_i \times l_{\lambda,SSP}(t_{SSP,i}, Z_{SSP,i}) \tag{3.2}$$

where M_i is the mass of the stellar particle, $l_{\lambda,SSP}$ is the luminosity density of the assigned SSP and the sum is over all relevant star particles in the region of interest.

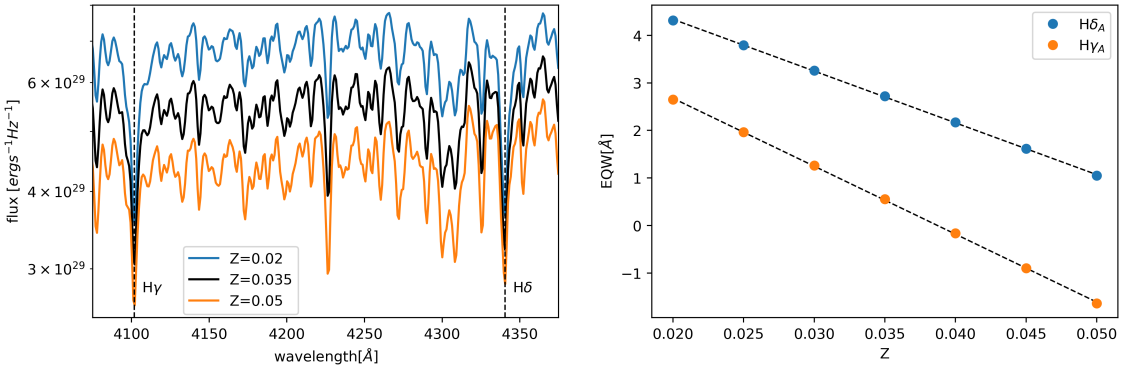

Figure 3.2: Checking the interpolated spectra. *Left panel:* The interpolated spectrum $Z = 0.035$ (black) stays somewhere between the two original ones ($Z = 0.02$ and $Z = 0.05$) and has a proper shape. To keep the figure clean, only the wavelength region around H_γ and H_δ abortion lines is shown, and only the spectra of an SSP with an age of 1 Gyr is plotted. *Right panel:* the equivalent widths of the H_γ and H_δ absorption lines in the spectra of the SSP with an age of 1 Gyr. The perfect linear fitting between interpolated models and original models at $Z = 0.02$ to 0.05 shows that the interpolation is reasonable.

3.2 Dust attenuation model

I employ a two-component dust attenuation model (Charlot & Fall, 2000; Wild et al., 2007) in which the optical depth is contributed by the interstellar medium for all stars, as well as stellar birth clouds for stellar populations younger than 10^7 years. The final effective optical depths as a function of wavelength for young and old stellar populations are thus given by:

$$\begin{aligned} \hat{\tau}_{young} &= \mu_d \tau_v \left(\frac{\lambda}{5500}\right)^{-0.7} + (1-\mu_d)\,\tau_v \left(\frac{\lambda}{5500}\right)^{-1.3} \\ \hat{\tau}_{old} &= \mu_d \tau_v \left(\frac{\lambda}{5500}\right)^{-0.7} \end{aligned} \tag{3.3}$$

where λ is the wavelength in Å, μ_d is the fraction of optical depth contributed by the ISM, which is set as 0.3 and τ_v is the effective optical depth at 5500Å, which I set to a fiducial value of 1.0, typical for local star-forming galaxies.

I note that by not using radiative transfer to calculate the attenuation I am not correctly accounting for the full 3D geometry of the stars and gas in the mock galaxies. Additionally, I do not attempt to link dust content to the metallicity of the gas particles. However, I choose this approach to avoid further sub-resolution recipes given the relatively high mass of the individual gas and star particles compared to giant molecular clouds in which stars are formed in reality. It is important to keep in mind the limitations of any dust modelling in mock galaxies with this level of spatial resolution.

3.3 Different spectra strategies

In relatively low resolution simulations (e.g. 10^6 $M_\odot$ for baryon particles), it is suggested that the poor sampling of star formation can adversely affect luminosities of simulated galaxies (e.g. Trayford et al., 2015). A single recently formed star particle can significantly change the spectrum, image and colour of the galaxy. Thus, carefully adding the contribution from star-forming gas particles is proposed to mitigate this numerical artefact in their works (Wild et al., 2009; Trayford et al., 2015; Lahén et al., 2018).

In my simulations, I notice that the instantaneous SFR does not match the increasing of galaxy stellar mass. In Figure 3.3, I derive the SFH via two different methods. The black line records the sum of SFRs of the gas particles at each snapshot, which represent the instantaneous SFR at the time of snapshot. The red line is the SFH derived by the increasing of stellar mass between the snapshots. It can be seen that the two SFHs differ from each other when there are fluctuations in the instantaneous SFR. This difference may lead to different observational properties, which motivated me to consider including light from star-forming gas particles. In this section, I describe 3 different strategies to include the contribution from gas and compare their results to those from the strategy that exclude the gas contribution, the one introduced in section 3.1.

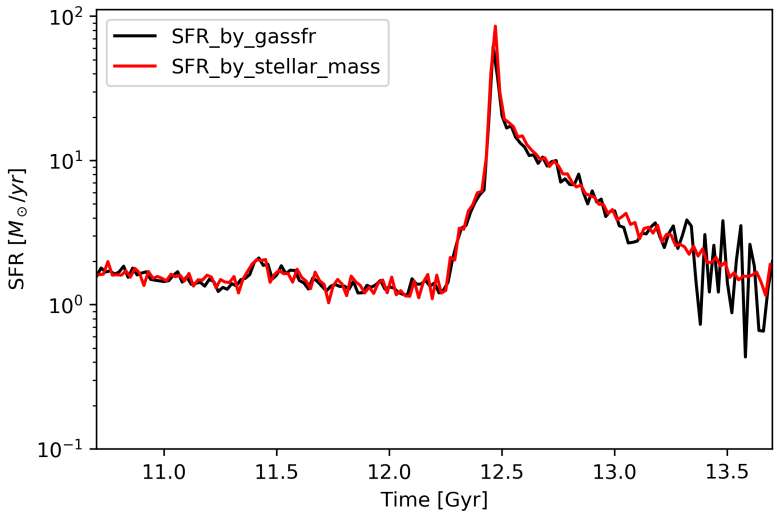

Figure 3.3: SFH derived via different methods. The black line records the sum of SFRs of the gas particles at each snapshot, which represent the instantaneous SFR at the time of snapshot. The red line is the SFH derived by the increasing of stellar mass between the snapshots. It can be seen that the two SFHs differ from each other when there are fluctuations in the instantaneous SFR.

The method adopted in the SEDmorph code to include the light of these star-forming gas particles is detailed below. For each gas particle, its SFR at each snapshot is recorded and assumed to remain constant for 20 Myr, which is the time spacing between two snapshots. The gas particle is supposed to spawn a stellar particle at each snapshot with a mass of its (SFR×20 Myr) and a corresponding age of the snapshot. I then assign an SSP to the "phantom" stellar particles and sum up their total light. I remind that these "phantom" stellar particles do not exist in the simulations and they are only assumed for the convenience to calculate the light of star-forming gas particles. For the stellar particles converted during the simulations, the SFH of their progenitor gas particles are also recorded, and the same process is applied to include contribution that the particles made before their transition from gas status into stellar ones. This method is coded as *YZ_gas* for easier reference in the following text.

Besides the *YZ_gas* method, I also improve the SEDmorph code to adopt the method that Trayford et al. applied to their analysis in the EAGLE (Schaye et al., 2015) simulation. In this *EAGLE* method, we assume each gas particle and recently formed star particle (age $<$ 100 Myr) has a constant SFR for the preceding 100 Myr. Similar to that in the *YZ_gas* method, the gas particles and young stellar particles are also assumed to spawn "phantom" stellar particles but at the ages of the simple stellar population of younger than 100 Myr. For the "phantom" stellar particles produced by gas particles, their masses are set to be the (particle SFR× age spacing between SSPs); while for those produced by young star particles, their masses are tuned to conserve the total mass of the particle. In this *EAGLE* method, the old stars (age $\geq$ 100 Myr) are treated with methods described in section 3.1. *EAGLE_minus*, a revised version, is also included, in which I remove the contribution from young stars (age $<$ 100 Myr) while keep everything else the same to the original *EAGLE* method. The strategy used in section 3.1 does not count the light from the gas particles but the stellar ones only. Hence, I code it as *star_only*.

To figure out which one of these four strategies is the best choice of the code, I carry out comparisons of SFH, UV flux and spectra indices. Here, I focus on a specific simulation, 2xSa_07_noBH. It is an equal mass merger of two Sa type galaxies using orbital configurations 07, i.e. prograde-retrograde. Note that the black hole feedback is turned off in this simulation. It is also the simulation displayed in Figure 3.3.

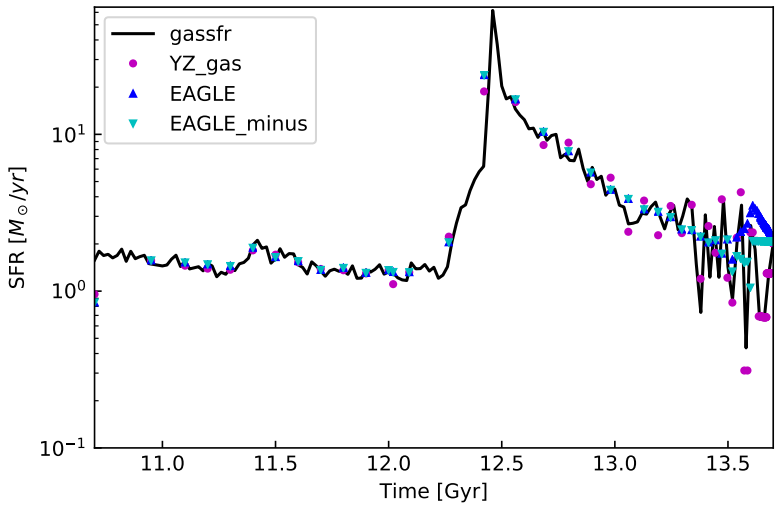

Figure 3.4: Comparing the SFHs recovered by different strategies. Only the *YZ_gas* method picks up the violent fluctuations seen in the gassfr, which suggests that the *YZ_gas* method is the most sensitive to instantaneous SFR. The *EAGLE* method causes a strange bump in the recent 200 Myr, which is introduced by double-counting of the contribution to SFR from recently formed stars and that from gas particles. The *EAGLE_minus* method successfully removes the unphysical bump structure but causes a flat SFH in the recent 100 Myr.

3.3.1 Star Formation History

It is critical to get the correct star formation history for stellar population synthesis. Hence, I first check the recovered SFHs from the three methods that include the gas contributions and compare the results to the SFH derived by the sum of SFRs of the gas particles at each snapshot (coded as *gassfr* for easier reference). In Figure 3.4, I use the snapshot at $t = 13.7$ Gyr of the 2xSa_07_noBH simulation, and compute the SFH during the entire simulation, from $t = 10.7$ to $t = 13.7$ Gyr. The *gassfr* is plotted as the black line while the SFHs recovered by different strategies are plotted with points of different types and colours. Only the *YZ_gas* method picks up the violent fluctuations seen in the gassfr, which suggests that the *YZ_gas* method is the most sensitive to instantaneous SFR. The *EAGLE* method causes a strange bump in the recent 200 Myr, with a peak 100 Myr ago. As described above, recently formed star particles (age $<$ 100 Myr) are assumed to have a constant SFR in the preceding 100 Myr before the time they convert from gas into stars. Such a solution double-counts the contributions of young stars with the star-forming gas particles that have a constant SFR in the recent 100 Myr. It also spreads the mass of the young stars into the recent 100–200 Myr, which again overlaps with the old stars at that age range. Thus, we see a bump in the recent 200 Myr, with a peak 100 Myr ago. Clearly, the *EAGLE* strategy will result an overestimation of the recent star formation rate. The *EAGLE_minus* method successfully removes the unphysical bump structure since the

contribution from young stars (age < 100 Myr) is removed. However, it causes a flat SFH in the recent 100 Myr and fail to reflect the dramatic change in the SFR, which can be critical during the starburst phase. The effect is easy to spot when we analyse the data at $t = 12.5$ Gyr (see cyan triangles in Figure 3.5). The *star_only* method is not included in this comparison as its SFH has been shown in Figure 3.3, in which we find that it is smoother than the instantaneous *gassfr*.

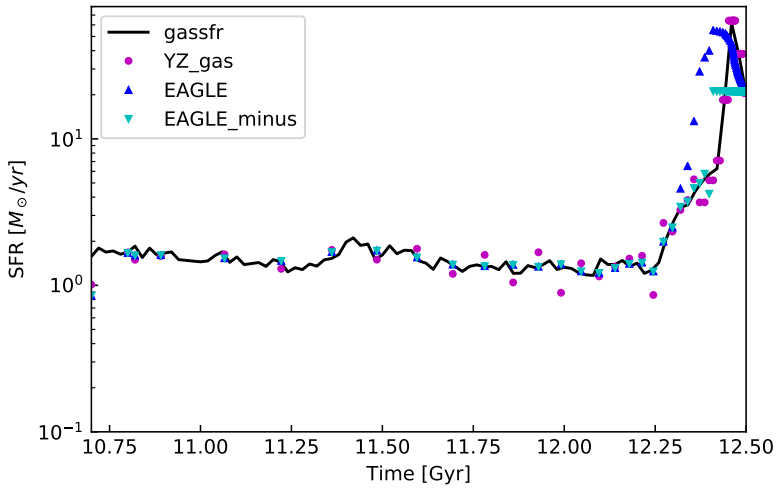

Figure 3.5: Same as Figure 3.4 but with the data at $t = 12.5$ Gyr, at which the galaxy is at a strong starburst.

The *EAGLE* and *EAGLE_minus* method have worse performance comparing with the *YZ_gas* method. The *star_only* method does not reflect the violent fluctuations of instantaneous SFR that can be picked up by the *YZ_gas* method. However, it is *not* safe to conclude that *YZ_gas* is better than *star_only* as the fluctuations of instantaneous SFR may not be reflected in observations.

3.3.2 UV flux

Here I check the UV flux in the spectra created by different strategies. The UV flux reflects the recent star formation history and is commonly used to estimate the SFR. For each snapshot, I measure the average UV flux density between 1500-2800Å and plot the UV flux evolution as a function of time with coloured line in Figure 3.6. The black is directly converted from *gassfr*, which I will come back to later. Here, I focus on the different results of the four spectra strategies. The *EAGLE* method systematically produces higher UV flux, which is a natural result of double counting and of overestimating on SFR. The *EAGLE_minus* method does a better job but gives a weird dip around 12.5 Gyr. Both *EAGLE* and *EAGLE_minus* show strong

fluctuations in the last half Gyr of the simulation. The *YZ_gas* and *star_only* method yields very similar results except that UV flux given the *YZ_gas* method fluctuates by a very small amplitude.

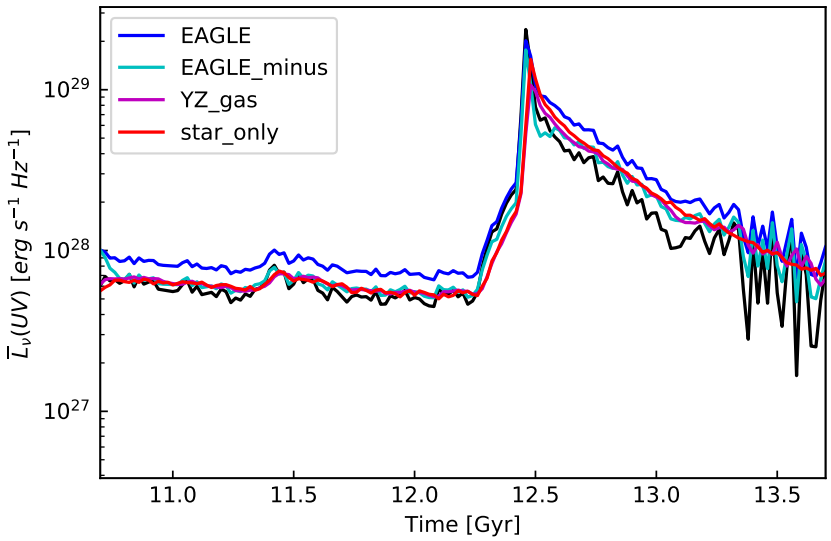

Figure 3.6: Comparison of the evolution of average UV flux as a function of time.

To convert *gassfr* into UV flux, I follow the idea in Kennicutt (1998). In this paper, the authors promote that the UV flux can be estimated by the equation below if the galaxy that has constant SFR over 10^8 yr:

$$L_\nu(erg\ s^{-1}Hz^{-1}) = 3.838 \times 10^{27} \times SFR(M_\odot/yr) \tag{3.4}$$

Note that my conversion factor is different from the original one. Kennicutt (1998) employed a Salpeter IMF and a dust-free galaxy model(Madau et al., 1998), while the SEDmorph adopts Chabrier IMF and two-component dust model. Hence, I calculate my own conversion factor using GALAXEV [3]. GALAXEV gives the SED of an evolving composite stellar population(CSP). Each CSP represents a galaxy that has a constant of $1M_\odot/yr$ SFR over the age of the CSP. The UV flux of the CSP (or galaxies) increases as the age of CSP grows at first and then becomes stable when the age of the CSP is several Gyr or older. The UV flux of the oldest CSP stays around $3.838 \times 10^{27}\ erg\ s^{-1}Hz^{-1}$(see Figure 3.7, giving the conversion factor in Equation 3.4.

In Figure 3.7, I notice that the UV flux takes longer than 10^8 yr to reach the flat phase than

[3]GALAXEV combines SSPs to build a spectrum, given on input SFH. Relative links: code at `http://www.bruzual.org/~gbruzual/src.tgz`code, introduction at `http://www.bruzual.org/~gbruzual/bc03/doc/bc2003.pdf`, authors' homepage at `http://www.bruzual.org`.

suggested in Kennicutt (1998). Hence, the conversion should not be used to estimate the UV flux during the starburst phase or at the time when the SFR fluctuates by a lot. In Figure 3.6, the UV flux converted from *gassfr* matches others before the starburst around $t = 12.5$ Gyr, but is too low after that, which confirms the limitation of conversion. Since the UV flux takes a long time to flatten up, fluctuations in the instantaneous SFR of short timescales is expected to be smoothed to some extent. In Figure 3.3, the instantaneous *gassfr* fluctuates with a timescale of ~ 0.05 Gyr. However, I warn that the *gassfr* has a coarse sampling, which is 0.02 Gyr, the time-spacing of snapshots. To better identify the fluctuation in the SFR, I look at the SFR log file output by the SPHGal and find that the instantaneous SFR roughly vibrates between 0.5 $M_{\odot}/yr$ and 5 $M_{\odot}/yr$ in triangle wave format with a period of **only** ~ 0.01 **Gyr**. In order to check whether such a fluctuation in SFR can be reflected in the fluctuation in UV flux, I construct a toy galaxy with a constant SFR of 2 $M_{\odot}/yr$ in the past 5 Gyr, then the SFR of the galaxy fluctuate in the next 1 Gyr in the same behaviour observed in the 2xSa_07_noBH: between 0.5 $M_{\odot}/yr$ and 5 $M_{\odot}/yr$ in triangle wave format with a period of ~ 0.01 Gyr. I calculate the UV flux of the toy galaxy and find that the UV flux remains almost constant though its SFR keeps changing. As the toy model suggested, the fluctuations picked up by the *EAGLE* and *EAGLE_minus* methods may not be resolved in real observations. During the comparison of UV flux, the *star_only* and *YZ_gas* methods show their advantage again as well as their similarity.

3.3.3 Principal Component Analysis Results

Principal Component Analysis (PCA) is applied to the mock stellar continuum in order to identify the post-starburst galaxies in the binary merger simulations in this thesis. Hence, it could be useful to compare the performance of different spectra strategies in the PCA results.

For each snapshot of 2xSa_07_noBH simulation, I measure the spectral indices, plot the evolution trace in PC1-PC2 space. The results are shown in Figure 3.8. The *star_only* method is plotted in white dot-lines in all the panels while the other methods are plotted in coloured dot-lines with the colour indicates the time of the corresponding snapshot. The grey contour is the SDSS DR7 galaxy distribution in PC1-PC2 space [4] (Wild et al., 2007), which allows me to compare my simulation to observations.

The left panel of Figure 3.8 shows the PCA trace comparison between the *EAGLE* method

[4] `http://www-star.st-andrews.ac.uk/~vw8/downloads/DR7PCA.html`

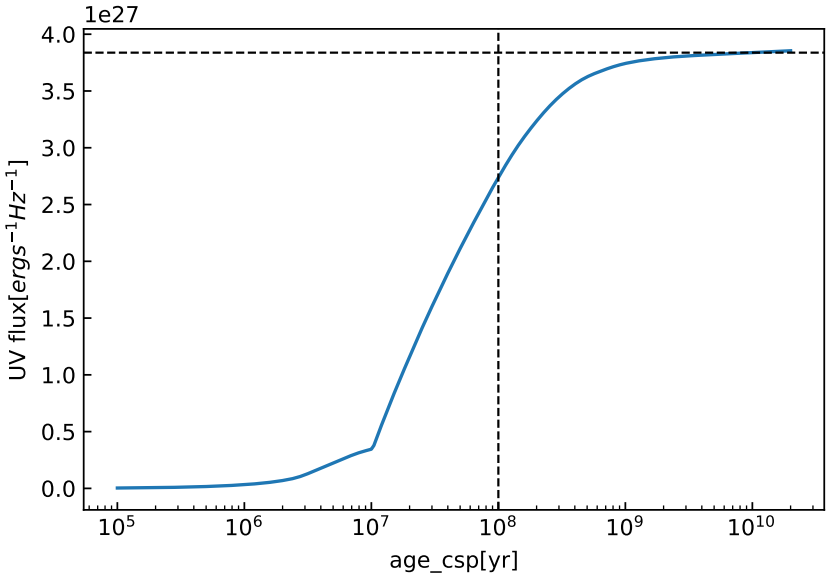

Figure 3.7: The UV flux evolution of the CSP as a function of CSP age. The UV flux of the oldest CSP in dusty model stays around $3.838 \times 10^{27}\ erg\ s^{-1}Hz^{-1}$, which indicates that a galaxy that keeps a constant SFR of $1 M_{\odot}/yr$ over a long period yields a UV flux of $3.838 \times 10^{27}\ erg\ s^{-1}Hz^{-1}$. I note that the UV flux takes longer than 10^8 yr to reach the flat phase than suggested in Kennicutt (1998)

(colourful dot-line) and the *star_only* method (white dot-line). Overall the *EAGLE* PCA trace is offset to the left due to its overestimation of SFR. At the end of the PCA trace, the *EAGLE* trace picks up more violent fluctuations, similar to the UV flux evolution. The middle panel of Figure 3.8 compares the *EAGLE_minus* with *star_only* methods. Unlike the trace of the original *EAGLE* method, the *EAGLE_minus* trace does not offset to the left as it avoids double counting young stars and gas . However, the *EAGLE_minus* traces differ from the *star_only* one between 12.2–12.5 Gyr, i.e. during the starburst phase when the SFR have significant increasing in a short time. The *EAGLE_minus* natural flatten the star-burst strength due to the assumption that each star-forming gas particle has a constant SFR for the preceding 100 Myr. The right panel compares *YZ_gas* method to the *star_only* method. The *star_only* trace is slightly smoother than the *YZ_gas* one, but overall they are basically the same and hard to distinguish.

3.3.4 Comparison Summary

Here I sum up the comparison results of this section. The *EAGLE* strategy causes a weird bump in the recovered SFH, significantly produce too much UV flux and is offset to the left in PCA trace. I decide to exclude the *EAGLE* method from the choices because its performance indicates its double counting young stars and gas. As an improved version, the *EAGLE_minus* method works much better in the SFH and UV flux. However, it flattens the star-burst phase

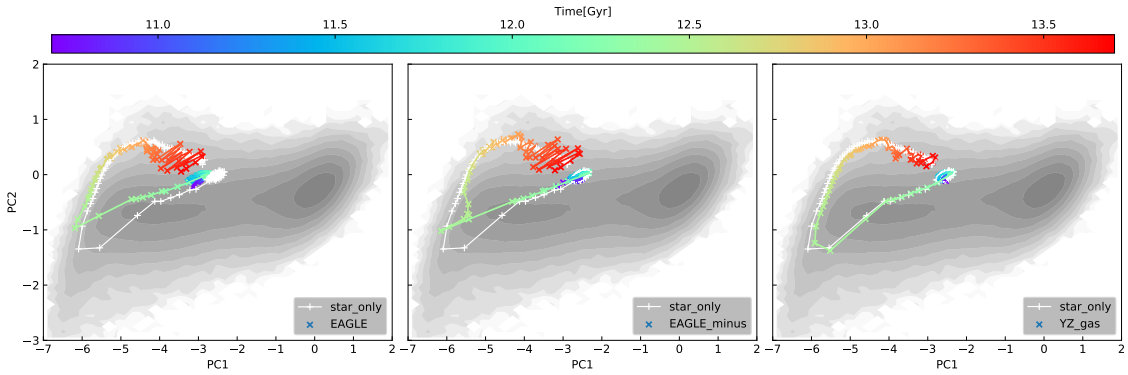

Figure 3.8: PCA trace. The grey contour shows the SDSS DR7 galaxy distribution in PC1-PC2 space. The white dot-lines in all panels represent the *star_only* method, working as the comparison base. The left panel shows that the *EAGLE* PCA trace is offset to the left significantly compared with the *star_only* method. The middle panel shows that the *EAGLE_minus* trace does not have the right shape around 12.2–12.5 Gyr as discussed in the text. The right panel shows that *star_only* trace overlaps the *star_only* one quite closely. The colour bar on the top indicates the age of points in the figures.

in the SFH, has a weird dip in its UV flux evolution and strange shape of PCA trace. The *EAGLE_minus* method is excluded as well. The *YZ_gas* method has a quite similar performance to the *star_only* method; they overlap each other quite well in both UV flux evolution and PCA trace. However, *star_only* is more convenient, easier and faster than *YZ_gas*, hence a better solution. The conclusion of this section is that including the light from the star-forming gas particles is *not* necessary for simulations with the resolution of/better than $m_{baryon} \sim 10^5 M_\odot$. Through out this thesis, the *star_only* is applied for creating stellar continuum.

3.4 Datacube creation

3.4.1 MaNGA observing strategy

In order to analyse the spatially resolved properties of the simulated galaxies, I developed and extended the SEDmorph code to create integral field datacubes following the MaNGA observational strategy. MaNGA, Mapping Nearby Galaxies at Apache Point Observatory, [5] is a galaxy integral-field spectroscopic survey, one of three core projects in the fourth-generation Sloan Digital Sky Survey (SDSS-IV) (Bundy et al., 2015). MaNGA uses integral field unit (IFU) spectroscopy to obtain spectra from different regions of a galaxy with a spatial resolution of 1.3 – 5.1 kpc and a spectral resolution R $\sim$ 2000, covering the wavelength range from 3600 to 10000 Å. This ability allows astronomers to map the composition and kinematics of gas and stars and have new insights into galaxy formation and evolution. The MaNGA instrument

[5]MaNGA homepage: `http://www.sdss.org/surveys/manga`

is a multi-object integral-field unit spectrograph, making the MaNGA survey highly effective and productive. MaNGA has observed over 10,000 nearby galaxies ($0.01 < z < 0.15$) with the integral field spectroscopy and released the complete data set in 2021 (Abdurro'uf et al., 2021).

The observing strategy for MaNGA is described in detail in Law et al. (2015), and the data reduction pipeline (DRP) is introduced in Law et al. (2016). Here I briefly summarise the critical details related to the creation of the mock MaNGA datacubes. MaNGA has 17 individual fibre IFU, in which the fibres are hexagonally packed. The MaNGA IFUs range in size from 12 arcsec diameter (19 fibres) to 32 arcsec diameter (127 fibres). A schematic diagram of the 7 central fibres within a hexagonally packed MaNGA IFU is displayed in the left panel of Figure 3.9. The sampling irregularities from fibre-bundle IFUs can result in substantial interstitial light losses (e.g., Sánchez et al., 2012; Sharp et al., 2015). Hence, MaNGA includes dithered observations to overcome the problem. A fixed triangular three-point dithering scheme is adopted to effectively fills the interstitial regions, which is naturally suggested by the geometry of the hexagonal fibre arrangement. The relative positions of the three dither positions adopted in MaNGA are illustrated in the triangular figure in the left panel of Figure 3.9, while the coverage pattern at 5500 Å of three dithered observations is shown in the right panel. In each MaNGA observation, the number of dither sets depends on the time it takes to reach the target depth, leading to an integer multiple of 3 exposures (3,6,9,12, etc.).

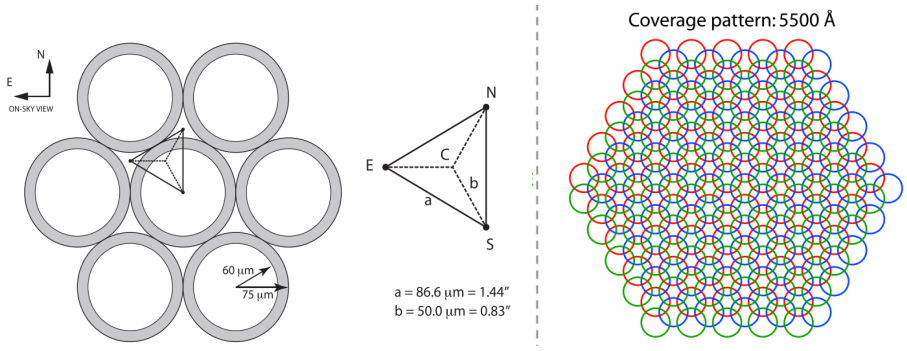

Figure 3.9: *Left:* Schematic diagram of the 7 central fibres within a hexagonally packed MaNGA IFU. The triangular figure displays the relative positions of the three dither positions; the fibre bundle is located at position "S". The central (C) "home" position is labelled, along with the north (N), south (S), and east (E) dither positions. *Right:* The coverage pattern at 5500 Å of three dithered observations. Figures obtained and reorganised from Law et al. (2015).

After the observation, the spectra from all the fibres and exposures for a given galaxy or target are fully reduced into Row-stacked spectra files (RSS, i.e., a 2D array in which each row corresponds to an individual 1D spectrum)). Using the RSS files and associated astrometric

solutions (see Section 8 of Law et al., 2016), the individual fibre spectra are combined into rectilinearly gridded cubes with a spatial pixel scale of 0.5 arcsec pixel^{-1}. The combination takes a circular Gaussian weight function. The relative contribution of i'th fibre to the j'th output square pixel is determined by the function below:

$$w[i,j] = b[i] \exp\left(-0.5 \frac{r[i,j]^2}{\sigma^2}\right) \tag{3.5}$$

where $\sigma = 0.7$ arcsec is an exponential scalelength, $r[i,j]$ is the distance between the i'th fibre location and the j'th output pixel, and $b[i]$ is a binary integer equal to zero where the inverse variance $g[i]^{-1} = 0$ and one elsewhere. Additionally, the weight is set to be $w[i,j] = 0$ for all $r[i,j] > r_{\rm lim} = 1.6$ arcsec as an upper limit on the radius of influence of any given measurement. The weight function is further normalized to conserve flux. The final weight function is, therefore:

$$W[i,j] = \frac{w[i,j]}{\sum_{i=1}^{N} w[i,j]} \tag{3.6}$$

in which N is the length of the one-dimension vector $f[i]$ of the input intensity data, $N = N_{\rm fibre} \times N_{\rm exp}$ where $N_{\rm fibre}$ is the number of fibres in the IFU (e.g., 127) and $N_{\rm exp}$ is the total number of exposures to combine together. In the cases that $w[i,j] = 0$ for all i in the range 1 to N (e.g., outside the hexagonal footprint of the IFU), $W[i,j]$ is set to be 0 to avoid dividing by zero errors.

By computing the matrix product of the normalized weights and the input intensity vector, the intensity distribution of the pixels in the output image can be given out as:

$$F = \alpha W \times f = \alpha \begin{bmatrix} W_{11} & \dots & W_{N1} \\ \vdots & \ddots & \vdots \\ W_{1M} & \dots & W_{NM} \end{bmatrix} \times \begin{bmatrix} f_1 \\ \vdots \\ f_N \end{bmatrix} \tag{3.7}$$

where $\alpha = 1/(4\pi)$ is a constant factor to account for the conversion from flux per unit fibre area (π arcsec^2) to flux per unit spaniel area (0.25 arcsec^2). The final step is to loop the process described above over the wavelength dimension, and the 3D datacube can be then constructed from the RSS files.

3.4.2 Creation of mock MaNGA datacubes

The first step in creating mock datacubes is to locate the centre of the simulated galaxies in each snapshot. For simulations with black holes I simply take the position of the supermassive black hole as the centre of the galaxy as the black hole is repositioned to the minimum of the potential at every time step. For the simulations without black holes I use the distribution of dark matter particles to identify the centre of the potential well in which the galaxy resides. I create a single datacube for each merger simulation, focussing on the centre of the first galaxy, which is the highest mass galaxy in the case of unequal-mass mergers. This is sufficient for my purposes, as I am predominantly interested in the post-merger remnants.

The basic steps to create a realistic MaNGA datacube are to: (1) apply a seeing (atmospheric) point spread function (PSF); (2) sum the light that falls down each circular fibre in a single pointing; (3) apply a dither pattern to build the Row Stacked Spectrum (RSS) file; (4) combine the RSS into a regularly gridded datacube. I also explored other algorithms for creating datacubes and found that they are inferior to the one described above. One alternative algorithm is to apply the PSF after the cube is built. This method is computationally less expensive by $\sim$20% but does not lead to sufficiently accurate results. Another algorithm is to bin the simulation directly onto a square grid and apply the well characterised combined atmospheric and instrumental PSF after the binning. This process is simpler to be realised but turns out to be more computationally expensive. More details on the comparison of different algorithms can be found in the next section.

In order to measure the spectrum received by a single MaNGA fibre, I must first apply a PSF to account for the blurring of the light as it travels through the atmosphere. I assume a two-component Gaussian profile with parameters taken from the median of SDSS DR7 imaging fields. To include the seeing PSF effect into the SEDmorph code, I first compute a weight function, $W_{\rm PSF}(d)$, that accounts for the shape of the PSF integrated over the fibre area (assuming a MaNGA fibre radius of 1 arcsec). The detailed calculation of $W_{\rm PSF}$ is shown in Figure 3.10. In the upper panel, I show the 2-Gaussian PSF profile in the g band. The colour indicates the surface brightness of the combination of the PSF and a point source with a total flux of 1 $L_{\odot}$. The black circle indicates the circular fibre with a radius of 1 arcsec (assuming the point source has a redshift of 0.04, the median redshift of the MaNGA survey) and the black dot indicates the fibre's centre. By summing up the flux enclosed by the circle, I get total flux that the point

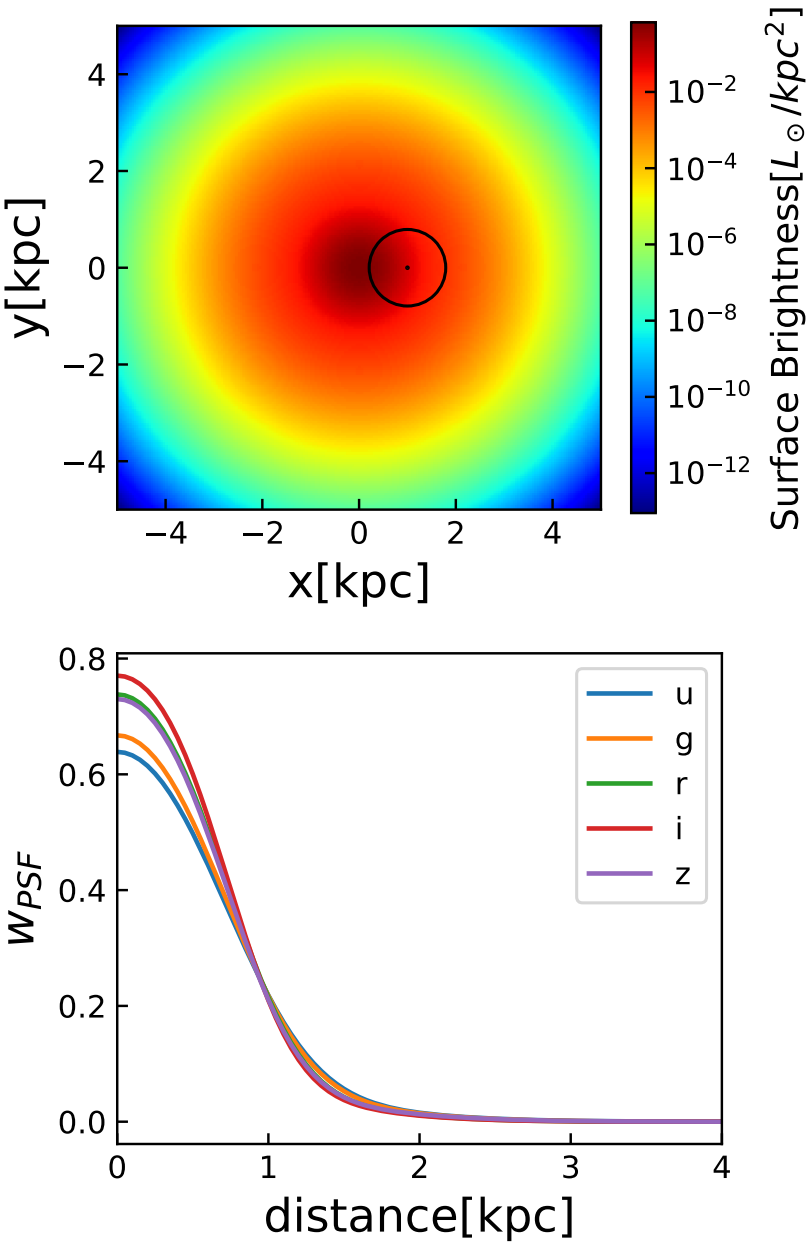

Figure 3.10: The calculation of $W_{\rm PSF}$. *Upper*: The 2-Gaussian PSF profile at g band. The colour indicates the surface brightness of the combination of the PSF and a point source with a total flux of 1 $L_\odot$. The black circle indicates the circular fibre with a radius of 1 arcsec (assuming the point source has a redshift of 0.04) and the black dot indicates the fibre's centre. By summing up the flux enclosed by the circle, I get total flux that the point source contributes to the fibre at a specific distance. *Lower*: PSF weight as a function of distance between the fibre and the point source. This plot is acquired by shifting the fibre in the upper panel to the different distance from the point source and calculating the flux received by the fibre from the point source.

source contributes to the fibre at a specific distance. Since the total flux of point source here is set to be 1 $L_{\odot}$, the total flux got above thus have the same value of $W_{\rm PSF}(d)$. To acquire the $W_{\rm PSF}(d)$ as a function of d, I shift the fibre in the upper panel to the different distance from the point source and calculating the flux received by the fibre from the point source. In order to reduce the computing time I set $W_{\rm PSF}(d) = 0$ once it drops below a value of 10^{-6}. The final weight function at g band is shown in the lower panel Figure 3.10. The PSF weight functions for other bands (u, r, i, z) are also calculated and displayed in the same panel. We find noticeable differences between different bands, thus, different $W_{\rm PSF}(d)$ should be applied for different wavelength ranges. For the purposes of my PhD project I am particularly interested in the spectra of local galaxies around 4000Å, which falls in the g-band for simulated galaxies at $z = 0.04$. Therefore, throughout this thesis, I apply the typical g-band PSF taken from the median values for 500 000 SDSS DR7 fields (specifically, the σ widths of the two Gaussians are 0.54 arcsec and 1.21 arcsec respectively, and the peak amplitude ratio of the two Gaussians is 0.081).

With weight function, $W_{\rm PSF}(d)$, I calculate the integrated spectrum that falls within the jth fibre, $l_{\lambda,j}$, by summing over stellar particles in the simulation accounting for their distance from the centre of the fibre, d, and the shape of the PSF:

$$l_{\lambda,j} = \sum_{i=1}^{N_{star}} W_{\rm PSF}(d)_i l_{\lambda,i} \tag{3.8}$$

where $l_{\lambda,i}$ is the attenuated stellar continuum luminosity density assigned to the ith stellar particle.

The MaNGA fibres are arranged in hexagonal bundles, and sets of three dithered exposures are taken to fill the gaps between the fibres using a triangular pattern with a side length of 1.44 arcsec. In each MaNGA observation, the number of dither sets depends on the time it takes to reach the target depth, leading to an integer multiple of 3 exposures (3,6,9,12, etc). For the mock observation, one dither set of three exposures will be sufficient. To know where to place the circular apertures on the simulated galaxy, I take a representative metrology file for the largest MaNGA IFU bundle of 127 fibres (ma134-56995-2.par[6]) which records the positions of all the fibres in one dither. I then shift the fibre positions following the triangular pattern

[6]An slightly older version that's publically accessible can be found here: `https://svn.sdss.org/public/repo/manga/mangacore/tags/v1_6_2/metrology/ma134/ma134-56995-1.par`. The older version is off by a slight scaling factor from the one used in this project.

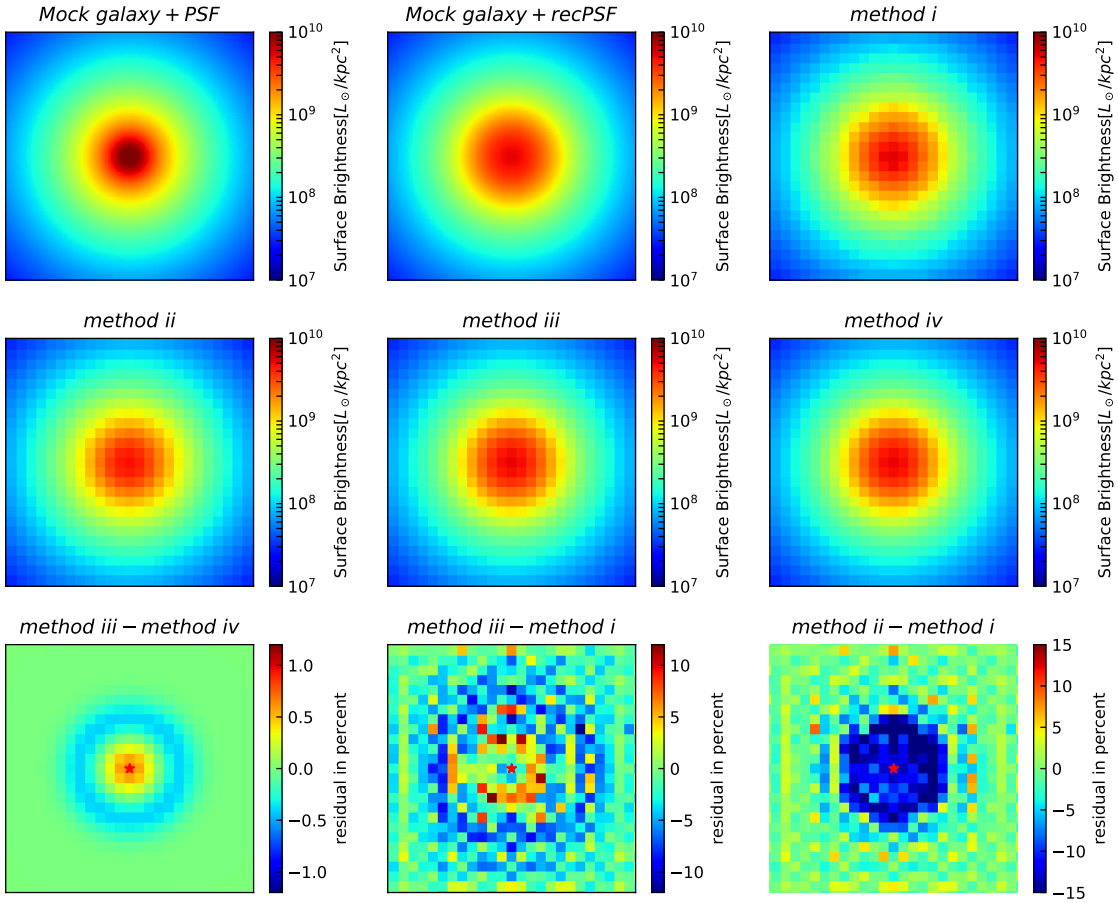

Figure 3.11: Comparison of different datacube creation methods to turn a mock galaxy into a mock IFU observation. The mock galaxy (top left) has a Sérsic light profile with $n = 4$ and effective radius of $R_e = 1.5$ kpc. All the panels here are 10×10 kpc, displaying the mock galaxy up to $\sim 3R_e$. The centre of the galaxies is marked by a red star in the lower panels. The panels are described in detail in the text. The top row shows the mock galaxies with different PSFs as well as the reconstructed image methods that I use in this project. The middle row shows reconstructed images using the alternative methods described in this appendix. The bottom row shows the comparison between these alternative reconstruction methods and the one I used in this project.

for the fibre positions in the other two dithers.

Once I have calculated the spectra in each individual exposure, I combine them into a 3D datacube using the same flux-conserving algorithm as used in the MaNGA survey (see subsection 3.4.2 and Section 9.1 of Law et al., 2016, for details). I do not include noise due to e.g. sky background, therefore I do not calculate error arrays or masks. Neither do I model the line spread function, and the resulting spectra remain at the spectral resolution of the SSPs.

3.5 Comparing different datacube creation methods

I explored several different algorithms for the creation of a mock datacube. Here I justify why it is necessary to run the full procedure that correctly accounts for the seeing and observed dithering pattern. The methods that I am comparing are:

1. use circular fibres, apply the seeing (atmospheric) PSF to the mock galaxy, apply the dither pattern, and subsequently sample the spectra onto a regularly gridded datacube (this is the method described in Section 3.4);

2. as method (i), but only convolve the spectra with the seeing after creation of the regularly gridded datacube;

3. directly sample the galaxy onto a regular square grid, and apply the PSF after creation of the datacube. "Square fibres" are used in this method when creating spectra for different pixels. The PSF for this method consists of the MaNGA reconstructed PSF kernel (*recPSF*), while for the above two methods, the PSF consists of the seeing at the focal plane only.

4. as method (iii), but convolve the spectra with the *recPSF* before creation of the regularly gridded datacube. This method is computationally more demanding than method (iii), but also more realistic.

I first create a mock galaxy with a Sérsic profile light distribution with $n = 4$, effective radius of $R_e = 1.5$ kpc, and intensity at the effective radius of $I_e = 10^9\ L_\odot/\mathrm{kpc}^2$. The mock IFUs cover an area of 10×10 kpc^2, up to $\sim 3R_e$ of the model galaxy. The mock galaxy is shown in the top row of Figure 3.11, convolved with a typical g-band seeing for the SDSS observatory in the top left panel and convolved with the median g-band effective reconstructed PSF (*recPSF*) kernel (Yan et al., 2016) for the MaNGA survey in the top middle panel. Note that the *recPSF* is more extended than the seeing PSF because it is the result of the convolution of the Gaussian seeing kernel with the top-hat fibre response function. My full simulated cube is then reconstructed following method (i), which strictly follows the MaNGA observation strategy. This image is shown in the top right of Figure 3.11. I also reconstruct the image using method (ii) and show the result in the centre-left panel in Figure 3.11. Finally, I reconstruct the image using methods (iii) and (iv), and the resulting images are shown in the centre-middle and centre-right panels,

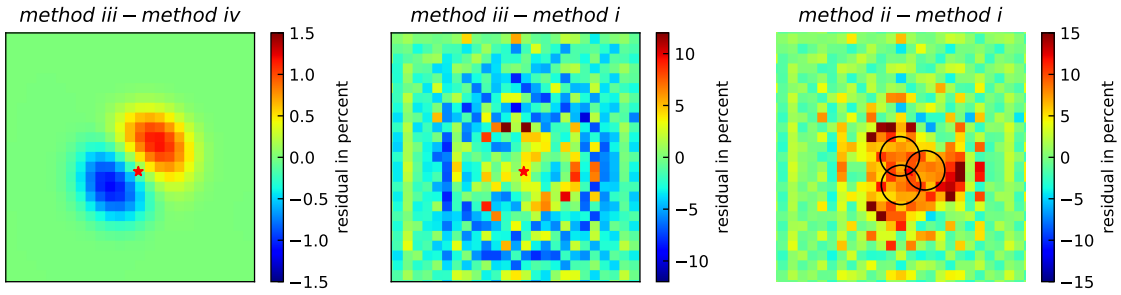

Figure 3.12: Same as the bottom row of Figure 3.11 but the centres of the IFUs are slightly offset from the galaxy centre. In this case, the galaxy centre (red star) falls at the position that is always covered by the circular fibres at all three dithered exposures.

respectively.

In the bottom row of Figure 3.11 I compare the different methods by showing residuals as indicated. The left panel shows a comparison of method (iii) and (iv), and I conclude that these methods only deviate at the few percent level. The central panel compares method (iii) and (i), which again shows that these methods deliver similar results, with residuals mostly below 5 percent. The benefit of applying the seeing first using the RSS method (method i) is demonstrated in the right panel, with residuals between method (i) and (ii) at the level of 10%. The application of the seeing after the RSS cube construction results in a total flux loss of ∼10%, depending on the exact position of the galaxy centre compared to the IFU centre.

In Figure 3.12 I shift the position of the centres of the IFUs slightly relative to the galaxy centre such that the galaxy centre falls in the region covered by all 3 circular fibres in the dithered MaNGA observations. Method (iii) again produces a similar result compared to the standard RSS method (i). With the RSS method, I find a total flux gain of 5% when the seeing is applied after (method ii), rather than before the RSS cube creation (method i).

I exclude method (ii) of applying the seeing after the RSS cube as it does not reproduce the MaNGA observations. Using square fibres (methods iii and iv) seems to be acceptable as most pixels have a difference less than 5%. Though these two methods reproduce proper flux in most pixels, it has been warned that using square fibres gives wrong higher-order data (e.g. the variance, the MaNGA team, private communication at the MaNGA collaboration meeting 2020.) Meanwhile, the square fibre process is more computationally expensive because it needs to create spectra for every pixel. For a 127-fibre IFU, the standard RSS method (i) creates only 381 spectra in total (127 fibre × 3 dithers).The 127-fibre IFU covers a hexagon region with a side width of 12 arcsec. For a pixel size of 0.5 arcsec× 0.5 arcsec as in MaNGA, this

region contains ∼1492 pixels. Therefore, 1492 spectra are required in the square fibre process to reach the same coverage, which is ∼4 times of that in the standard RSS method. Though the square fibre approaches save the dithering and the data-gridding steps and are faster when creating a single spectra, it is still 3 times more computationally expensive compared to the RSS approach used in this project. I therefore settled on method (i) for the datacube reconstruction method used in this project.

Comparison Summary: To create mock MaNGA datacubes, I found it was necessary to strictly follow the MaNGA observation strategy (method i). Short cuts have their drawbacks at the same time. Convolving with the PSF after data gridding (method ii) produces significant residuals. Gridding data directly (methods iii and iv) does produce the right flux but gives wrong higher-order data like variance, it also requires larger computational resources compared to a full treatment.

4

RADIAL GRADIENTS IN POST-STARBURST GALAXIES

Integral field spectroscopic (IFS) surveys have revealed radial gradients in the optical spectral indices of post-starburst galaxies, which can be used to constrain their formation histories. In this chapter, I utilise the binary merger simulations introduced in section 2.1, create post-processed mock IFS datacubes of the simulated galaxies, carefully matched to the properties of the MaNGA IFS survey with the SEDmorph code presented in chapter 3.I then study the spectral indices of the mock datacubes to investigate the origin of the radial gradients in PSBs and constraining their formation mechanism.

4.1 Observational motivation

Chen et al. (2019) identified $>$ 300 galaxies with PSB regions based on traditional cuts on Balmer absorption line and Hα emission line strengths, out of over 4000 galaxies in the MaNGA

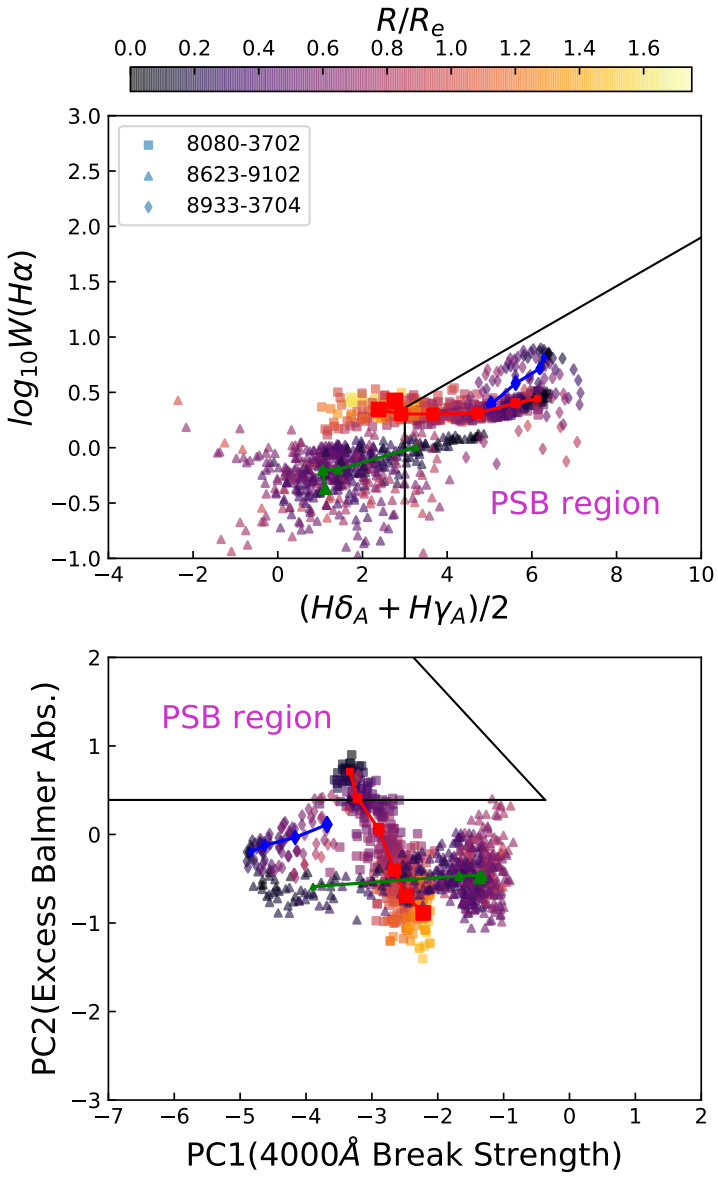

Figure 4.1: Spectral index distributions for three representative MaNGA post-starburst galaxies selected from Chen et al. (2019), with points colour coded by radius with respect to the galaxy's effective radius as given by the upper colour bar. The red, green and blue lines and points show the median values for spaxels binned in annuli of width 0.25 R_e with larger symbols indicating outer regions. The MaNGA plate-ifu identifiers are given in the inset box. *Top:* Hα equivalent width (in Å) vs. the summed stellar continuum indices Hδ_A and Hγ_A. *Bottom:* the principal component spectral indices that characterise the strength of the 4000Å break (PC1) and any excess Balmer absorption over that expected for the normal star-forming main sequence (PC2).

Product Launch 6 (MPL6, see Bundy et al., 2015, for an overview of the MaNGA survey)[1]. Of these, they identified 31 galaxies with centralised PSB signatures (CPSB). For these 31 galaxies, I downloaded the publicly available spectral data cubes and spectral measurement maps from the SDSS Data Release 15 (DR15, Aguado et al., 2019), which were created by the MaNGA Data Reduction (DRP, Law et al., 2016) and Analysis (DAP, Westfall et al., 2019) pipelines. In both cases I used the "HYB10" spaxel binning where the stellar-continuum analysis is performed on Voronoi binned cells with a minimum signal-to-noise ratio (SNR) of 10 (Cappellari & Copin, 2003), while the emission-line and spectral-index measurements are performed on the individual spaxels.

From the DAP maps, I extracted the Hα emission line equivalent width (W(Hα)), H$\delta_{\rm A}$ and H$\gamma_{\rm A}$ stellar continuum absorption line indices (Worthey & Ottaviani, 1997), the mean g-band weighted signal-to-noise ratio per pixel map and stellar velocity map. In all that follows I masked spaxels with spaxel g-band SNR smaller than 10. During the MaNGA data analysis the emission and absorption lines are fit simultaneously, and the emission component is subtracted from the spectrum before the absorption indices are calculated (see Belfiore et al., 2019, for full details). In this way the stellar and gas components of the spectrum are separated and are therefore independent of one another. The W(Hα) measurement is then calculated from a Gaussian fit to the residual emission line spectrum. The H$\delta_{\rm A}$ and H$\gamma_{\rm A}$ absorption line indices are defined as the continuum normalised total flux difference between the absorption feature and a "pseudo-continuum" defined as a straight line between two flanking bandpasses, with the bandpasses as defined in Worthey & Ottaviani (1997). They can therefore be negative in old stellar populations whose spectra exhibit only weak Balmer absorption.

From the summary "DRPall" file I obtained the effective radius, measured as the radius that contains half of the Petrosian flux in r-band elliptical apertures from the NASA-Sloan Atlas catalogue[2], and the Galactic extinction. From the DAP spectral data cubes I obtained the flux and variance, which I corrected for Galactic extinction and shifted to the rest frame using the redshift and stellar velocity maps. I then linearly interpolated the flux and error arrays onto the eigenbasis wavelength array of Wild et al. (2007), in order to measure principal component based spectral indices that describe the shape of the 4000Å break region of the optical stellar continuum spectrum, using a normalised-gappy PCA algorithm to take account

[1] An internal team data release including the first 3 years of MaNGA survey data
[2] `http://nsatlas.org`

of the error arrays and any masked spaxels. Further details on the PCA spectral indices are given in Section 1.2.2.

Following the method of Chen et al. (2019), I mask all spaxels with SNR$<$ 10 and those with "DONOTUSE" flags, and calculate the distance of every spaxel from the centre of the galaxy, as a function of the effective radius. In Figure 4.1 I show the spectral index distribution as a function of distance from the centre for three good quality CPSB galaxies, in both W(Hα) vs. Balmer absorption line strength (top), and PC1 vs. PC2 (bottom). These three galaxies were selected to illustrate the range in radial gradients observed in the full sample. By definition, the central regions of the three galaxies lie within the traditional W(Hα) vs. Balmer absorption line strength selection box, which I define as (Hδ_A+Hγ_A)/2 $>$ 3 and W(Hα) $<$ 2.2$\times$(Hδ_A+Hγ_A)/2 $-$ 0.3. There are strong radial gradients in the Balmer absorption line strength, with the central regions much stronger than the outer regions. In the PCA spectral indices we see a range of radial gradients, from marginally positive to strongly negative. I note that neither 8933-3704 nor 8623-9102 would be identified as a PSB by the PCA spectral indices, within the selection box defined by Rowlands et al. (2018a), which suggests that a very recent and rapid shut down in their star formation has occurred, before the Balmer absorption lines have had a chance to strengthen sufficiently to reach the PCA selection box.

Simple toy models indicate that these observations are consistent with two simple scenarios: a single co-eval burst which was stronger in the central regions, or a starburst that has progressed from outside-in (see Figure 4.2). However, the toy models are unable to distinguish between the two options. These results form the motivation for this chapter: why do we observe radial gradients in the spectral indices of PSB galaxies, and can we use them to tell us something about the physical processes that led to the formation of these unusual galaxies?

4.2 Spectral analysis of mock observations

The observational results above motivate me to run the binary merger simulations to create post-starburst galaxies. The models and simulations have been introduced in section 2.1. I then apply the SEDmorph code (see chapter 3) to create mock spectra and IFU datacubes for the simulated galaxies. The analysis of the mock observations is presented below.

Traditionally, PSBs are identified by strong Balmer lines alongside an absence of nebular emission. However, this method will not select post-starburst galaxies with low-level residual

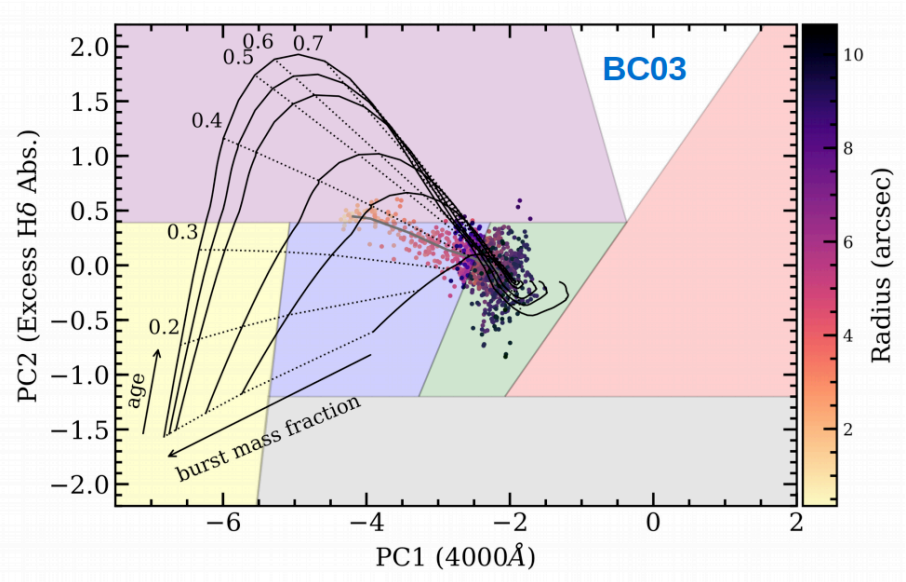

Figure 4.2: Using toy models to explain the origin of the radial gradients in the optical spectral indices of a PSB. Each solid line represents the evolution trace of a model galaxy with a starburst of different burst mass fraction (Burst mass fraction is the ratio of the stellar formed during the starburst to the total stellar mass of the galaxy: $f_{burst} = M_{burst}/M_{tot}$) . The age and f_{burst} trends are marked out by the arrows in the figure. The spectral index distribution of a MaNGA PSB are shown by the points colour coded by radius of the pixel. It can be seen that the observed radial gradient is consistent with two simple scenarios: a single co-eval burst which was stronger in the central regions, or a starburst that has progressed from outside-in. The shaded regions are the selection box for different galaxy populations defined by Rowlands et al. (2018a): quiescent (red), star forming (blue), green valley (green), starburst (yellow), and post-starburst (purple) Figure obtained from John Weaver's MPhy dissertation (2018).

star formation, or those that contain a narrow line AGN (Yan et al., 2006; Wild et al., 2007), and the samples can be contaminated by dust obscured star-forming galaxies (Poggianti & Wu, 2000; Wild et al., 2020). Here, we promote a principal component analysis (PCA) method that use the stellar continuum to provide an estimate of the recent star formation and compare the two methods for identifying PSB regions in our simulated galaxies.

The traditional method

I sum the H$\delta_{\rm A}$ and H$\gamma_{\rm A}$ absorption line indices (Worthey & Ottaviani, 1997) and combine this with the equivalent width of the Hα emission line to investigate when the simulated galaxies obey the "traditional" selection criteria for post-starburst galaxies. I measure the H$\delta_{\rm A}$ and H$\gamma_{\rm A}$ absorption indices using the same method as in the MaNGA survey (see above). I note that these are calculated at the resolution of the MILES-SSPs, ∼58 km/s, which is similar to the MaNGA instrumental dispersion around the 4000 Å break. As I am dealing with small regions of galaxies, the velocity dispersion is not as large as for whole galaxies. Hence, the slight difference in resolution between the simulated spectra and the MaNGA data has little effect on the spectral indices used in this chapter.

In order to calculate the equivalent width of the Hα emission line consistently from the spectral synthesis models, I firstly measure the ionising photon luminosity $Q(H^0)$ from the dust-free continuum luminosity density $l(\lambda)$ (Eqn. 3.2) at wavelengths shorter than the Lyman limit (λ_{ly}):

$$Q(\mathrm{H}^0) = \int^{\lambda_{ly}} l(\lambda)\frac{\lambda}{hc}\mathrm{d}\lambda \tag{4.1}$$

where h is the Planck constant and c is the speed of light. I convert this into an integrated Hα emission line luminosity ($L(H\alpha)$) assuming Case B recombination at $T_e = 10,000K$ (e.g. Kennicutt, 1998):

$$L(\mathrm{H}\alpha)[\mathrm{ergs\ s^{-1}}] = 1.37x10^{-12} \times Q(\mathrm{H}^0)[\mathrm{s^{-1}}]. \tag{4.2}$$

I then attenuate the luminosity due to dust by the same amount as for young stars in the continuum model (Eqn. 3.3). To calculate the equivalent width (EW) of the Hα emission line as used in observations, I extract the mean stellar continuum luminosity density from the attenuated stellar continuum between ±5Å from the wavelength of Hα (l_{6563}). The EW is then given by:

$$W(\mathrm{H}\alpha) = \frac{L(\mathrm{H}\alpha)}{l_{6563}}. \tag{4.3}$$

Principal Component Analysis

I compare the traditional method with a second spectroscopic diagnostic which uses the stellar continuum alone to identify galaxies with stronger Balmer absorption than expected. This method applies a Principal Component Analysis (PCA) to the stellar continuum between 3750 and 4150 Å. More details on the PCA spectral indices can be found in Section 1.2.2. The major advantage of PCA is that the method can detect older and weaker PSBs and those which contain narrow line AGN.

In order to calculate the principal component amplitudes for the spectra in the mock data cubes, I first convert from air to vacuum wavelengths, convolve to the common velocity dispersion of 150 km/s used by the eigenbasis (assuming an intrinsic dispersion of 58 km/s for the MILES library) and then project the spectra onto the same eigenvectors as calculated in Wild et al. (2007)[3]

4.3 Results

In this section I compare the impact of different black hole feedback models, progenitor galaxy properties and orbits on the star formation histories and spectral measurements of the simulated galaxies as a function of time from pre- to post-merger. I then focus in on one particular simulation to study the origin of the radial gradients in the spectral indices.

4.3.1 Comparison between different BH feedback models

In this subsection I compare the quenching progress and observational signatures of quenching in simulations with very different BH feedback models in order to constrain the type of feedback that might be needed to create the post-starburst galaxies observed in the real Universe. Here I consider four models:

1. *No BH*: the BH feedback is turned off;
2. *Thermal BH*: the "classical" thermal BH feedback model (Section 2.1.2);
3. *With RFB*: the mechanical BH feedback model with additional X-ray radiative feedback turned **on** (Section 2.1.3);

[3]The eigenvectors can be downloaded here: `http://www-star.st-and.ac.uk/~vw8/downloads/DR7PCA.html`. Code to perform the projection is available here: `https://github.com/SEDMORPH/VWPCA` (IDL) or `https://github.com/astroweaver/pygappy` (python).

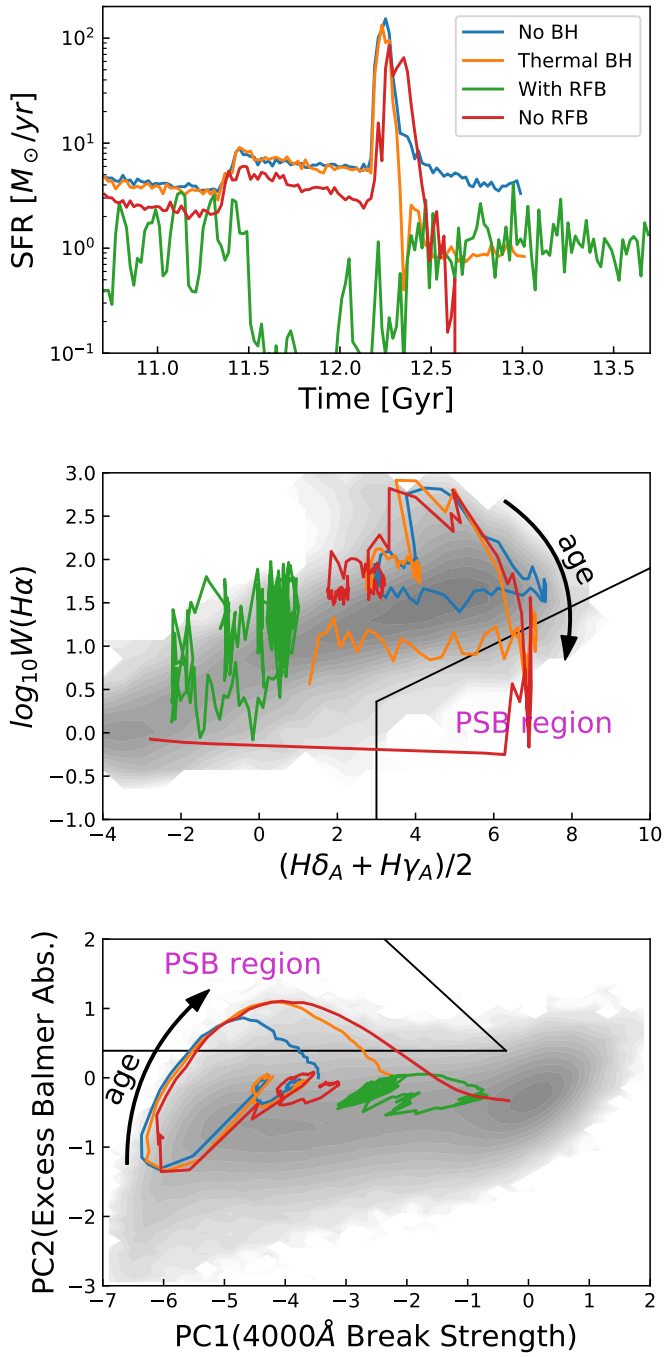

Figure 4.3: Comparison of simulations with the same progenitor galaxies and orbits (2xSc_00), but different BH feedback models. In all panels the different colour lines show a model with: the BH feedback turned off (blue, "*No BH*"); "classical" thermal BH feedback model (orange, "*Thermal BH*"); mechanical BH feedback with additional X-ray radiative feedback (green, "*With RFB*"; mechanical BH feedback without additional X-ray radiative feedback (red, "*No RFB*"). In the *No BH* and *Thermal BH* simulations the model galaxies run out of gas particles before the end of the simulations, thus entering a numerically induced quenching phase. I therefore only show the evolution of these simulations up to that point. *Top*: The star formation histories. *Middle*: The evolution of the simulated galaxies in the Balmer absorption and Hα emission line space. *Bottom*: The evolution of the simulated galaxies in PC space. In the central and lower panels the underlying grey contours show the distribution of the SDSS DR7 galaxies using a log scaled number density and the black lines indicate the commonly used demarcations for identifying clean samples of PSB galaxies.

4. *No RFB*: the mechanical BH feedback model with additional X-ray radiative feedback turned **off**.

I compare simulations with the same progenitor galaxies (2xSc) and orbits (G00); this orbital arrangement produces the strongest torques and therefore cleanest star formation histories making them ideal to compare the impact of the different feedback mechanisms. The star formation histories (SFH) are derived from the change in the total stellar mass of the galaxies between different snapshots (see section 3.1) and the spectral indices are measured as described in Section 4.2.

The results are shown in Figure 4.3. All simulations are run for 3 Gyr, however some simulations experience a very sudden quenching phase caused by a complete exhaustion of cold star-forming gas. In these simulations, the star formation is terminated so quickly that the related quenching is suspected to be not physical. Such extremely fast quenching is at least partly resolution driven. I run the 2xSc_00 merger with exactly the same code and same initial conditions, except for different particle mass resolution. It is confirmed that the quenching would be less drastic at a higher resolution. The related quenching is likely caused by a combination of the employed supernova+BH feedback model and the relatively low particle resolution of the merger simulations. I argue that such "numerical induced quenching" is not astrophysical. To avoid confusion I remove these results from the figures. In all cases apart from the model with both mechanical and radiative feedback (*With RFB*) the SFH is dominated by a strong burst of star formation at coalescence (t ∼12.3 Gyr), which leads to post-starburst features in one or both of the observational index spaces. However, the models differ in the amount that they quench and therefore the final SFR as I will discuss below.

It is clear that the mechanical BH feedback model with radiative feedback turned **on** is too effective at suppressing the star formation. During the first encounter of the galaxies at $t \sim$ 11.5 Gyr some gas is funnelled into the galaxy centre and feeds the BH. The radiative feedback strongly suppresses the star formation below 0.1 $M_{\odot}/yr$, which prevents the small increase in SFR seen in each of the other simulations. Moreover, the radiative feedback completely eliminates the starburst during the final coalescence, preventing the remnant galaxy from showing observational post-starburst features. After the final merger, the galaxy structure becomes relative stable and the gas inflow becomes weaker, which limits the strength of the BH feedback. In observational index space, the galaxy sits predominantly in the “green-valley”

throughout the simulation, temporarily reaching the red sequence after the first encounter. The majority of the gas in the galaxy remains unconsumed by the end of the simulation allowing a relative high final SFR of about 1 $M_{\odot}/yr$, and it quickly returns to the "green valley" following coalescence.

In the other three simulations, the SFHs show a similar trend before the final merger. All the galaxies experience enhanced star formation during the first encounter of the two progenitor galaxies and a strong starburst during the final merger. Note that although the initial SFRs are set to be the same when creating the model galaxies, the SFRs end up with slightly different values when the galaxies reach equilibrium states after the 0.5 Gyr isolated run (see Section 2.1.5). Shortly after coalescence the SFRs decline quickly from the peak, even in the case of no BH feedback. As noted previously in the literature, this initial decline is caused by gas consumption and stellar feedback from O and B-type stars, rather than BH feedback processes. All three galaxies enter the fiducial PSB region in PCA space, due to the spectral signatures of the excess of A/F stars created in the starburst. Following coalescence we see the divergence in the SFH caused by the different BH feedback models. Without BH feedback (*NoBH*) the remnant's SFR remains at a level comparable to that before the merger. Introducing thermal feedback suppresses star formation slightly in comparison, but only to the level of 1 $M_{\odot}/yr$ (i.e. similar to the Milky Way). Only the mechanical BH feedback model *No RFB* is able to completely quench star formation in the galaxy. Due to the residual star formation in the *No BH* and *Thermal BH* models these galaxies retain a level of star formation that leads to significant Hα emission and prevents the galaxy from passing into the traditional PSB selection region. Only the mechanical feedback model is able to suppress the Hα emission sufficiently that the galaxy would be selected as a PSB using the traditional Hα emission vs. Balmer absorption indices. The merger remnant evolves onto the red sequence in both index spaces as the simulation ends.

Based on the discussion above, for the remainder of this chapter I focus on simulations with mechanical BH feedback implemented, but without radiative feedback, as these are the only runs that would be selected using a traditional PSB selection method. I note that the fact that the PCA selection includes objects where the quenching is incomplete may well explain the much larger number of PCA-selected PSBs compared to those selected with the traditional cut on emission line luminosities (Pawlik et al., 2018).

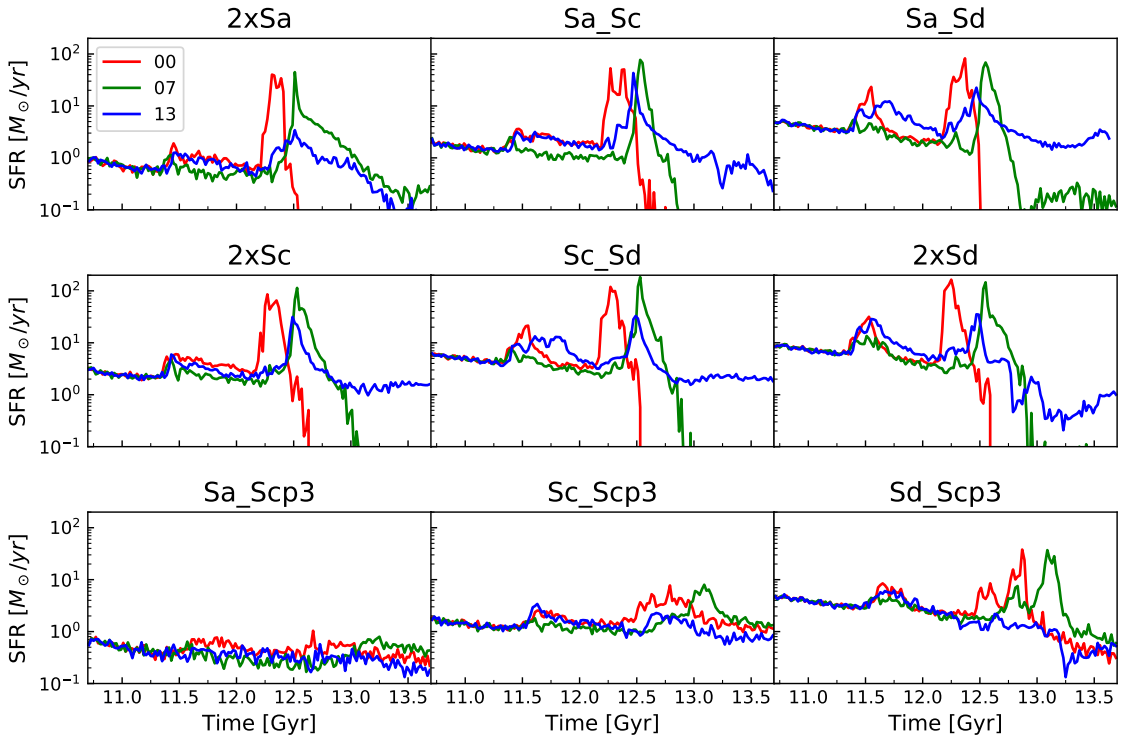

Figure 4.4: SFH of all the merger simulations run with the mechanical BH feedback model and without the additional X-ray radiative feedback. The star formation histories of the merger simulations demonstrate that sharp quenching is only achieved in particular circumstances: progenitor galaxies with similar mass, approaching each other in either prograde-prograde or retrograde-prograde orbits. Neither unequal-mass merger nor retrograde-retrograde merger can reproduce fast quenching.

4.3.2 Comparison between different progenitor galaxies and orbits

I now run the complete set of simulations presented in Table 2.2 with different progenitor galaxies and orbits, using the mechanical BH feedback model. There are 6 combinations of progenitor galaxies for equal-mass merger (2xSa, Sa_Sc, Sa_Sd, 2xSc, Sc_Sd, 2xSd) and 3 combinations for 1:3 mass ratio mergers (Sa_Scp3, Sc_Scp3, Sd_Scp3). Each pair is set on 3 different orbits G00, G07, and G13 (Section 2.1.5 giving 27 different mergers in total. In Figure 4.4 I show the SFH of all 27 simulations. I refrain from showing all evolutionary plots of the spectral indices, as the results can largely be inferred from the SFHs given the knowledge gained in the previous subsection. In this subsection I summarise the results for all 27 simulations, and in the following subsection I focus on one key example showing the full evolution of the model in the observational parameter space.

Almost all equal-mass mergers have strong starbursts. However, despite the strong mechanical BH feedback the starburst can have a long decay time following the merger, especially for the retrograde-retrograde (G13) merger or the retrograde-prograde (G07) merger with

lower gas fractions. In these cases, the SFR displays only a gradual decline, and the Hα EW never declines sufficiently to place the galaxy into the PSB selection box. For unequal-mass mergers, the starburst is significantly weaker compared to the equal-mass merger with the same orbits and progenitors with the same Hubble type. Only the Sd_Scp3_00 and Sd_Scp3_07 mergers enter the PCA PSB region, although with a lower PC2 than the major mergers. Moreover, in all of the nine unequal-mass merger simulations, the post-merger SFR is comparable to the SFR before the merger, leading to strong residual Hα emission. In both equal- and unequal-mass mergers, mergers with Sd galaxies create the strongest starbursts with the same orbit, while mergers with Sa galaxies lead to the weakest starbursts and mergers with Sc galaxies result in intermediate ones. The progenitors do affect the strength of the starburst and, therefore, the creation of PSBs. However, several parameters vary in these progenitor galaxies including bulge fraction and gas fraction. A smaller bulge fraction results stronger starburst in the first close passage but a weaker one in the final merger (Mihos & Hernquist, 1994b). Higher gas fraction provides more fuel for the starburst but very-rich gas-mergers may have lower efficiency at producing starbursts (Fensch et al., 2017). Which factor plays the dominating role in creating a stronger starburst remains unclear and more work could be done to find it out in the future.

The prograde-prograde orbit (G00) is the easiest orbit to reproduce a strong starburst and subsequent quenching. In this orbit, the stellar disc and bulge of the two progenitors collide with each other violently, causing the strongest torques which drive a rapid flow of gas into the galaxy centre forming a large number of new stars in a short time. The gas is quickly consumed, leaving less material for further star formation. The gas flow drives rapid AGN accretion and the resulting BH feedback also reduces the efficiency for the remaining gas to transform into stars. A sharp decline in SFR can be seen in every pair of the equal-mass prograde-prograde progenitors. However, it seems unlikely that this orbital configuration occurs regularly in the real Universe. Comparison with very large cosmological simulations would be required to clarify this.

I conclude that, within the scope of these simulations, sharp and sustained quenching of star formation caused by mergers is only achieved in particular circumstances: relatively gas rich progenitor galaxies with similar mass, approaching each other in either prograde-prograde or retrograde-prograde orbits. In these simulations, neither unequal-mass nor retrograde-retrograde mergers can reproduce features completely consistent with the full range of ob-

served PSB galaxies, with the presence of nebular emission due to ongoing residual star formation being a key constraint.

4.3.3 Evolution of global spectral properties for a representative merger

The previous two subsections have shown that post-starburst features can be reproduced with specific progenitor galaxies and certain orbits, in the presence of significant BH feedback. I now choose one representative merger simulation and focus on its evolving spectral properties. Though the prograde-prograde orbit (G00) produces the strongest starburst and sharpest quenching, such an orbital configuration with both progenitor galaxies having angular momenta parallel to the orbital angular momentum is likely to be rare in the local Universe. I therefore select the next best G07 orbit. Similarly, mergers between two massive disc-dominated galaxies with high gas fractions are unlikely to be common enough to be the most representative cases. I therefore select the Sc progenitors. In this and the following subsections I thus focus on the 2xSc_07 simulation.

The SFH and BH accretion rate of the combined simulation cube are plotted in the top panel of Figure 4.5, with the three coloured vertical lines indicating the different quenching stages. At the blue snapshot ($t = 12.56\,\mathrm{Gyr}$), the SFR starts to decrease (the quenching just begins); at the cyan snapshot ($t = 12.76\,\mathrm{Gyr}$), the SFR drops to a value that is comparable to that before the merger; at the red snapshot ($t = 13\,\mathrm{Gyr}$), the SFR drops below $0.1 M_{\odot}/yr$. The dotted grey line indicates the merger of two BHs at $t = 12.53\,\mathrm{Gyr}$, which is considered as the formation point of the merger remnant.

The central and lower panels of Figure 4.5 show the evolution of the simulated galaxies in spectral index space, integrating the entire spectrum of both galaxies. The simulated galaxy starts from within the blue cloud in both index spaces at the beginning of the simulation, with the first encounter causing a very small change in the spectral indices. During the starburst we observe very strong Hα emission and weak 4000Å break strength (PC1) due to significant contribution to the spectrum from O and B-type stars. The Balmer absorption lines remain strong in starburst galaxies, due to the large number of A and F-type stars formed which are only partially outshone by the O and B stars. However, this translates into a low PC2 as the Balmer absorption line strength is slightly weaker than expected when compared to normal star-forming galaxies. As the star formation declines below its initial level, the remnant quickly moves into the PSB region in both spectral index spaces, ending up on the red sequence. The

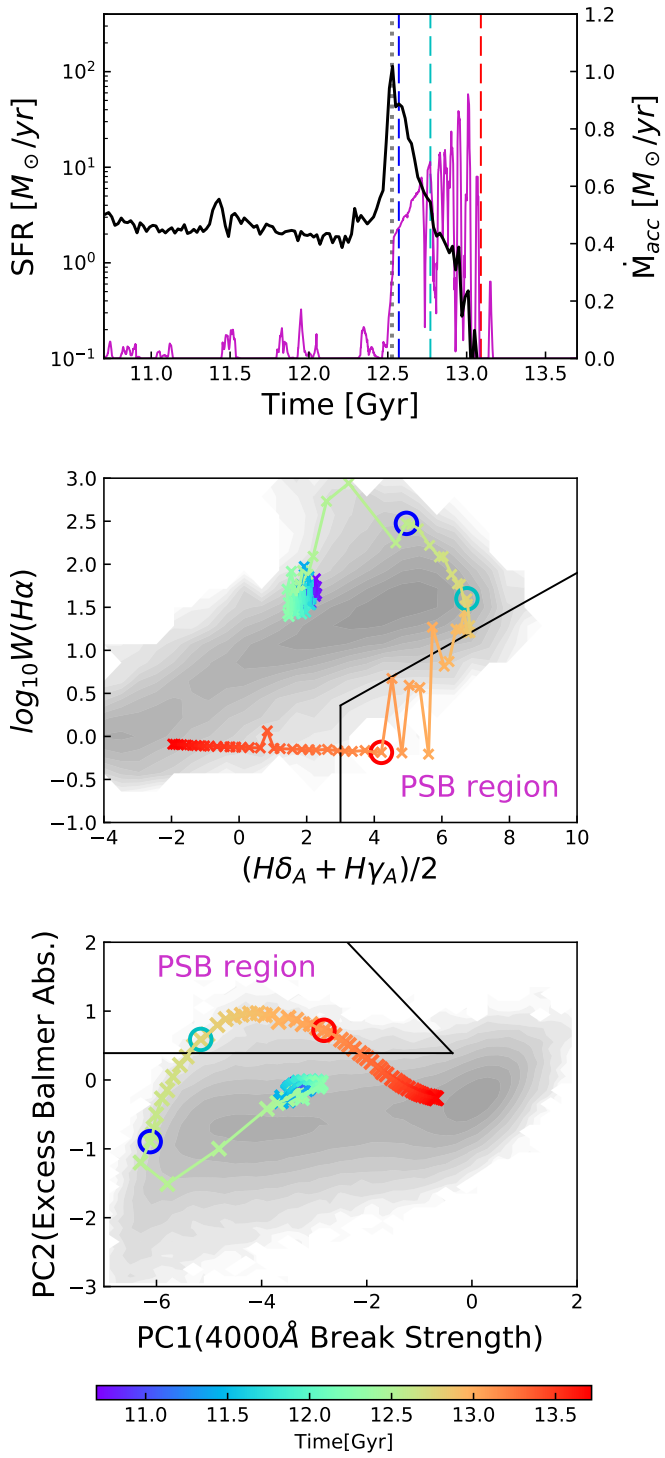

Figure 4.5: The evolution of the global SFH and spectral properties in the 2xSc_07 simulation. The blue, cyan and red dashed vertical lines and circles indicate the snapshots of different quenching stages ($t = 12.56$, 12.76, and 13.08 Gyr respectively). The grey dotted line indicates the time of BH coalescence. *Top:* the star formation history (black) and BH accretion rate (purple). *Centre:* the evolution of the simulated galaxy spectrum in Balmer absorption vs. Hα emission strength. Each cross represents a simulation snapshot spaced every 2×10^7 years, with colour from blue to red indicating the progression of time over 3 Gyr with the colour scale given at the bottom of the figure. *Bottom:* the evolution of the simulated galaxy spectrum in the PCA space.

remnant galaxy can be found in the PCA-defined PSB region consistently from from 12.74 to 13.22 Gyr, while it is found less consistently in the Hα-defined PSB region between 12.92 and 13.16 Gyr.

While the stellar continuum based PCA indices show a stable evolution with time, the Hα emission line strength fluctuates significantly during the PSB phase. The purple line in the top panel of Figure 4.5 shows the smoothed BHAR averaged over 20 Myr, which fluctuates substantially with peaks in BHAR followed by dips in the SFR. I therefore suggest that the fluctuating BH feedback strength causes the galaxy to shift in and out of the Hα-defined PSB region even after entering the PSB phase at $t \sim 12.92$ Gyr.

In general for my simulations, I find that the stellar continuum based PCA selection is a more consistent identifier of PSB galaxies. The very strong fluctuations in the Hα EW will cause an emission line-selected sample to be incomplete, even before the loss of objects from the sample due to narrow line emission from the AGN. However, I note that some observed PSB galaxies selected using the traditional nebular emission based method are not selected with the PCA, in particular the two examples presented in Figure 4.1. I also note that this is not an intrinsic property of the PCA analysis, but caused by not using emission lines in the selection. It would be equally true of any PSB selection method that does not use emission lines. I will return to these points in the discussion section below.

4.3.4 Evolution of radial gradients in spectral properties

To analyse the spatial properties of the PSB remnant in the 2xSc_07 simulation, I create datacubes for the snapshots between $t = 12.56$ Gyr, and $t = 13.08$ Gyr, from the early quenching stage to the late quenching (i.e. the time range between the blue and red lines in the top panel of Figure 4.5). To simplify the analysis I bin the spectra in the mock datacubes according to their distance to the galaxy centre, in annuli of 0–1 kpc, 1–2 kpc, 2–3 kpc, and 3–4 kpc respectively, and calculate the spectral indices from the binned spectra. Taking that the compact remnant has a half-light radius of $R_e = 1.4 \sim 2.0$ kpc during the quenching progress being inspected here, the data here cover a radii $\gtrsim 2R_e$. The evolution in the radial gradients of the spectral indices are plotted in Figure 4.6. As the Hα emission line is very sensitive to the fluctuating residual SFR in the post-merger galaxies, the radial gradient in Hα-H$\delta_{\rm A}$ fluctuates substantially with time during the PSB phase. There is a very strong radial gradient in the Balmer absorption lines at all snapshots, with the central region showing the strongest Balmer

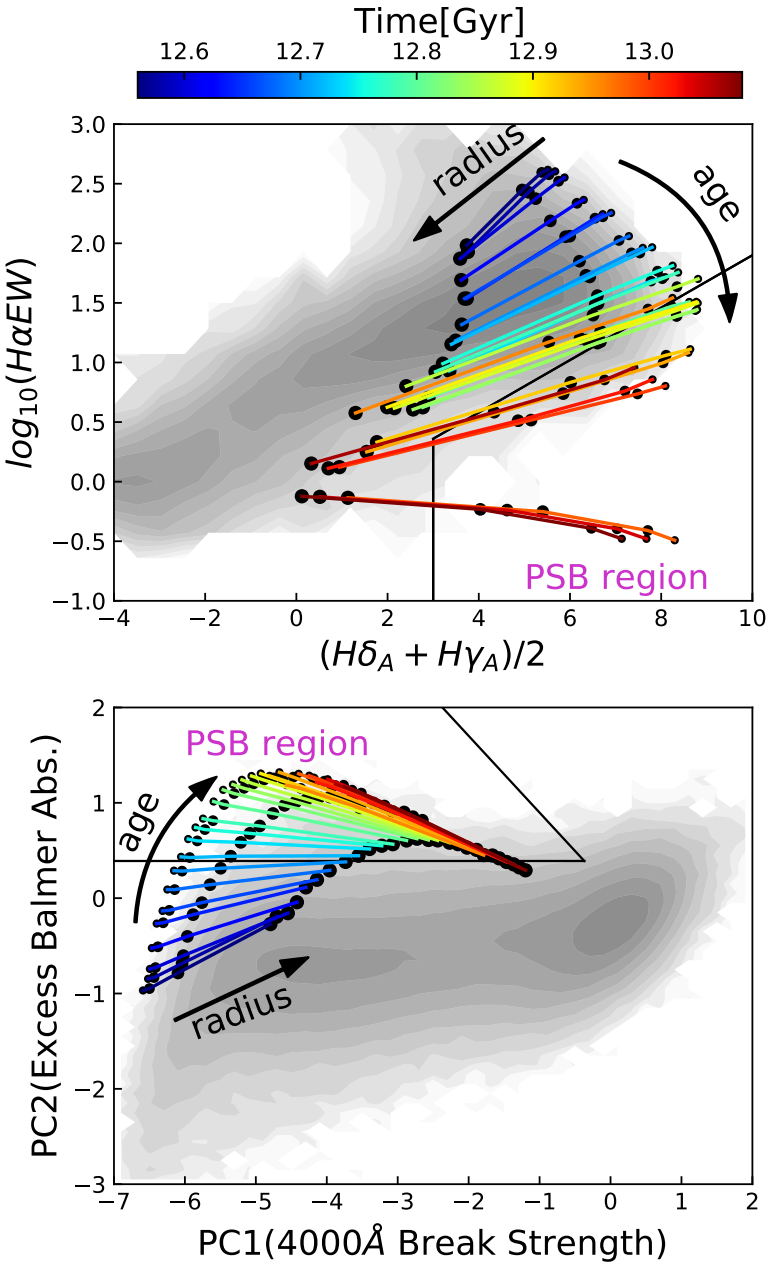

Figure 4.6: The radial gradients in spectral indices for simulation 2xSc_07 between $t = 12.56$ and 13.08 Gyr (i.e. the time range between the blue and red lines in the top panel of Figure 4.5). The spectra are integrated within circular annuli of radius 0–1, 1–2, 2–3, and 3–4 kpc respectively, shown by small to large dots respectively. The colour of the lines indicates the simulation time as given by the colour bar on the top. Note that in the 2xSc_07 simulation, the BHs merge at $t \sim 12.53$ Gyr. *Top:* the evolution of the radial gradient in Hα emission line equivalent width vs. Balmer absorption line strength. *Bottom:* the evolution of the radial gradient in the PCA stellar continuum indices.

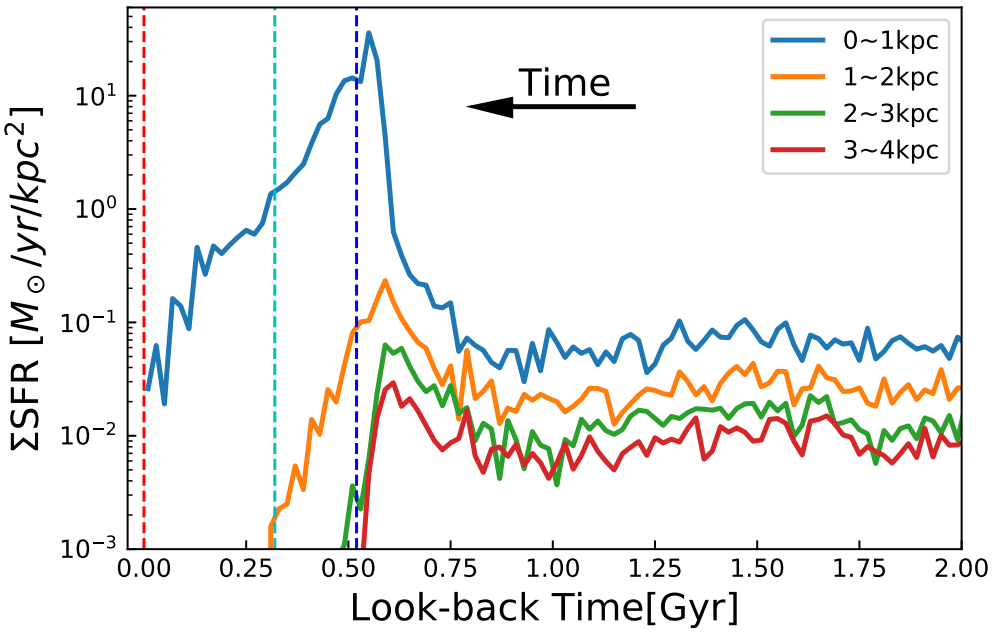

Figure 4.7: The star formation history in different radial annuli of the galaxy, looking back from $t = 13.08$ Gyr, where the SFR decays below $0.1 M_\odot/yr$. The SFRs are scaled by normalised by the surface of each annulus for better comparison.The dashed lines are as in Figure 4.5. The surface star formation rates peak at roughly the same time at all radii but the burst is significantly stronger and more prolonged in the galaxy centre.

absorption lines. In all but a few snapshots, the central region also shows the strongest nebular emission lines. In PCA space the evolution is more stable with time, evolving rapidly from a positive to negative gradient, with the galaxy entering the fiducial selection box at the same time for all radii. In both spectral index figures, only the inner regions of the galaxy are clearly identified as post-starburst, while the outer regions move from star-forming towards quiescent stellar populations.

The ability of the simulation to reproduce the very different radial gradients observed in different PSB galaxies shown in Figure 4.1 suggests that the difference in observed gradients may simply be due to the time at which we observe the galaxy following coalescence. In Section 4.1 I noted that the radial gradients could be produced by a single co-eval burst which was stronger in the central regions, or a starburst that has progressed from outside-in. However, simple toy models are unable to distinguish between these two hypotheses (see Figure 4.2). In Figure 4.7 I show the star formation history of the different radial annuli, taken from the final snapshot shown in Figure 4.6 with $t = 13.08$ Gyr. The star formation rates peak at roughly the same time at all the radii but the burst is both stronger and more prolonged at the galaxy centre i.e. a combination of the co-eval starburst and the outside-in starburst hypothesese. While the

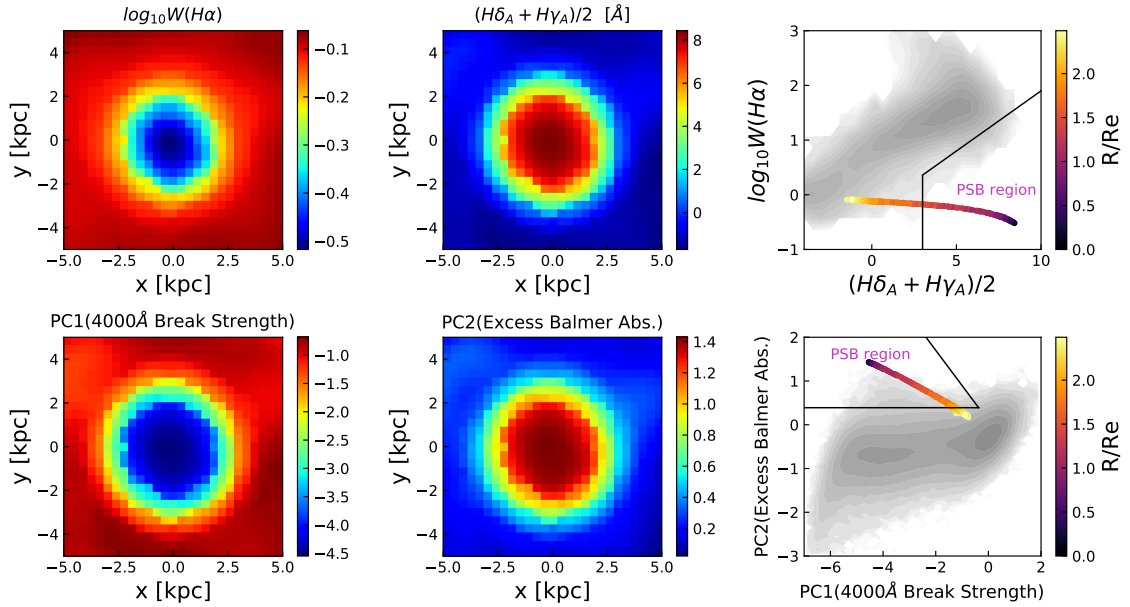

Figure 4.8: Spatially resolved maps of the key spectral indices used in this chapter, for a single snapshot of simulation 2xSc_07 chosen for its strong gradient in PC1/2 and minimal ongoing star formation leading to a flat gradient in W(Hα). On the right I reproduce the radially averaged gradients, colour coded by distance from the centre of the galaxy.

peaks of the star formation are co-eval, the star formation is quenched in the outer regions more quickly than in the inner regions, presumably due to the rapid gas flows continuing to feed the central regions.

4.3.5 Spectral index maps

For completeness, I present the 2D maps of one snapshot of merger 2xSc_07 in Figure 4.8. The snapshot was chosen for the maximal strength of its post-starburst spectral features. We see that the spatial distributions of the spectral indices are entirely smooth, with very little residual structure remaining following the catastrophic event that caused them.

4.4 Discussion

A better model of the physical mechanisms responsible for creating post-starburst galaxies may help to improve our understanding of how and why star formation completely quenches in galaxies throughout cosmic time. Through a careful comparison of real observations from state-of-the-art IFU surveys and mock observations from advanced simulations, we hope to be able to constrain the external and internal processes responsible for quenching star formation.

The galaxy merger simulations presented in this chapter were designed to reproduce low

redshift central post-starburst galaxies, where there is significant evidence that major mergers are the only plausible mechanism for the creation of the strongest spectral features and the high fraction of morphological disturbance. However I have shown that with the galaxy merger simulations presented here it is difficult to create a sharp enough quenching event that leads to both the strong Balmer absorption lines and the complete absence of nebular emission lines due to ongoing star formation. While the strong gas inflow is required to drive the starburst, it is hard to completely shut off the star formation in the centre of the merger remnant without very significant BH feedback, for which there is limited evidence for galaxies in the very local Universe (Fabian, 2012). Whether this is due to the limited size of my simulation set, or limitations in the sub-resolution physics of the models is unclear. Comparison with a full cosmological hydrodynamical simulation would address the former concern, however the latter is much more difficult to tackle: the simulations presented here use very similar recipes to the EAGLE simulation, and most of the currently available simulations do not differ significantly in any of the key ISM or feedback aspects.

One obvious concern is the observed presence of cold gas in a large fraction of PSBs which appears to have very low star formation efficiencies (Rowlands et al., 2015; French et al., 2015; Smercina et al., 2018; Li et al., 2019). For simulations that assume a Kennicutt-Schmidt style star formation law, cold gas forms stars, without any exceptions. In addition, my simulations assume a relatively smooth dust distribution, while it is possible that the observed equivalent width of emission lines is reduced by a highly clumpy dust distribution. Improved recipes for treating the detailed sub-resolution physics of the ISM in these unusual galaxies may thus be required.

My results clearly disagree with the conclusions of Snyder et al. (2011) and Wild et al. (2009): with the improved simulation resolution and sub-resolution physics recipes I find that stellar feedback is only able to cause the initial decline of SFR needed to halt the starburst. Without BH feedback the galaxies return to the blue-cloud or green valley, but cannot further quench the star formation to become entirely quiescent.

This leads me to the question of whether rapid quenching is related to mergers at all. While it is hard to envisage an alternative scenario in the local Universe, the higher gas mass fractions of galaxies at higher redshift may provide the fuel needed for galaxy wide starbursts, without the need for strong centralised inflows which are difficult to halt. Rodríguez Montero et al.

(2019) used the SIMBA cosmological simulations to show that in most cases the quenching of the galaxy was not related to a recent major merger, over a wide range of cosmic time.

A key additional constraint not investigated here is the morphologies of the remnants: highly compact at high redshift (Yano et al., 2016; Almaini et al., 2017) and tidally disturbed at low redshift (e.g. Zabludoff et al., 1996; Yang et al., 2008; Pracy et al., 2009). My simulated post-starburst galaxies are very compact with a super bright core as the results of the highly centralized strong starbursts in the galaxy centre. Such extreme starbursts may be partially the effect of the intermediate resolution and the poor way gas is modelled (a cold, turbulent ISM is not included here) (Teyssier et al., 2010; Powell et al., 2013). However, I would like to argue that my merger simulations are set up with extreme initial condition, it is not surprised that the merger remnants are more compact than active star-forming galaxies with similar masses. As for tidally disturbed features, Pawlik et al. (2018) investigated the morphological asymmetries of mock images created from very similar simulations to those used in this chapter, finding them to decay very rapidly at SDSS-like image depths. Further progress may be possible with deeper imaging datasets, such as will become available in the near future with the Vera C. Rubin Observatory.

With the advent of IFU datasets, the differing radial gradients in the spectral indices of PSB galaxies have become apparent (Pracy et al., 2005; Chen et al., 2019). A negative gradient in the Hδ absorption line strength (i.e. stronger absorption in the centre) as seen in the vast majority of central PSBs (Chen et al., 2019), has commonly been suggested to be an indication of a merger origin due to the gas inflows leading to an excess of A and F stars in the centre. This has been borne out by merger simulations, including those presented here (Bekki et al., 2005; Snyder et al., 2011). Galaxies with PSB spectral features only in their outskirts (so-called 'ring' PSBs) are not produced at all by my suite of simulations, and are more likely caused by external processes which have disrupted the outer disc star formation (Owers et al., 2019a). Interestingly, by decoupling the *excess* Balmer absorption from the past averaged star formation rate, the radial gradients in PCA spectral index space show an intriguing feature, starting out positive, flattening and then becoming increasingly negative with time. This should provide an excellent way to measure the age of PSB galaxies, independent of obtaining precise star formation histories, and suggests that the three different gradients observed in MaNGA galaxies in Section 4.1 could well be caused by the same physical process caught at different observed times.

Throughout this chapter, I have combined the analysis of two very different spectral index spaces: the equivalent widths of the Hα emission line and Balmer absorption lines, and the PCA indices of Wild et al. (2007) which focus on the stellar continuum alone. The sensitivity of the Hα emission line to residual ongoing star formation, which in my simulations fluctuates wildly dependent on the fluctuating BH feedback strength, provides a natural explanation for the much larger number of PCA-selected PSBs than traditional selection (Pawlik et al., 2019). As stated previously, the PCA selection is insensitive to a small amount of residual star formation, which provides an important complementary and more inclusive approach to PSB selection. However, it is evident from Figure 4.1 that the PCA-selection does not identify all observed PSBs, with 2/3 of the example MaNGA PSBs selected using the traditional method falling outside the PCA PSB region. According to their gradients in PC space, these are likely younger objects, where the Balmer absorption has not yet had time to strengthen and 4000Å break strength to increase sufficiently for PCA selection (i.e. the PCA selection box as used in this chapter selects only older PSBs, as noted already previously in Wild et al. (2010)). The two objects with slightly positive or flat gradients in PC1/2 highlight yet another discrepancy with the simulated mergers: the star formation must have been quenched incredibly rapidly for these to be identified as PSBs through their lack of Hα, and such rapid quenching of Hα is never observed in my simulations. This would require an immediate impact of the BH feedback, which as we see from the top panel of Figure 4.5 takes a little while to get going following the coalescence of the BHs. This again suggests an important missing ingredient to the sub-resolution star formation recipes in these simulations.

Finally, I note that the radial gradients in the spectral indices are caused by a stronger, longer duration starburst occurring in the central regions of the galaxy. The starburst in the outer regions happens co-evally with that in the centre, i.e. not supporting either inside-out nor outside-in growth scenarios. The quenching occurs first in the outer regions, however, supporting outside-in quenching for these extreme galaxies.

4.5 Summary

I use Gadget-3 to run a set of binary merger simulations with different black hole feedback models, progenitor galaxies, and orbits. I develop the SEDMorph code to build mock SDSS-like spectra for the simulated galaxy, by combining the star formation history and metallicity of each particle with stellar population synthesis models. I create mock datacubes following the

MaNGA observational strategy including a PSF and dithering pattern. The spatial distribution of Hα emission, Balmer absorption lines, and stellar continuum shape indices are investigated in the post-merger galaxies, to diagnose recent and ongoing star formation.

A summary of my findings is as follow:

- To create mock MaNGA datacubes I found it was necessary to strictly follow the MaNGA observation strategy. Short cuts have drawbacks at the same time. Convolving with the PSF after data gridding produces significant residuals. Gridding data directly does produce the right flux but gives wrong higher-order data like variance, it also requires larger computational resources compared to a full treatment.

- To completely shut down the star formation in the model PSB galaxies, mechanical AGN feedback is required to expel the gas from the galaxy, while the more traditional thermal feedback BH model is not sufficiently efficient.

- The star formation histories of the merger simulations demonstrate that sharp quenching leading to PSB-like remnants is only achieved in particular circumstances: progenitor galaxies with similar mass, approaching each other in either prograde-prograde or retrograde-prograde orbits. Neither unequal-mass mergers nor retrograde-retrograde mergers lead to quenching that is significant or rapid enough to lead to PSB spectral features.

- The traditional PSB selection method, which identifies PSB galaxies via their absence of nebular emission lines as well as strong Balmer absorption lines, is highly sensitive to the complete shut down in star formation, which in turn appears to be sensitive to the accretion rate of the BH shortly before the time of observation. A stellar continuum based method, such as the PCA method used here, is much less sensitive to rapid fluctuations in the SFR of the galaxy and therefore is likely to lead to more complete samples.

- However, two of the three example MaNGA galaxies presented in this chapter are not selected by the PCA method as their Hα emission has shut off before the Balmer absorption lines are strong enough to be identified cleanly by the PCA. Such a rapid shut off in star formation following the starburst is not found in any of my merger simulations. Combined with the fact that many PSBs are known to have cold gas that is not forming stars efficiently, this points to a missing ingredient in the sub-resolution star formation

recipes or the ISM structure employed in these simulations.

- In agreement with previous work, the simulated post-starburst galaxies show a strong radial gradient in the Balmer absorption line strength, with stronger absorption in the inner region, as seen in the majority of local PSB galaxies where the integrated light is dominated by the central PSB region. This appears to be a defining feature of merger-origin PSBs, caused by the inflow of gas to the central regions.

- In PCA space an evolution in the radial gradient becomes apparent, that is masked by traditional methods using nebular emission lines due to their sensitivity to fluctuations in ongoing star formation. This indicates that the range of gradients observed in MaNGA PSB galaxies is simply due to different times of observation rather than different underlying processes.

- My simulations show that the galaxies undergo a single co-eval burst which was stronger and longer lived in the central regions. This does not support either inside-out nor outside-in growth during the star-formation episode, but rather outside-in quenching.

Clearly much more remains to be understood about the formation of PSB galaxies, with this chapter raising questions about the effectiveness of the implementations of BH feedback in the current generation of hydrodynamic simulations. Comparison with cosmological simulations may help us to understand the range of different orbits and gas properties as a function of stellar mass and epoch; however they are still fundamentally limited by resolution as well as the employed sub-resolution star formation and stellar feedback recipes. Observationally, further progress on understanding the causes of both the starburst and final quenching in PSB galaxies may come from combining the analysis of radial gradients in spectral indices with the morphology in deep imaging data, or stellar kinematics from high quality IFU data.

5

RAPIDLY QUENCHED GALAXIES IN SIMBA

A wide range of mechanisms have been put forward to explain the quenching of star formation in galaxies with cosmic time, however the true balance of responsible mechanisms remains unknown. The identification and study of galaxies that have shut down their star formation on different timescales might elucidate which mechanisms dominate at different epochs and masses. In this chapter, I study the population of rapidly quenched galaxies (RQGs) in the SIMBA cosmological hydrodynamic simulation at $0.5 < z < 2$, comparing directly to observational post-starburst galaxies in the UKIDSS Ultra Deep Survey via their colour distributions and mass functions. While the SIMBA simulation has been introduced in section 2.2, I will give the details of the method and the results in this chapter.

5.1 Methods and Analysis

5.1.1 Star formation histories and quenching timescales

With the star formation histories (SFH) of galaxies, it is trivial to measure the timescale over which they quench, and with simulation data this is possible. In this chapter, I identify galaxies to be quiescent if they have an instantaneous specific star formation rate sSFR $< 0.2/t_H(z)$, where $t_H(z)$ is the age of the Universe at redshift z and sSFR is the ratio of instantaneous star formation rate (SFR) to the total stellar mass of the galaxy, sSFR=SFR/M_*. To calculate the SFHs of each galaxy, I use the instantaneous SFR of the galaxy at each snapshot, tracking back through the most massive progenitor. In the case that there are multiple galaxies in the preceding snapshot due to merger events, I choose the most massive one as the progenitor and follow this progenitor back in time. By such a process, I trace backwards the most massive branch of the merger tree of the quiescent galaxies. In some rare cases, I choose to select the longer branch rather than the most massive progenitor branch. This is due to limitations of the halo finder program, when the most massive progenitor has no progenitors, while the second most massive does have. In these cases, I chose the second most massive progenitor to allow me to track back the target galaxies over a longer time range. Fortunately, such cases happen in only about 2% of the sample, so I do not anticipate any impact on my statistical results due to using the longer branches.

Now that I have the full progenitor histories for the galaxies, the specific SFHs (i.e. sSFR vs. time) are formed from the instantaneous gas SFRs of the progenitor at each snapshot, normalised by the total stellar mass of the progenitor, against the cosmic ages of the snapshots. Figure 5.1 shows the derived SFHs for two example galaxies that are quiescent in the $z = 0.5$ snapshot, with the dots showing the instantaneous sSFRs in each snapshot. SIMBA snapshots have a time spacing of ~ 100 Myr in the redshift range of interest in this chapter, which is relatively coarse compared to the timescale over which some galaxies can be quenched. So to improve the accuracy of the estimated quenching timescales, I fit a cubic B-spline (Dierckx, 1975) to the SFH. The interpolated SFHs for the two examples are shown in Figure 5.1 by solid lines. I define the quenching time, τ_q, as the time a galaxy takes to cross from a star-forming threshold to the quiescent threshold defined above, where the star-forming threshold is defined as sSFR$(z) > 1/t_H(z)$. By defining the thresholds with respect to the Hubble time, as suggested by Pacifici et al. (2016), allows for the strong evolution in typical galaxy sSFR

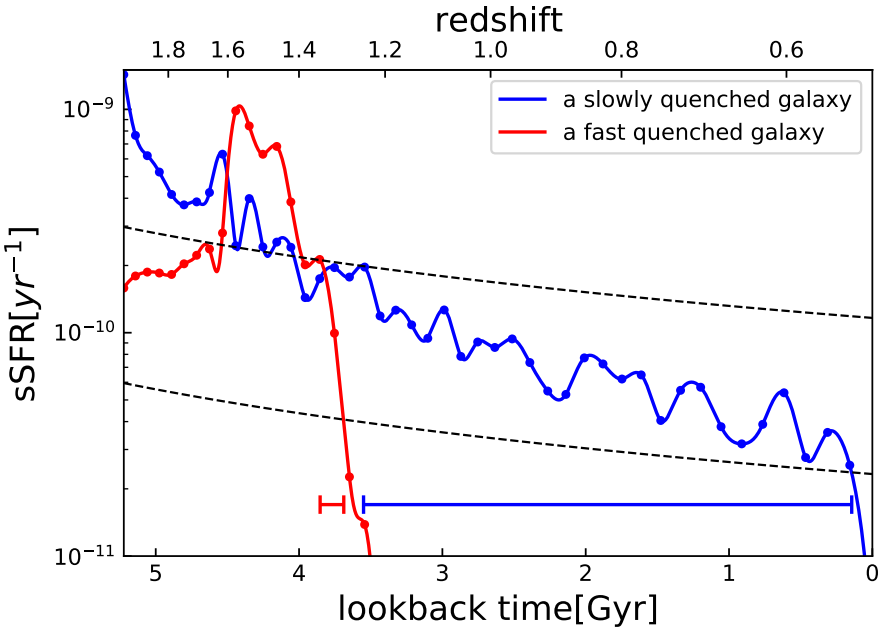

Figure 5.1: Specific star formation histories of an example rapidly quenched galaxy (red dots) and slowly quenched galaxy (blue dots) identified in the $z = 0.5$ simulation snapshot, with lookback time from $z = 0.5$. The dashed lines represent the star-forming (upper) and quenched (lower) thresholds. To better estimate when the galaxies cross the thresholds, I first fit a cubic B-spline (Dierckx, 1975) to the specific star formation history, which are shown as solid lines. I measure the time that a galaxy takes to cross from the star-forming to the quenched threshold and define this to be the quenching time τ_q of the galaxy, indicated by the horizontal bars in the lower portion of the plot.

with redshift (e.g. Speagle et al., 2014). These thresholds are shown by black dashed lines in Figure 5.1, and the inferred τ_q of the example galaxies are indicated by the horizontal bars towards the bottom of the figure. Note that the quenching time τ_q is sometimes scaled by the age of the Universe $t_H(z)$ to give a normalised quenching time of $\tau_q/t_H(z)$. As explained below I do not follow this convention in this chapter.

I note that mergers can affect the sSFR and therefore the measurement of the quenching timescale. In extreme cases, the primary star-forming galaxy merges with a quiescent galaxy with a mass ratio close to 1, the sSFR of the merger remnant will drop by a factor of ~ 2. However, even in these extreme cases, the sSFR need to be further decreased by a factor of more than 2.5 in a short time so that the galaxy can be identified as a rapidly quenched galaxy. Furthermore, mergers with large mass ratios are rare in both the real and the simulated Universe. Though mergers can change the quenching timescale of a few specific galaxies, they will not systematically affect the identification of rapidly quenched galaxies, the ultimate goal of measuring quenching timescale. Therefore, I decided to ignore the effect of mergers on sSFR in this chapter.

An alternative method for calculating the SFHs of galaxies in the simulation is to make use of the ages of the stars in the galaxies at the snapshot of interest. While this is a more direct equivalent of what is done observationally, I choose not to do this for two reasons. Firstly, I am interested in the evolution of the rapidly quenched population through colour space in order to compare to observations made in different redshift intervals, and therefore I need to allow for galaxy mergers. In real observations, the galaxies observed in these redshift intervals will not include the entire stellar population present in the lower redshift descendent galaxies, but rather just the stars of the pre-merged components. Secondly, in order to calculate the evolving galaxy colours and to compare directly with observations, I make use of the relative distribution of stars and gas to calculate the dust attenuation, and this information is not retained via a simple stellar-age distribution. I note that this does not affect the spectral energy distributions of the galaxies used to compute the colours of galaxies in this chapter, as these are computed using the full stellar-age-metallicity information and therefore have a time resolution close to the time-step of the simulation.

5.1.2 Sample selection

There are $\sim$ 39,000 galaxies identified by the halo finder in the $z \sim 1$ snapshot. I select the galaxies that have stellar masses more than $M_* \geq 5 \times 10^9$ $M_\odot$ and a K band apparent magnitude $K < 23$ mag[1]. With an initial mass of gas particles of $1.82 \times 10^7 M_\odot$, this stellar mass cut guarantees that each galaxy contains more than 275 stellar particles so that the effects of numerical fluctuations are limited. The K band cut also helps to reduce numerical effects, but more importantly, it ensures that the galaxies are bright enough to be observed in the comparison observational dataset.

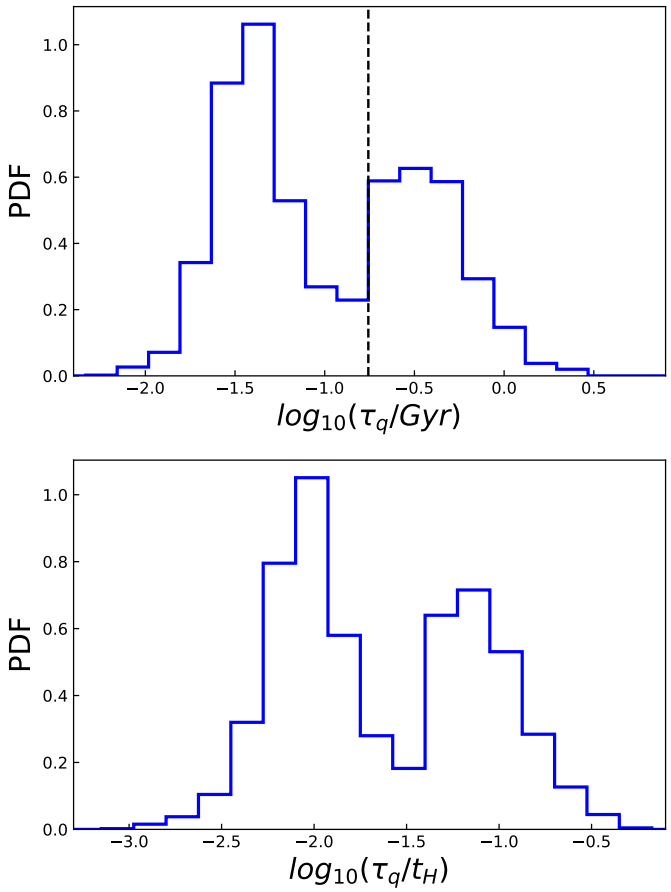

Figure 5.2: The probability density function (PDF) of the quenching timescale (upper panel), and normalised by the age of the Universe at the time that the galaxy is quenched (lower panel) for galaxies that are quenched by $z = 1$ in SIMBA. In both cases the distribution is clearly bimodal, with a division at $\tau_q \sim 175$ Myr (dashed line) or $\tau_q/t_H \sim 0.03$. In this chapter, I am interested in the spectral evolution of the galaxies, therefore the quenching timescale *without* normalisation is the relevant property.

The mass and apparent magnitude cuts select 10,530 galaxies. Of these, 2623 lie below the

[1]It can dramatically reduce the sample size to apply the stellar mass and K band magnitude constraint while tracking the progenitors. Hence, these two constraints are applied to the galaxies at $z \sim 1$ only, and not to their progenitor galaxies.

quiescent threshold (sSFR $< 0.2/t_H$) and form the red sequence at redshift $z \sim 1$. As described above, I track back the progenitors of each galaxy in this final sample, reconstruct their SFH and measure their quenching timescales. The upper panel of Figure 5.2 shows the stark bimodality in the distribution of the quenching timescales very clearly, with a division at $\tau_q \sim 175$ Myr (the dashed line in the figure). For slowly quenched galaxies, their quenching timescale can be comparable to the cosmic timescale, hence it is common to normalise the times by the age of the Universe at the time that the galaxy is quenched ($log(\tau_q/t_H)$, lower panel of Figure 5.2). The bimodality remains with a division at $log(\tau_q/t_H) = -1.5$. While this normalisation is common in the literature (see e.g. RM19 where the bimodality was discovered in SIMBA), it is unrelated to the spectral evolution of the galaxies, which evolve the same regardless of Cosmic age. Thus in this chapter, I adopt the criterion *without* Universe age scaling and define "rapidly quenched galaxies" (RQGs) as those with $\tau_q \leq 175$ Myr.

5.1.3 Mock photometric dataset

Constraining the SFH of a galaxy with observational data is challenging, with limited information stored in the integrated spectral energy distributions (SEDs), and strong dependencies on the fitting methods and stellar synthesis models. Therefore, to compare with real data, I use the PYLOSER[2] package to forward-model the observed colours and create mock photometric data for the simulated galaxies in SIMBA. This uses the stellar population synthesis models pyFSPS, a python version of FSPS (Conroy et al., 2009; Conroy & Gunn, 2010), which combines the MIST stellar isochrone model (Dotter, 2016; Choi et al., 2016; Paxton et al., 2011, 2013, 2015) with the MILES spectral library (Sánchez-Blázquez et al., 2006; Falcón-Barroso et al., 2011). Throughout my analysis a Chabrier initial mass function (Chabrier, 2003) is assumed and nebular emission is included. The models are interpolated to the age and metallicity of each stellar particle.

Wavelength dependent dust extinction is included by ray-tracing the line-of-sight extinction. PYLOSER calculates the dust extinction to each stellar particle within the galaxies based on the density of the line-of-sight dust column, combined with a composite dust extinction law. For galaxies with an average metallicity lower than tenth Solar metallicity, the extinction law of the Small Magellanic Cloud is applied. For galaxies with a metallicity higher than Solar metallicity, a mixed extinction law is used depending on the sSFR of the galaxies: Milky-Way

[2] `https://pyloser.readthedocs.io/en/latest/`

extinction (Cardelli et al., 1989) for less star-forming galaxies (sSFR $< 0.1\text{Gyr}^{-1}$), Calzetti et al. (2000) for highly star-forming galaxies (sSFR $> 1\text{Gyr}^{-1}$) and a linear combination of the two for galaxies with a sSFR in between. For galaxies with an intermediate metallicity that do not fall in the two groups mentioned above, the SMC and "mixed" extinction law are themselves mixed. For the sake of speed, PYLOSER does not employ a much more expensive radiative transfer, however, the results are similar.

The spectra of all stars in the galaxies are summed to form the integrated galaxy spectrum, which is then redshifted and dimmed according to the redshift of the galaxies to simulate observed spectra. Filter transmission functions are finally applied to calculate the apparent magnitude of the galaxies in different bands. Here I compute photometry in 10 filters to mimic the comparison observational dataset: the Subaru B, V, R, i', z'; UKIRT J, H, K; VISTA Y; and IRAC 3.6 and 4.5μm bands.

5.1.4 Super-colour analysis

As well as identifying rapidly quenched galaxies directly from their star formation histories, I use a second method that is directly comparable with observations, which is based on the super-colour method. The details of super-colours have been provided in subsection 1.2.2, here I recap the key features. The super-colour analysis involves projecting the multi-wavelength photometry onto pre-computed eigenvectors (or equivalently eigenspectra) that were determined from a large library of 44,000 model SEDs. The principal component amplitudes indicate the contribution of each eigenspectrum in the SED and are termed "super-colours" (SC). Each super-colour indicates a particular property of the galaxy SEDs: SC1 describes the red-blue slope of the SED, indicating the average sSFR; SC2 changes the strength of the 4000 Å or Balmer break, indicating the fraction of stellar mass formed in the last ~ 1 Gyr as well as the metallicity of star-forming galaxies; SC3 also controls the exact SED shape around the 4000 Å break and helps to break the degeneracy between metallicity and burst fraction.

Similarly to traditional rest-frame UVJ analyses, the super-colour analysis can be used to classify galaxy SEDs into quiescent and star-forming, but without requiring model fits to determine rest-frame colours. Importantly for this project, the super-colours cleanly separate out an unusual class of rapidly quenched, recent starburst galaxies (commonly called "post-starburst" galaxies), which lie above the main populations due to their excess population of A and F-type stars which have unusually strong Balmer breaks while still being quite blue (Wild

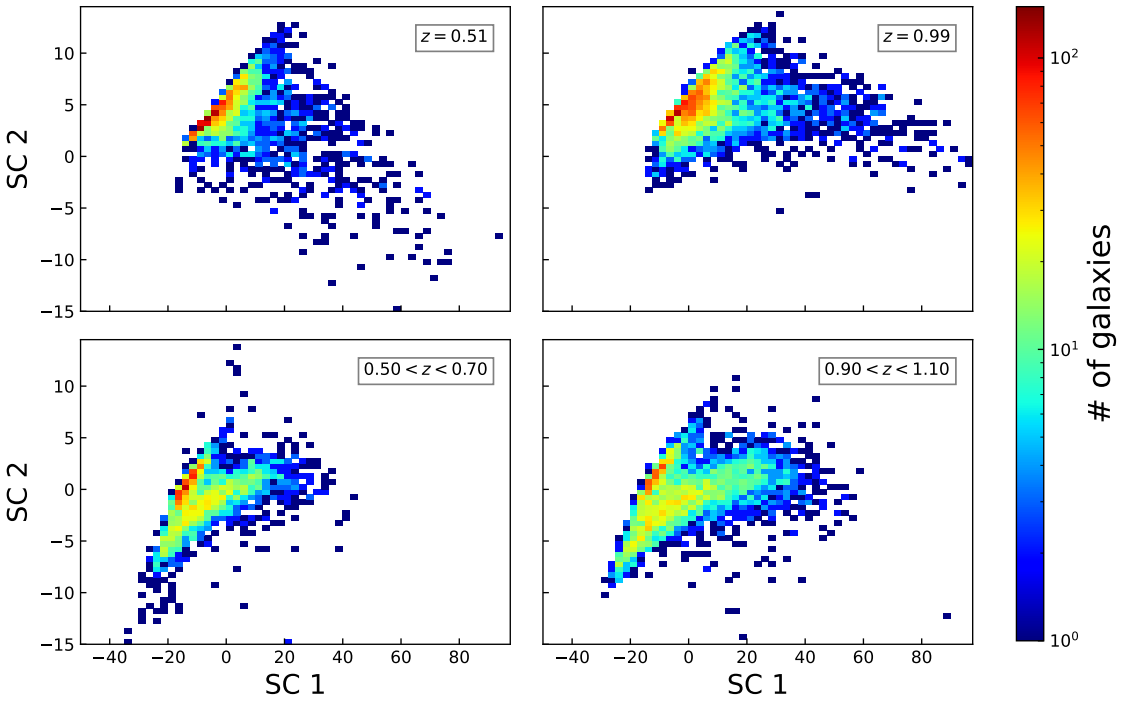

Figure 5.3: The distribution of the first two super-colours, which describe the SED shapes, of SIMBA galaxies (upper panels) and galaxies in the UKIDSS Ultra Deep Survey (lower panels). All galaxies are selected to have K-band magnitudes brighter than $23\,mag$ and stellar masses $M_* \geq 5 \times 10^9 M_\odot$. The SIMBA galaxies are selected from the $z = 0.5$ (left) and $z = 0.99$ (right) snapshots, while the UDS galaxies have a redshift range of $0.5 < z < 0.7$ (left) and $0.9 < z < 1.1$ (right). In order to better compare with the observations, only a randomly selected 40% and 20% of the available SIMBA galaxies are plotted.

et al., 2016; Maltby et al., 2018; Wild et al., 2020). For the purpose of identifying these rapidly quenching galaxies, I find that SC1 and SC2 are sufficient so I focus on these two SCs in the main body of the chapter and only briefly discuss SC3 in the end of this subsection.

The eigensystem of the super-colour analysis is computed with BC03 models, while the photometry of the SIMBA simulated galaxies are computed with the FSPS model. This is not relevant, as the super-colour amplitudes can be calculated for any spectral energy distribution, regardless as to the origin. Note that SCA does not fit for the redshift of the galaxies, instead it takes the redshift as an input. Wild et al. (2014) has confirmed the effect of reasonable photometric redshift errors has negligible effect on the observed super-colours. Hence, I directly use the redshift of the snapshot in when carrying SCA rather than fitting the redshift from my 10 bands data with other algorithms. The upper panels of Figure 5.3 show the super-colour distributions of a subset of the SIMBA galaxies at $z = 0.5$ and $z = 1$, selecting only a random subset of 40% and 20% of the available galaxies in order to approximately match the number of galaxies in the observational comparison samples. In the bottom panels, I display

the observed distribution of super-colours for galaxies (Wild et al., 2016) from Data Release 8 (DR8) of the United Kingdom Infrared Telescope (UKIRT) Ultra Deep Survey (UDS, Lawrence et al., 2007, Almaini et al. *in prep*), with the same mass and K-band magnitude cut, but with slightly looser redshift ranges of $0.5 < z < 0.7$ and $0.9 < z < 1.1$. In the observational data, we can observe a tight sequence to the upper-left of super-colour space, which is comprised of quiescent galaxies with low sSFR (Wild et al., 2014). The lower branch contains star-forming galaxies spread out to cover a much larger region in SC1-SC2 space, with higher sSFR galaxies on the right and dustier or low sSFR galaxies on the left. The post-starburst galaxies lie to the upper-right end of the red sequence, forming a tight sequence and clearly separated from the star-forming cloud, unlike in traditional UVJ colour-colour diagrams.

Comparing between the SIMBA and UDS samples in the upper and lower panels, we see some very clear differences, indicating that the shapes of the modelled SEDs are not entirely correct in SIMBA. The SIMBA galaxies are shifted to higher SC1 and SC2 values compared to the UDS, i.e. the modelled SEDs are on average too blue and have too strong Balmer and 4000Å break strengths. There is also no clean separation between the quiescent and blue sequence, and the post-starburst population is much less clearly defined.

The discrepancies between the distribution of SIMBA and UDS galaxies in super-colour space are *not* due to the spacing of the snapshots in SIMBA, as the photometry is computed from the full stellar age-metallicity distribution in each galaxy, combined with line-of-sight dust extinction. Dust is suspected to play a role here. Star-forming galaxies have more dust than quiescent galaxies, which leads to stronger flux attenuation particularly in the blue, which can impact the measured super-colours. In Figure 5.4 I show the distribution of the first two super-colours with and without dust attenuation in the left and central panels. The blue sequence is well separated from the quiescent population when dust attenuation is excluded. It seems plausible that an inaccurate dust treatment could be the cause for moving the blue sequence too far to the red to blend with the quiescent population. Another suspected cause of the discrepancies is the stellar population model used when creating the mock photometric data for SIMBA galaxies. Thus, I recreate the mock photometric data for SIMBA galaxies with another stellar population model, the BC03 model (Bruzual & Charlot, 2003), following the same method described section 3.1. The differences between SIMBA and UDS results remain as shown in Figure 5.4

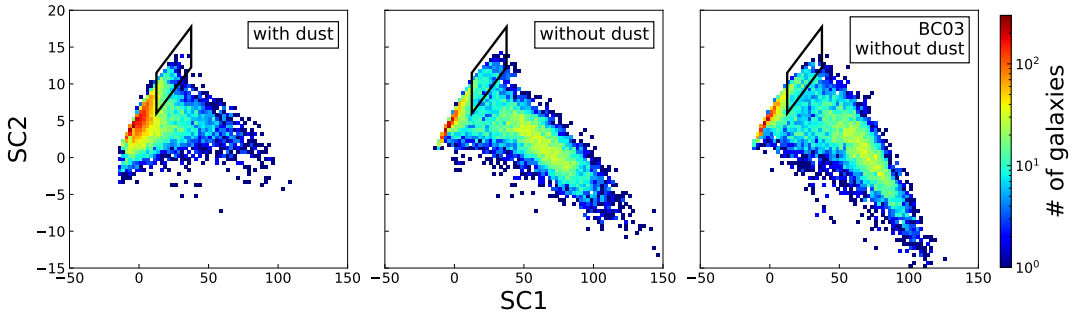

Figure 5.4: The distribution of SIMBA galaxies at redshift $z = 1$ in SC1-SC2 space, the RQG selection box is plotted for reference. *Left panel*: Super-colours computed *including* the line-of-sight dust extinction; *Middle panel*: Super-colours computed **without** dust extinction; *Right panel*: Super-colours computed with the BC03 model (Bruzual & Charlot, 2003) and **without** dust extinction.

From these investigations I conclude that an inaccurate dust treatment may be causing the blue sequence to blend with the quiescent population, but the remaining differences between SIMBA and UDS hint that SIMBA is not perfect in terms of creating the right types of star formation and chemical evolution histories, and I return to this below. Nevertheless, as I show conclusively below, it is still possible to use the super-colours to identify rapidly quenching galaxies, albeit with a level of contamination from star-forming galaxies that I do not expect to see in real samples.

About SC3

Both the second and third super-colours (SC2 and SC3) control the exact SED shape around the 4000 Å break, they correlate with metallicity and give additional information on stellar ages and dust. Thus, SC3 can help break the degeneracy between metallicity, age and dust in some cases. In Figure 5.5, I display the distribution of the SC1-SC3 of SIMBA galaxies (upper panels) and galaxies in the UDS (lower panels). The distribution of SIMBA galaxies show a bar structure in the SC1-SC3 space, which is clearer at $z = 0.99$ (the upper right panel). I confirmed that almost all quiescent galaxies fall on this bar structure while the star-forming galaxies occupy a larger region and form the cloud. In contrast, the UDS galaxies do not show a clear bar. Taking the high measurement error on SC3 in the observation, it is inappropriate to conclude that such a discrepancy does exist in physical level or that SIMBA reproduced a fraudulent structure in SC1-SC3 space. Further investigation with only those observations where spectroscopic redshifts are available might be worthwhile to find out whether SC3 could be useful in the future.

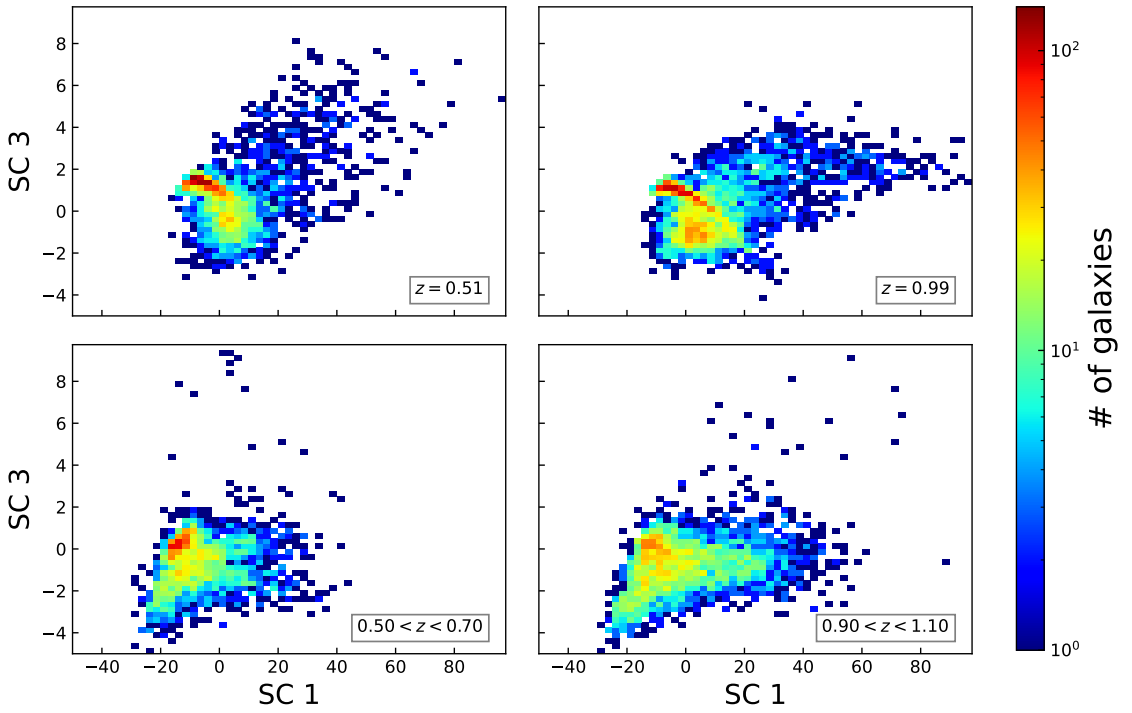

Figure 5.5: Same as Figure 5.3 but for the distribution in SC1-SC3 space.

5.2 Results

In this section I study the effectiveness of the super-colour technique at identifying rapidly quenched galaxies, measure the contribution of the rapid quenching pathway to the build up of the quiescent population as a function of both mass and redshift, and compare the mass function with observations of galaxies selected using the same super-colour technique. Finally, I investigate the visibility timescales of the rapidly quenched galaxies and the impact of an absence of starbursts on the SIMBA galaxy colour distribution.

5.2.1 Rapidly quenched galaxies in super-colour space

The upper panel of Figure 5.6 shows the distribution in SC1-SC2 super-colour space of the 2623 quiescent galaxies with instantaneous sSFR below the quiescent threshold of sSFR$<0.2/t_H(z=1)$ in the $z=1$ snapshot (subsection 5.1.2). As expected from the observational data, the quiescent population follows a tight sequence towards the left-hand edge of the full SC distribution, this is due to the strong 4000Å break strength, with the slope in SC1-SC2 caused by the distribution of both ages and metallicities in the population. The lower panel shows the ratio of rapidly quenched galaxies ($\tau_q \leq$175 Myr) to all quiescent galaxies in super-colour space. We see that almost all quiescent galaxies in the upper right tip of this

sequence have been rapidly quenched, matching the region identified as being dominated by post-starburst galaxies in observations (Wild et al., 2014). I delineate the region with a box as shown to further investigate the properties of galaxies in this region of super-colour space.

In the upper panel of Figure 5.7 I plot the past and future sSFH of *all* 729 galaxies that are found within the box in the $z = 1$ snapshot (i.e. including galaxies that are not yet quiescent, unlike in Figure 5.6). I find that only 10% of them are formally quenched by my definition (i.e. have dropped below the quiescent threshold of sSFR$< 0.2/t_H$), however the galaxies have experienced a rapid drop in sSFR in the recent < 0.5 Gyr, as expected given their strong Balmer break strengths. The median, 16th and 84th percentiles also show a dramatic decrease of sSFR. This highlights an important point about the identification of RQGs: the spectral features are transient, and therefore they are only identifiable for a short time following quenching (see subsection 5.2.3). In the lower panel I show the fraction of these galaxies with sSFR above the star-forming line, below the quenched line, and in between, as a function of time from $z = 1$. Despite most having experienced a recent sharp decline in star formation, they do not immediately cross the threshold to become fully quenched, with only ∼60% of the galaxies formally quiescent within 1 Gyr. I note that this is unlikely to be representative of the situation in the real Universe, where the RQGs form a distinctly different population to the star-forming galaxies, while in SIMBA the blue sequence appears to merge into the RQG area of super-colour space.

5.2.2 Contribution of rapid quenching to the quiescent population

With the simulation dataset, there are two ways to identify quiescent galaxies that have previously rapidly quenched their star formation and thus assess the contribution of rapid quenching to the build up of the quiescent population. Firstly, I can identify them by their known SFHs (SFH-selected), and secondly by their observational signatures (SC-selected). Note that I do not use the super-colours alone to identify RQGs in SIMBA as is done observationally, but first identify quiescent galaxies and track back their evolution in super-colour space to see whether they enter the region where we find a high fraction of RQGs in Figure 5.6. In this section I compare both methods to measure the contribution of the rapid quenching route to the quiescent population in SIMBA, as well as how well photometric observations are able to recover the true impact of rapid quenching.

In Figure 5.8, I display the super-colour traces of the progenitors of the two example $z =$

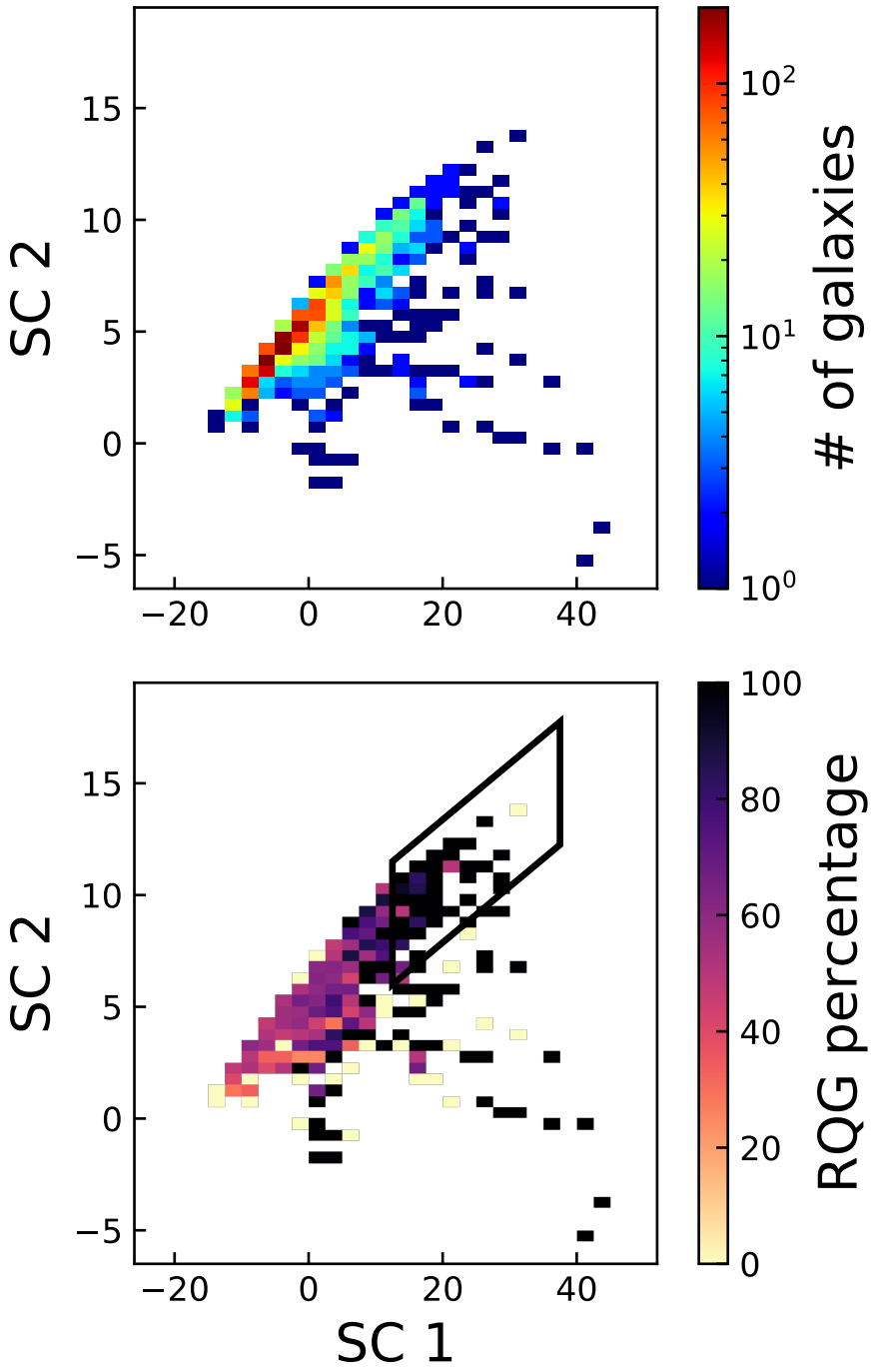

Figure 5.6: *Top:* The distribution in super-colour space of quiescent galaxies in the $z = 1$ snapshot of the SIMBA simulation, selected to have an instantaneous sSFR$< 0.2/t_H(z = 1)$. As found in observed data, they form a tight sequence to the left of super-colour space. *Bottom:* The ratio of the number of rapidly quenched galaxies to all quenched galaxies. Almost all quiescent galaxies found in the upper right tip of the red sequence have been rapidly quenched. I mark this region with a box to further investigate the properties of the galaxies in this region.

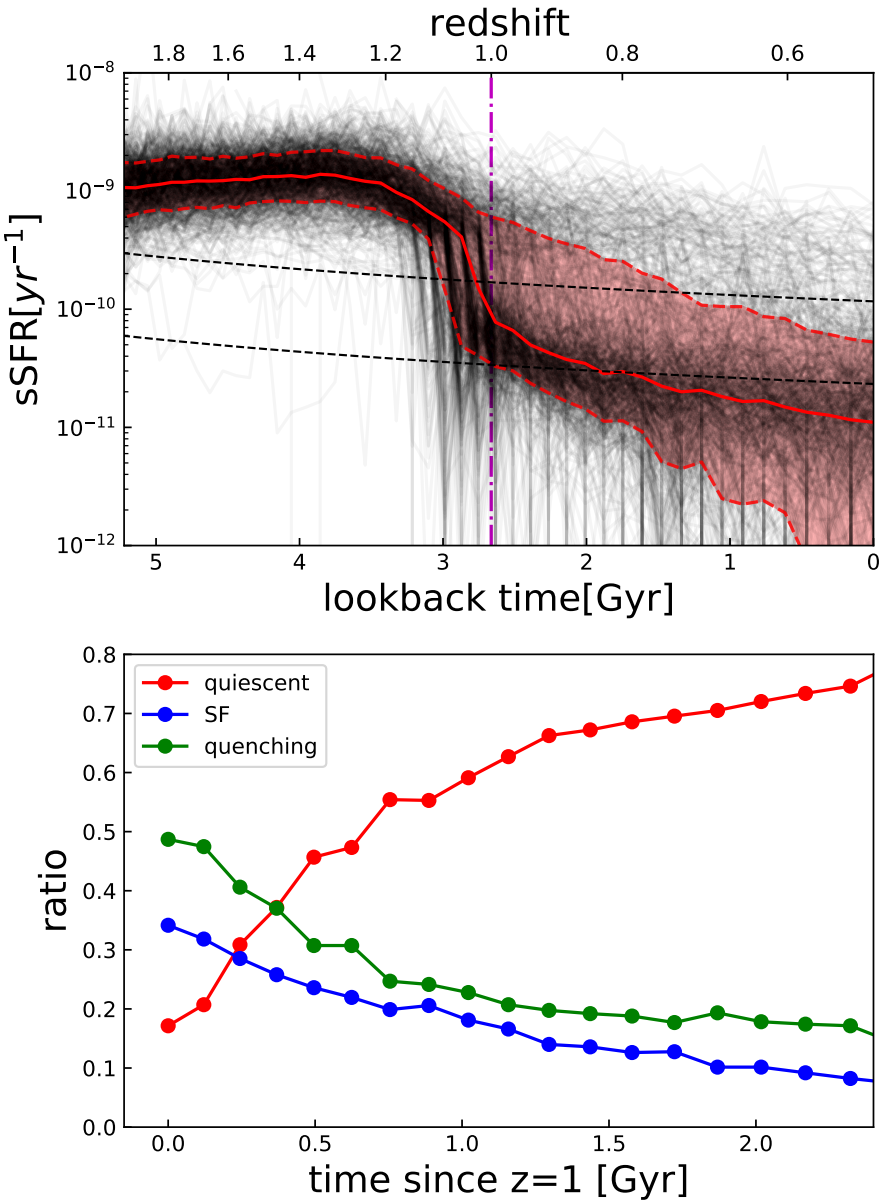

Figure 5.7: Investigating the past and future star-formation properties of galaxies that fall inside the box delineated in Figure 5.6 in the $z = 1$ snapshot of the SIMBA simulation. *Upper panel*: the sSFH of all galaxies that fall inside the super-colour defined RQG box in the $z = 1$ snapshot (black lines), with the 16th, 50th and 84th percentiles of the sSFR at each lookback time since $z = 0.5$ (red lines). The dashed black lines show the evolving star-forming and quiescent thresholds. The magenta line marks the time at $z = 1$. Although only $\sim 10\%$ of the galaxies in this region of SC space are currently quiescent, the majority show a recent sharp drop in their SFHs which drives their unusual SED shapes and position in super-colour space. *Lower panel*: The census and future evolution of galaxies that fall in the super-colour defined RQG box at $z = 1$. The majority of galaxies in the box are "quenching", i.e. they have a sSFR between the star-forming and quiescent thresholds. Despite their recent rapid quenching events, many remain above the quenched threshold for a significant time period, with only $\sim$60% of the galaxies in the box at $z = 1$ becoming formally quiescent in the following 1.0 Gyr.

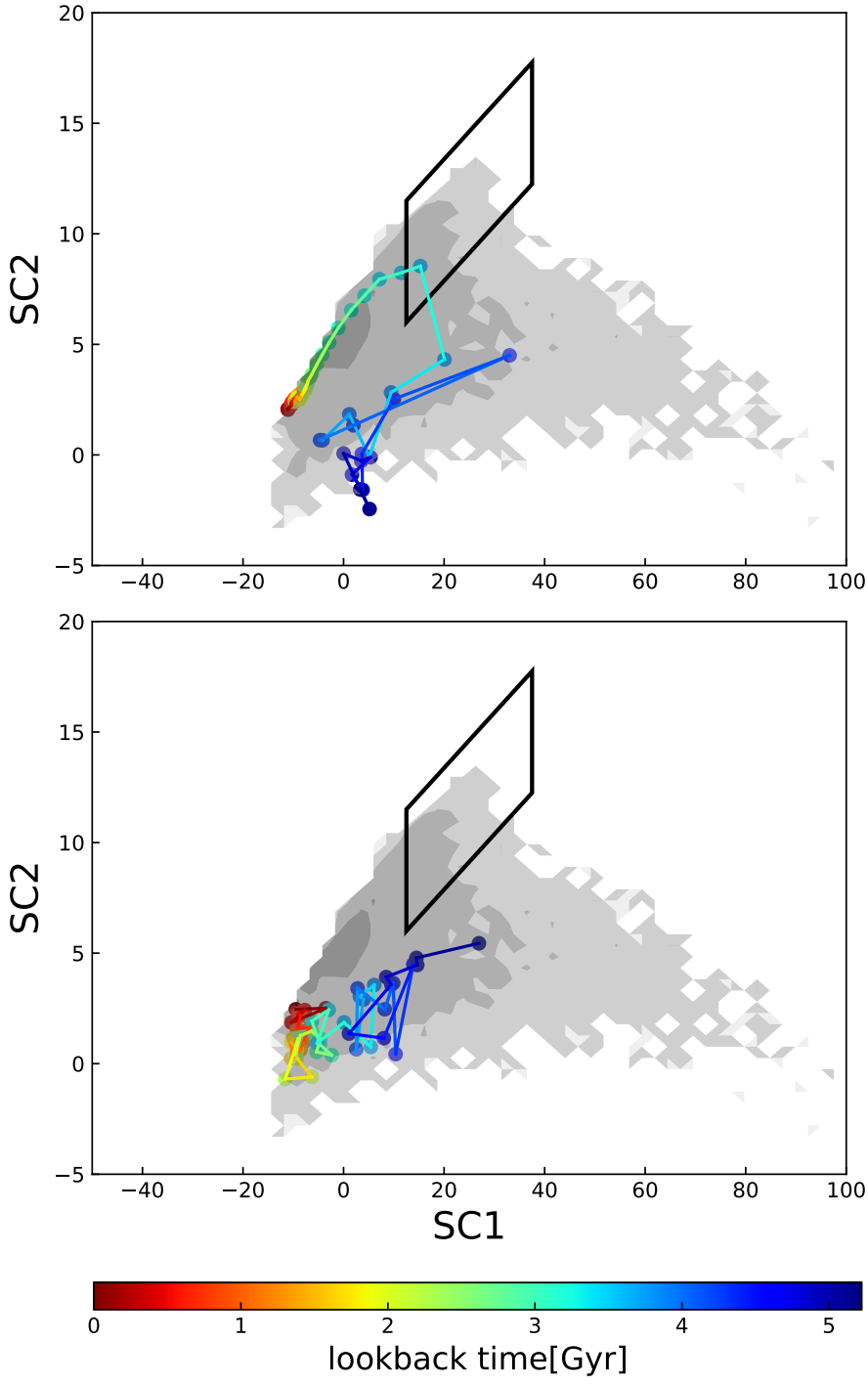

Figure 5.8: The evolutionary trace in super-colour space of the rapidly quenched (upper panel) and slowly quenched (lower panel) galaxies displayed in Figure 5.1. The underlying grey contours show the distribution of SIMBA galaxies at redshift $z \sim 1$. The colour bar indicates look-back time from $z = 0.5$, where these two galaxies were selected to be quiescent.

0.5 galaxies shown in Figure 5.1, coloured by lookback time since $z = 0.5$. The upper and lower panels show the rapidly and slowly quenched galaxy respectively. While the RQG moves through the box region, the slowly quenched galaxy moves directly onto the red sequence without entering the box region. I can calculate the super-colour trace of all RQGs in the $z = 1$ SIMBA snapshot, identifying those that enter the box region of super-colour space, and classifying them as "rapidly quenched" from their observed colours[3]. I expect this process to identify fewer RQGs than using the SFHs, which are not accessible observationally, because the super-colours are not a perfect selection method. Because the super-colours that I am using are only defined up to a redshift of 2, it is only possible to identify "observational" rapid quenching events that occur after this time. In the following, I ensure that I compare like-with-like when comparing SFH-selected and colour-selected RQGs by restricting the SFH-selected RQGs to those that quench below $z_q = 2$. I define z_q to be the redshift at which the sSFR of the galaxy last crosses the quiescent threshold of $0.2/t_H(z)$.

We find that 1537 out of 2623 quiescent galaxies at redshift $z \sim 1$ in SIMBA have a quenching timescale of $\tau_q \leq 175$ Myr, i.e. $\sim 59\%$ have been rapidly quenched. Summing their stellar masses, we find they contribute $\sim$48% of the stellar mass in the red sequence. Restricting to those galaxies with $z_q < 2$, we find 1315 out of these 2314 quiescent galaxies are SFH-defined RQGs making up $\sim$57% of the red sequence in terms of number count and $\sim$45% in terms of stellar mass. I then check the traces of the 1315 SFH-defined RQGs, and find that 1247 of them once enter the box in super-colour space. Thus, 1247 out of 2314 quiescent galaxies are RQGs that can be identified by the super-colour selection, making up $\sim$54% of the red sequence in terms of number count while only $\sim$38% in terms of stellar mass.

The numbers show that the super-colour selection identifies most of the SFH-selected RQGs but preferentially misses the more massive RQGs. To investigate this further, in the upper panel of Figure 5.9 I display the mass function of the quiescent galaxy population at $z = 1$, with a black dashed line for all quiescent galaxies, and black solid line for galaxies with $z_q < 2$, alongside those quiescent galaxies identified as rapid quenchers by their SFH (dashed red line) or from having passed through the box in super-colour space since $z < 2$ (solid red line). I assume Poisson errors when I count the galaxies in each mass bin, and these are then propagated into the mass function. The mass function peaks between $10^{10}\mathrm{M}_\odot$ and $10^{11}\mathrm{M}_\odot$,

[3]We linearly interpolate the SC1-SC2 points between individual snapshots to identify whether a galaxy enters the region, rather than using the snapshots alone.

with fewer lower and higher mass quiescent galaxies as expected. By restricting the analysis to galaxies with $z_q < 2$ I loose a small fraction of quiescent galaxies, with a slight bias to preferentially loosing the more massive ones.

Clearly the shape of the mass function of the RQGs is similar to that of the total quiescent population, but to better compare the three mass functions, their ratios are plotted in the lower panel of Figure 5.9. The green line compares the mass function of the SFH-selected RQGs with the SC-selected RQGs, while the red lines compare the mass functions of the RQGs with the quiescent population with $z_q < 2$. The dashed black lines indicate the ratios of 0.5, 1, and 2 for easy reference. We see that for the majority of the quiescent population, the rapid quenching route makes up a little over half by number count of all quiescent galaxies. The dominant difference between the shape of the mass functions is at the high mass end, with RQGs having a lower typical stellar mass than the overall quiescent population, highlighting that the rapid quenching routes are more important in the low/median mass galaxies. This coincides with the mass range where SIMBA's jet feedback is dominant, consistent with the idea that the star formation in these RQGs is rapidly quenched by the violent jet feedback. I also note an apparent drop in contribution of RQGs at lower masses, and it is possible that ongoing accretion prevents these galaxies from depleting their gas rapidly enough to be selected. However, the smaller number of galaxies in the lowest mass bin make this result uncertain.

From the green dashed line indicating the ratio of SC-selected RQGs to SFH-selected RQGs, we see that almost all RQGs are identified observationally at stellar masses below 10^{11} $M_\odot$. At the high mass end, some SFH-selected RQGs can be missed by the super-colour identification. We visually inspected the SFHs and super-colour traces of the 49 RQGs with $M_* > 10^{11}$ $M_\odot$ that are not identified by their SC traces. I found that they fall into two groups: 1) the galaxy does not have a high enough sSFR prior to quenching to show sufficiently strong spectral features to enter the box in super-colour space; 2) the galaxy has a fluctuating SFH after being quenched and although the sSFR never returns above the star-forming threshold, the weak rejuvenation event(s) complicate the super-colour trace of the galaxy, preventing it from entering the selection box. This process appears to be particularly prevalent in the highest mass galaxies.

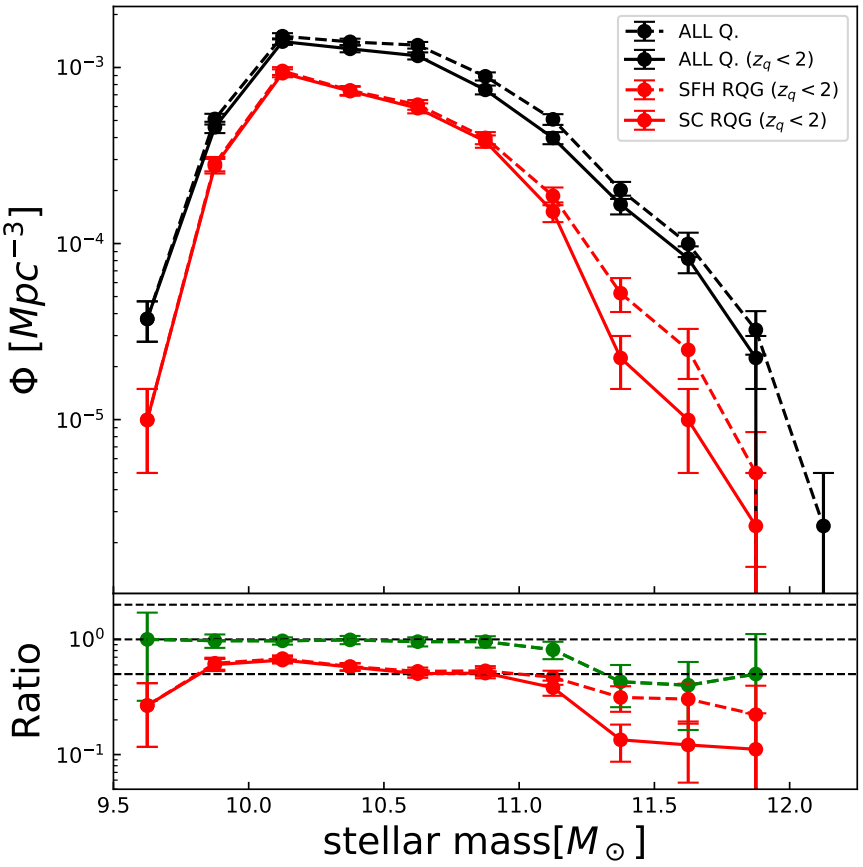

Figure 5.9: *Upper panel*: The $z = 1$ mass function of all quiescent galaxies (black dashed line, sSFR $< 0.2/t_H(z = 1)$) and those quenched after redshift $z_q < 2$ (black solid line); the SFH-identified rapidly quenched galaxies (red dashed line, $\tau_q \leq 175$ Myr) and the super-colour identified rapidly quenched galaxies (red solid line). The error bars here are the Poisson errors in each bin. *Lower panel*: the ratio of the SFH-selected RQGs to all quiescent galaxies quenched after redshift $z_q = 2$ (dashed red line), the super-colour selected RQGs to all quiescent galaxies quenched after redshift $z_q = 2$ (red solid line) and the super-colour selected RQGs to the SFH-selected RQGs (green dashed line). The black dashed lines indicate ratios of 0.5, 1 and 2.

5.2.3 Visibility timescales

Understanding the visibility timescale of RQGs or PSBs is an active topic for astronomers, as this allows an estimate of the mass growth of red sequence through the rapid quenching route without tracking the individual SFHs of galaxies only accessible via high quality continuum spectroscopy. For simulated RQGs in SIMBA, a direct measurement of visibility timescale can be more easily obtained.

We define the visibility timescale of RQGs as the duration over which the galaxies stay in the box region of super-colour space. The time-spacing of the SIMBA snapshots is coarse relative to the visibility timescale, therefore it is not possible to do this precisely based on the snapshots only, and I instead use the linear interpolation in SC space to estimate the visibility time. For the small fraction of traces that start in the box, i.e. at $z = 2$ the galaxy is already quenching, I simply take the time of $z = 2$ as a entering time. Similarly, for traces that end in the box, I take the time of $z = 0.5$ as a leaving time. Some galaxies may enter and leave the box region several times due to fluctuations in their SFHs, and for these I accumulate all the time the galaxies super-colours are within the box. At $z = 0.5$, there are 2938 quiescent galaxies that have passed through the box region with a median visibility time of 390 Myr.

The median visibility timescale of RQGs decreases as the redshift decreases, from 513 Myr for galaxies that quenched between $1.25 < z_q < 2$, to 398 Myr for galaxies that quenched between $0.75 < z_q < 1.25$ and 292 Myr for galaxies that quenched at $0.5 < z_q < 0.75$ respectively (see the distributions of visibility timescales in Figure 5.10). This difference likely arises due to the higher sSFR of galaxies at higher redshifts, causing stronger observed features in the SEDs which remain for longer.

These values are not directly comparable to observational results, due to the difference in super-colour distributions between SIMBA and the UDS meaning that different boxes were used to identify the RQGs. Therefore, the value of 390 Myr, compared to 0.5-1 Gyr in Wild et al. (2020) is likely consistent within the uncertainties. This calculation should certainly be revisited when simulations are able to produce the overall colour distributions of galaxies more accurately.

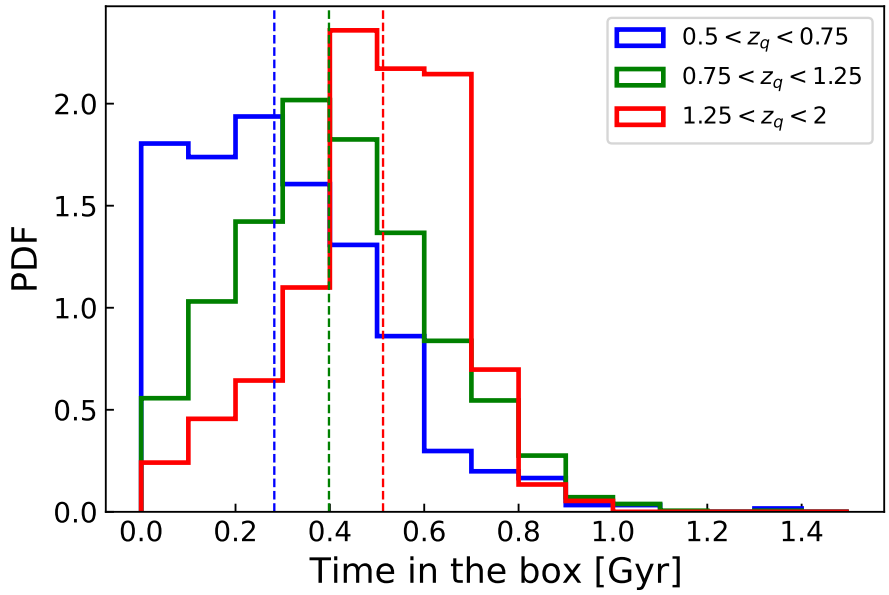

Figure 5.10: The probability density function (PDF) of the visibility timescales of RQGs quenched in different redshift bins. The solid lines show the PDF of each bin while the dashed vertical lines show the median visibility timescales. The median visibility timescale of RQGs decreases as the redshift decreases, from 513 Myr for galaxies that quenched between $1.25 < z_q < 2$, to 398 Myr for galaxies that quenched between $0.75 < z_q < 1.25$ and 292 Myr for galaxies that quenched at $0.5 < z_q < 0.75$ respectively.

5.2.4 Redshift evolution

Observations have suggested that the importance of the rapid quenching route appears to decrease with decreasing redshift and may rapidly diminish at $z < 1$ (Wild et al., 2016; Rowlands et al., 2018b; Belli et al., 2019). Here I investigate the redshift evolution of RQGs in the SIMBA simulated galaxies. I first select 3257 rapidly quenched SIMBA galaxies with $\tau_q \leq 175$ Myr in the $z = 0.5$ snapshot, and separate them into 3 different redshift bins depending on the redshift at which the galaxy was quenched (z_q): $1.25 < z_q < 2$ (361 galaxies), $0.75 < z_q < 1.25$ (1874 galaxies), and $0.5 < z_q < 0.75$ (650 galaxies)[4]. The mass functions of these three samples are shown in the top-left panel of Figure 5.11, using the total stellar masses of the galaxies at the time they were quenched. The top-centre panel shows the same result using only those RQGs which *also* pass through the region of super-colour space which would allow them to be detected observationally.

The SIMBA RQG mass functions show a strong redshift evolution, with high-mass RQGs ($M^* > 10^{11} M_\odot$) predominantly present in the $0.75 < z_q < 1.25$ and $1.25 < z_q < 2$ samples. The number density of intermediate mass RQGs ($10^{10} < M^*/M_\odot < 10^{11}$) increases rapidly

[4]The remaining 372 RQGs were quenched before $z = 2$, hence are not included in this analysis.

between $1.25 < z_q < 2$ and $0.75 < z_q < 1.25$. As time goes on, the mass function retains its shape but the overall number density decreases to the $0.5 < z_q < 0.75$ sample. The left and middle panels show very similar results, showing that the observational super-colour selection method for RQGs is able to tell a qualitatively similar story.

The lower panels of Figure 5.11 show the ratio of RQGs to the total numbers of galaxies quenched during each redshift bin in SIMBA, with a pure SFH selection on the left, and including the super-colour selection in the middle. Note that this only includes galaxies quenched within the redshift interval, rather than the full number of quenched galaxies at that redshift. In the high redshift bin ($1.25 < z < 2$) we see that the majority of galaxies that are quenched in this redshift range are quenched rapidly, at all masses. As redshift decreases, the rapid quenching pathway remains important at lower masses, but a smaller fraction of high mass galaxies pass through the rapid quenching pathway. Again, the overall qualitative trends are identified when the super-colours are used to identify the RQGs.

The top-right panel of Figure 5.11 shows the mass function of super-colour selected RQGs in the UKIDSS Ultra Deep Survey (UDS) for comparison, which is recreated using the data of Wild et al. (2016) with the same redshift and mass bins as used in this chapter. Although they are named post-starburst galaxies in the observational work, this is only a matter of differing terminology as they are selected using a similar "box" in super-colour space designed to catch the spur of galaxies to the upper right of the red sequence. In the $1.25 < z_q < 2$ redshift bin, we see a very similar shape to that seen in SIMBA, and there is also a similar redshift evolution at high masses. However, there are three distinct differences. Firstly, the loss of high mass RQGs clearly starts at a higher redshift in the data than in SIMBA. Secondly, at intermediate redshift, the number of intermediate mass RQGs ($10^{10} < M^*/M_\odot < 10^{11}$)) is significantly overestimated by SIMBA. Thirdly, in the low redshift bin the observations are dominated by low-mass RQGs ($M^* < 10^{10} M_\odot$) which are entirely absent in SIMBA. The first and second discrepancy may be related, implying the jet mode feedback is operating too efficiently at $0.75 < z < 1.25$ causing too much rapid quenching in this redshift range. There are several possible reasons for the third discrepancy: 1) numerical effects caused by the limited SIMBA resolution (the galaxies at these masses have only ∼275 stellar particles); 2) the AGN jet feedback in SIMBA is too subdominant in these less massive galaxies; 3) environmental effects are not modelled sufficiently accurately in SIMBA. Detailed reasoning or proof for this hypotheses is difficult to obtain and the subject of future work.

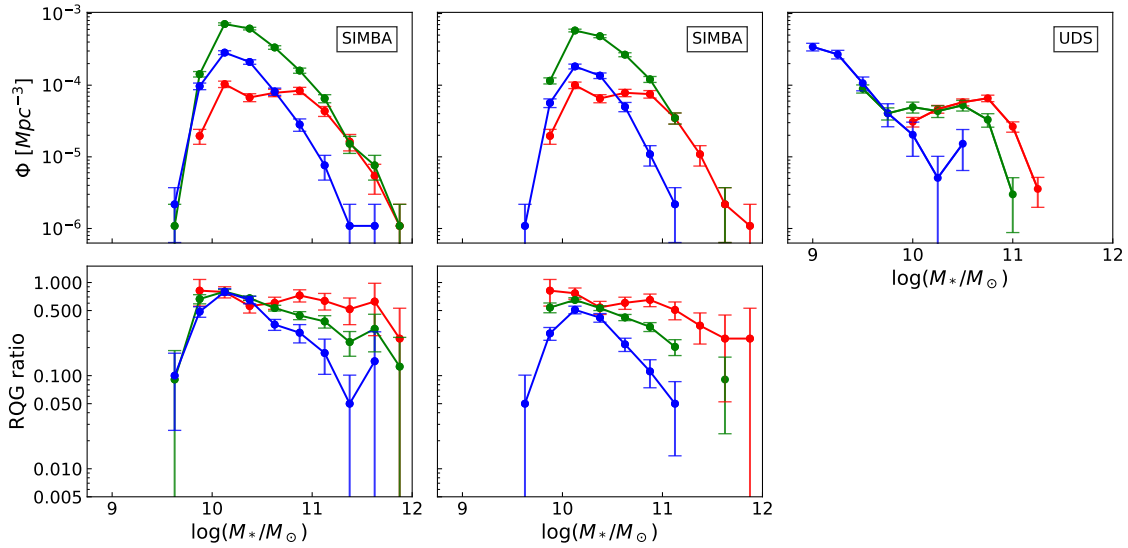

Figure 5.11: *Top left:* The mass functions of RQGs identified from their SFH to have $\tau_q \leq 175$ Myr in the $z = 0.5$ SIMBA snapshot, which were quenched at $1.25 < z_q < 2$ (red), $0.75 < z_q < 1.25$ (green) and $0.5 < z_q < 0.75$ (blue). The stellar mass is the mass at the time of quenching and the errors are propagated from Poisson errors on the number counts. *Top centre:* Same as top left, but for RQGs that *also* pass through the RQG region of super-colour space. *Top right:* The mass functions for RQGs in the UKIDSS UDS survey, taken from the catalogue of (Wild et al., 2016). *Bottom*: the ratio of the number of RQGs to the total number of galaxies that are quenched during each redshift interval. On the left the RQGs are identified from their SFHs alone, and in the middle they *also* pass through the RQG region of super-colour space. Note that there is no easy observational comparison to these lower panels, as it is more challenging to identify galaxies that recently quenched slowly than to identify RQGs.

5.2.5 "Rapidly quenched" or "post-starburst" galaxies?

In SIMBA, the red sequence in super-colour space lacks the clear spur of RQGs to the upper-right, that is well separated from the star-forming cloud like in the UDS data. By fitting models to good quality spectra and multi-wavelength photometry of galaxies in the UDS field, Wild et al. (2020) showed that these galaxies have a strong burst of star formation, hence the observationally determined name of "post-starburst" galaxies. Given the limited resolution, SIMBA may not be able to produce the sharp bursts often invoked to represent PSBs[5], and in Figure 5.7 the star formation histories do not show an obvious sharp rise prior to the quenching in most cases. Here I investigate the impact on the colour distribution of adding a pseudo-burst to the star formation histories of the quenching galaxies. I first select the galaxies that lie between the star-forming and quiescent thresholds, i.e. $0.2/t_H < sSFR < 1/t_H$ in the $z = 1$ snapshot. I then identify all newly formed stellar particles with an age < 300 Myr and the manually change their age to 300 Myr so that these galaxies then have a pseudo starburst 300 Myr ago followed by complete quenching of the star formation. The stellar population synthesis process, the line-of-sight dust extinction, photometry and super-colour computation are then carried out as for the original analysis of the SIMBA galaxies, and the resulting super-colour distribution is shown in Figure 5.12. With this pseudo-burst the thin spur to the upper-right of the red sequence is now as obvious as in UDS observations. Hence I conclude that the lack of this feature in SIMBA is likely a direct result of galaxies not undergoing strong enough rapid starbursts. For this reason, the term "rapidly quenched galaxy" is more appropriate for the SIMBA galaxies, while in the real Universe it seems that most galaxies in this region of super-colour space are in fact "post-starburst galaxies"

5.3 Discussion

Unlike in RM19, I adopt a slightly different definition of rapid quenching: the quenching timescale is *not* scaled by the Hubble time in this chapter. The bimodality in quenching timescale still exists and I argue that this definition has two advantages: 1) the quenching timescale is comparable to the stellar evolution timescale of the massive stars that dominate the spectral properties, thus it is easier to link the RQGs in SIMBA with those identified by their

[5]Note that the BH feedback model adopted in SIMBA might also be partially blamed for the lack of the PSBs. It has been implied that the jet mode feedback is operating too efficiently at $0.75 < z < 1.25$, which can eliminate the potential starburst and result a direct rapidly quenching

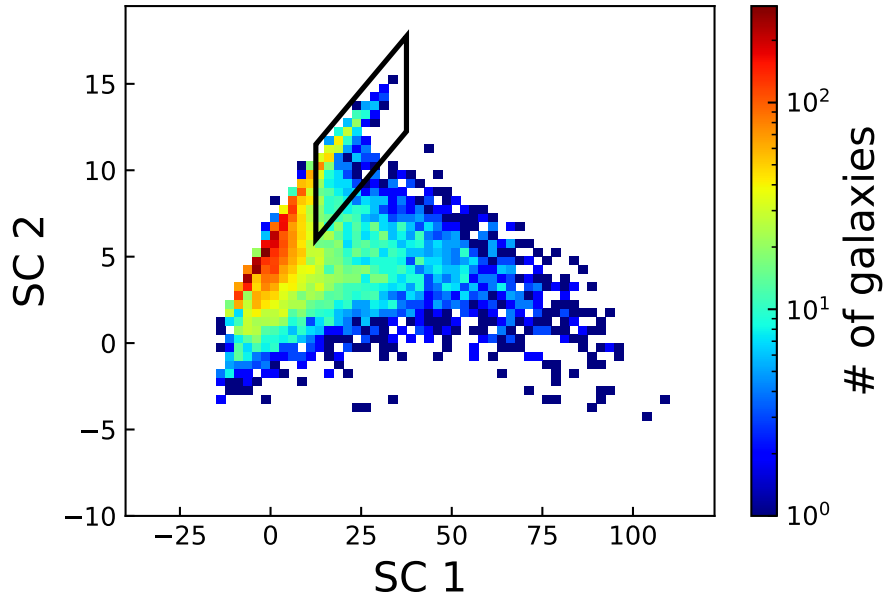

Figure 5.12: The super-colours of SIMBA $z = 1$ galaxies with a "pseudo-burst" added (see text for details). This causes a much more prominent spur to the upper-right end of the red sequence, similar to that seen in the UDS data (Figure 5.3).

observed spectral energy distributions; 2) this definition is more likely to relate to any physical timescale of catastrophic events that could rapidly halt star formation in galaxies, rather than slow gas-consumption type quenching mechanisms that might be expected to scale with the Hubble time. It is in part this different definition of RQGs that allows me to identify that quenching events at $z = 1$ and above are preferentially rapid, a trend that is missed in RM19. However, both definitions guide me to the conclusion that a significant fraction of quiescent galaxies are quenched via rapid processes, different from the common assumption that rapid quenching is largely unimportant (see e.g. Trussler et al., 2020; Peng et al., 2010, 2015). Though observations suggest that importance of the fast-quenching route may rapidly diminish at $z < 1$ (Rowlands et al., 2018b), the contribution from RQGs to the growth of the red sequence should not be ignored, at least over the first half of cosmic history.

We still do not have a clear idea about what mechanisms are responsible for the rapid quenching. Both RM19 and my results find that the rapid quenching route is important for galaxies with stellar masses around 10^{10}–10^{11}M$_\odot$. This mass range coincides with where supermassive black hole driven jet feedback is effective in SIMBA, suggesting that the fast quenching is likely associated with the violent expulsion of gas by the jets. In my binary merger simulations introduced section 2.1, it is confirmed that AGN feedback is necessary to fully shut down the star formation in post-merger, post-starburst galaxies. However, I also find that

the star formation in starburst galaxies can be rapidly suppressed to a “main-sequence” level without any contribution from black hole feedback, which supports the picture that stellar feedback can also play an important role in the rapid quenching route, at least in the early post-starburst phase. The stellar feedback helps driving gas outflows and disrupting the giant molecular clouds, which contributes to the end of the starburst. The exact role of stellar feedback in quenching remains unclear, and more discussion can be found in French (2021). As SIMBA does not reproduce enough starburst galaxies (see subsection 5.2.5), the contribution from stellar feedback to the rapid quenching will not be fully included, leading to a potential underestimation in the importance of fast quenching route, or need for enhanced AGN feedback to be included. It would certainly be valuable to further investigate the mechanisms that are responsible for the fast quenching route in SIMBA. Investigating other cosmological simulations such as Illustris-TNG (Pillepich et al., 2018) and EAGLE (Schaye et al., 2015) could also help answer the question.

Mergers are believed to be an important route for rapid evolution to early-type galaxies through a starburst phase. Observationally, in the local Universe at least, many PSBs/RQGs are found to have tidal features. The consistency between the observed rates of PSBs and the merger rates at $z \lesssim 1$ also suggests a predominantly merger origin of rapid quenching (Snyder et al., 2011). However, RM19 find a different picture in SIMBA: not enough mergers are spotted to explain the number of quenched massive galaxies at $z \lesssim 1.5$. Furthermore, they find that galaxy quenching has no obvious correlation with major mergers in SIMBA, disconnecting the rapid quenching route from merger induced starbursts (see also Quai et al., 2021, for a similar result in Illustris-TNG). Research in the EAGLE simulation also challenges the simple assumption that mergers are the only origin of RQGs: about a half of merger induced PSBs will not be in fact transitioning into quiescent galaxies (Pawlik et al., 2019) and environment effects are found to be important for the creation of PSBs (Davis et al., 2019). Clearly further work is required to understand these apparently disparate results, both observationally and theoretically.

Observationally the rapidly quenched satellites in clusters are found near to cluster centres (Owers et al., 2019b), and it is now well established that the fraction of PSBs steadily increases from 1% in field to $\sim$ 15% in dense clusters (Socolovsky et al., 2018; Paccagnella et al., 2019). Unlike galaxies in the field, galaxies in a dense environment are expected to experience a much “harder life": ram pressure stripping, galaxy harassment, thermal evaporation, and starvation.

These additional processes are expected to help to rapidly stop the star formation and result RQGs. In SIMBA it is found that central galaxies are more likely to be rapidly quenched compared with satellites galaxies at the same stellar mass (Rodríguez Montero et al., 2019). Thus, I can expect that the RQGs identified in this chapter are more likely to be central galaxies, rather than galaxies that have recently entered a large overdensity. Further comparison of the environments of RQGs in observations and simulations may help identify further similarities and differences between the real and simulated Universe.

5.4 Summary

In this chapter I have investigated rapidly quenched galaxies (RQGs) in the SIMBA cosmological simulation and compared them to observations. I track the progenitors of the quiescent galaxies to obtain their star formation histories (SFHs). From their SFHs I measure the quenching timescale τ_q, the time that the galaxies take to cross from a star-forming threshold to the quiescent threshold. I confirm the bimodal distribution of quenching timescales, and divide the quiescent galaxies into rapidly quenched and slowly quenched galaxies. Mock photometric data are created and a super-colour analysis is carried out in order to compare the simulation to observations.

The findings of this chapter are summarised below:

1. As seen in RM19 the quenching timescales of quiescent galaxies in SIMBA show a stark bimodality with the division at $\tau_q = 175$ Myr, dividing the quiescent galaxies into rapidly quenched galaxies and slowly quenched ones.

2. The quiescent galaxies in SIMBA form a tight sequence in super-colour space, similar to that observed observationally, although offset in exact positioning.

3. In SIMBA, the blue cloud blends with the quiescent population in super-colour space unlike the observed blue sequence, which is probably due to an inaccurate dust treatment. Besides, the discrepancies between the super-colours of galaxies in SIMBA and the observational UDS dataset hint that SIMBA is not perfect in terms of creating the right types of star formation and metallicity histories.

4. The super-colour distribution additionally shows that SIMBA lacks galaxies that have undergone strong enough rapid starbursts, thus, the red sequence in super-colour space

lacks the clear spur of RQGs to the upper-right that is seen in observations.

5. 95% of SIMBA RQGs pass through the upper-right region of super-colour space observationally identified as containing post-starburst galaxies, proving that the super-colour method is an effective selection technique to identify RQGs. However, there is some mass dependence, with a smaller fraction identified via their super-colours at stellar masses above 10^{11} $M_{\odot}$.

6. We find that 59% of the the quiescent galaxies at $z = 1$ in SIMBA have been rapidly quenched with $\tau_q < 175$ Myr, contributing ∼48% of the stellar mass growth of the red sequence. This is at the upper end of the ∼25-50% derived observationally by Wild et al. (2020) at $0.5 < z_q < 2$, and higher than that estimated by Belli et al. (2019) at $z \sim 1.4$.

7. RQGs have a lower typical stellar mass than the overall quiescent population, with a distinct reduction in the importance of the rapid quenching route below $10^{11}M_{\odot}$. This coincides with the mass range where SIMBA's jet feedback is dominant, consistent with the idea that the star formation in these RQGs is rapidly quenched by the violent jet feedback.

8. At $z = 0.5$, the RQGs that have passed through the box region of super-colour space have a median visibility time of 390 Myr, which is a little short compared to the 0.5-1 Gyr estimated observationally by Wild et al. (2020). However, the difference may be caused by the differing boundaries necessitated by the shift in super-colours between observations and simulation. Interestingly, the visibility timescale of RQGs decreases as redshift decreases, a result which requires observational verification with higher redshift spectroscopic samples.

9. In SIMBA the importance of the rapid quenching route decreases with decreasing redshift for galaxies with stellar masses $> 10^{10}M_{\odot}$, but remains important for galaxies with lower stellar mass even at $z = 0.5$. However, the mass functions of RQGs do not compare perfectly with observations, with a significant excess of intermediate and high mass RQGs at $1 < z_q < 1.5$ and lack of low mass RQGs at $0.5 < z_q < 1$ in SIMBA compared to observations. This implies that the jet mode feedback is operating too efficiently at $0.75 < z < 1.25$ causing too much rapid quenching in this redshift range.

Clearly much more remains to be understood about the rapidly quenched galaxies. The

SIMBA simulation helps us to investigate the importance of the rapid quenching pathway and its evolution at different stellar mass and different redshift. Exactly which mechanism(s) is/are responsible for the rapid quenching remains as intriguing problems to be solved in the future. The discrepancies between the properties of simulated RQGs in SIMBA and real RQGs in observations suggest some flaws in SIMBA, which will help the future improvement of the simulations. I am looking forward to improved galaxy evolution simulations, as well as more high-redshift spectroscopic data, in order to continue my investigations into rapidly quenched galaxies.

6

SUMMARY AND FUTURE WORK

6.1 Summary

In this thesis, I combine simulations and observations to investigate an important transitioning galaxy population, post-starburst galaxies. I utilise a set of binary merger simulations run by myself and a cosmological simulation run by my collaborators. The SEDmorph code is developed and extended to create integral field datacubes for binary merger simulations, while PYLOSER is applied to produce photometry data for SIMBA galaxies. I compare the mock observations to the real ones to investigate what mechanisms produce PSBs and how important PSBs are to growth of the red sequence. Here I summarise what I do and what I find in each chapter.

In chapter 2, I introduce the simulations used throughout my PhD project. I run a set of binary mergers simulations with a variety of black hole feedback models, progenitor galaxies, orbits and mass ratios. This chapter gives the details of the sub-resolution physics of the simulations, setting up of the model galaxies and the mergers. I want to emphasise the black hole

feedback models in this chapter, as these models turn out to have very different performance on quenching the post-starburst galaxies. The cosmological simulation SIMBA is also described in this chapter. I describe the basic information of SIMBA and highlight the dichotomy in its BH feedback model. How galaxies are resolved in SIMBA is also given in this chapter.

In chapter 3, I introduce the SEDmorph code that is used to create mock observations for simulated galaxies. I use the information of stellar particles to create stellar continuum with the BC03 spectral synthesis models. A two-component dust attenuation model is applied to include the dust attenuation effect. A few alternative methods to forward-model the stellar continuum are also introduced in this chapter for the discussion on whether it is necessary to include the light from the star-forming gas particles. I find it is not required to count the gas contribution to the spectra at the resolution of my simulations. I further developed and extended the SEDmorph code to create integral field datacubes following the MaNGA observational strategy. A seeing (atmospheric) point spread function (PSF) and a dither pattern are included when building the row stacked spectrum (RSS) files. Finally, I combine the RSS into a regularly gridded datacube. I also investigate several alternative procedures to produce mock MaNGA cubes. However, I find that it is necessary to strictly follow the MaNGA observation strategy. Short cuts such as gridding data directly, or convolving with the PSF after data gridding produce significant residuals or larger computational resources compared to a full treatment.

In chapter 4, I was motivated by radial gradients observed in the optical spectral indices of post-starburst galaxies, I applied the SEDmorph code to my binary merger simulations set to create mock spectra and IFU datacubes. I find that only major mergers on prograde-prograde or retrograde-prograde orbits in combination with a mechanical black hole feedback model can form galaxies with weak enough ongoing star formation, and therefore absent Hα emission, to be selected by traditional PSB selection methods. I find strong fluctuations in nebular emission line strengths, even within the PSB phase, suggesting that Hα selected PSBs are only a subsample of the underlying population. The global PSB population can be more robustly identified using stellar continuum-based approaches. The difficulty in reproducing the very young PSBs in simulations potentially indicates that new sub-resolution star formation recipes are required to properly model the process of star formation quenching. In my simulations, I find that the starburst peaks at the same time at all radii, but is stronger and more prolonged in the inner regions. This results in a strong time evolution in the radial gradients of the spectral

indices which can be used to estimate the age of the starburst without reliance on detailed star formation histories from spectral synthesis models.

In chapter 5, I study the population of rapidly quenched galaxies (RQGs) in the SIMBA cosmological hydrodynamic simulation at $0.5 < z < 2$, comparing directly to observational PSBs in the UKIDSS Ultra Deep Survey via their colour distributions and mass functions. We find that 59% of the the quiescent galaxies at $z = 1$ in SIMBA have been rapidly quenched with $\tau_q < 175$ Myr, contributing ∼48% of the stellar mass growth of the red sequence, which is higher than observed. A similar "downsizing" of RQGs is observed in both SIMBA and the UDS, with RQGs at higher redshift having a higher average mass. However, the mass functions of RQGs do not compare perfectly with observations, with a significant excess of intermediate and high mass RQGs at $1 < z_q < 1.5$ and lack of low mass RQGs at $0.5 < z_q < 1$ in SIMBA compared to observations. The precise colour distribution of SIMBA galaxies compared to the observations also indicates various inconsistencies in star formation and chemical enrichment histories, including an absence of short, intense starbursts. These results will help inform the next generation of galaxy evolution models, particularly with respect to the quenching mechanisms employed.

6.2 Future work

Combining simulations and observations does help us understand post-starburst galaxies and the quenching mechanisms. There are many directions could be taken further. Here I briefly describe some potential projects in the near future.

1). Super-colour analysis across different cosmological simulations: Besides the SIMBA simulation analysed in this thesis, a great set of large cosmological simulations have been carried out and are now publicly available, e.g. EAGLE (Schaye et al., 2015), Illustris-TNG (Pillepich et al., 2018), NewHorizon (Dubois et al., 2020) and so on. As revealed in subsection 5.1.4, super-colour analysis helps finding out whether the simulation creates the right types of star formation and chemical evolution histories. A natural step is to carry out super-colour analysis across different simulation models. With the tools that I developed for SIMBA, I will check how the statistical properties of fast quenched galaxies vary in different simulations. Interesting properties include the total contribution to the growth of the red sequence, the mass function, the number density, and their evolution as a function of redshift. Compari-

son between the SCA results of simulations to those of real observations will be carried out to figure out what kind of SFH are successfully/unsuccessfully reproduced and whether the relative fractions of different types of SFH are correct. It can be interesting to compare my results from mock photometry to the findings in Iyer et al. (2020), in which the researchers use the power spectral density to investigate the SFH variability in different cosmological simulations. These results will help constraining the simulation models and improve our understanding on galaxy quenching mechanisms.

2). Spatially resolved super-colour analysis in simulations and observations: The recent CANDELS *Hubble Space Telescope* survey (Grogin et al., 2011; Koekemoer et al., 2011) provides multi-wavelength photometry for a large sample of galaxies with good spatial resolution. I propose to carry out super-colour analysis on different regions of galaxies to check whether galaxy centres are quenched in the same mode as the galaxy outskirt, motivated by the finding that the quenching timescales at the galaxy centre is longer than that in the galaxy outskirt in my binary merger simulations (see Figure 4.7). With high-resolution simulations and the SEDmorph code, we can create a mock CANDELS survey in simulated universes and then use the results to interpret the observations. As simulations provide the detailed SFHs of the galaxies, the quenching timescales in different regions of the simulated galaxies can be measured. Besides, it is worth investigating the connection between the difference of the quenching timescales at different radii to the inside-out/outside-in quenching mode. I will compare the results to the findings in DEugenio et al. (2020), who find inverse stellar population age gradients of post-starburst galaxies at $z = 0.8$ with LEGA-C spectroscopic survey.

3). Different effect of black hole feedback models on galaxy quenching: The black hole feedback plays a significant role in the quenching of the quiescent galaxies at least in the fast quenched ones (Kaviraj et al., 2007b; French et al., 2018; Pawlik et al., 2018). My merger simulations also suggest that mechanical AGN feedback is required to completely shut down the star formation in our model PSB galaxies. However, not all study in simulations agree with the picture above. For instance, Davis et al. (2019) finds that AGN play only a secondary role in EAGLE. The disagreement is possibly resulted by the different black hole feedback models. However, it is hard to decide how the different BH models change the quenching processes since these simulations adopted sub-resolution physics like different star formation, stellar feedback models and gas cooling process, etc. Fortunately, modular structure simulation codes (e.g., SWIFT by Schaller et al. (2018)) allow users to choose what physical models we need

in simulations. It could be helpful to run zoom-in simulations adopting different BH accretion and feedback models while keeping other sub-resolution physics the same. Two aspects of the quenching process can be investigated: 1)Globally, how do the SFHs of the galaxies varies with different BH feedback models, whether the quenching timescale changes? 2)Spatially: how do the spatial behavior in quenching progress varies with different BH feedback models, in which cases inside-out or outside-in quenching modes is reproduced? and can these spatial behavior be distinguished by mock IFU observations?

Clearly, many intriguing work can be done in the future. I will keep studying the post-starburst galaxies in simulations and observations in the following years.

Bibliography

Abadi, M. G., Moore, B., & Bower, R. G. 1999, MNRAS, 308, 947

Abdurro'uf et al. 2021, arXiv e-prints, arXiv:2112.02026, 2112.02026

Aguado, D. S. et al. 2019, ApJS, 240, 23, 1812.02759

Almaini, O. et al. 2017, MNRAS, 472, 1401, 1708.00005

Alongi, M., Bertelli, G., Bressan, A., Chiosi, C., Fagotto, F., Greggio, L., & Nasi, E. 1993, A&AS, 97, 851

Anglés-Alcázar, D., Davé, R., Faucher-Giguère, C.-A., Özel, F., & Hopkins, P. F. 2017, MNRAS, 464, 2840

Athanassoula, E. 1992, MNRAS, 259, 328

Aumer, M., White, S. D. M., Naab, T., & Scannapieco, C. 2013, MNRAS, 434, 3142, 1304.1559

Baldry, I. K., Glazebrook, K., Brinkmann, J., Ivezić, Ž., Lupton, R. H., Nichol, R. C., & Szalay, A. S. 2004, ApJ, 600, 681

Balogh, M. L., Miller, C., Nichol, R., Zabludoff, A., & Goto, T. 2005, MNRAS, 360, 587

Balogh, M. L., & Morris, S. L. 2000, MNRAS, 318, 703

Barnes, J. E. 1992, ApJ, 393, 484

——. 2004, Monthly Notices of the Royal Astronomical Society, 350, 798

Bekki, K., Couch, W. J., Shioya, Y., & Vazdekis, A. 2005, MNRAS, 359, 949

Belfiore, F. et al. 2019, AJ, 158, 160, 1901.00866

Bell, E. F. et al. 2012, ApJ, 753, 167

Bell, E. F. et al. 2012, ApJ, 753, 167

Bell, E. F. et al. 2004, ApJ, 608, 752

Belli, S., Newman, A. B., & Ellis, R. S. 2019, ApJ, 874, 17, 1810.00008

Birnboim, Y., & Dekel, A. 2003, Monthly Notices of the Royal Astronomical Society, 345, 349

Blondin, J. M., Wright, E. B., Borkowski, K. J., & Reynolds, S. P. 1998, ApJ, 500, 342

Bondi, H. 1952, MNRAS, 112, 195

Bondi, H., & Hoyle, F. 1944, MNRAS, 104, 273

Bournaud, F. 2011, in EAS Publications Series, Vol. 51, EAS Publications Series, ed. C. Charbonnel & T. Montmerle, 107–131, 1106.1793

Bournaud, F., Jog, C., & Combes, F. 2005, A&A, 437, 69

Brammer, G. B. et al. 2011, ApJ, 739, 24

Brennan, R. et al. 2015, MNRAS, 451, 2933

Bressan, A., Fagotto, F., Bertelli, G., & Chiosi, C. 1993, A&AS, 100, 647

Bruce, V. A. et al. 2014, MNRAS, 444, 1001

Bruzual, G., & Charlot, S. 2003, MNRAS, 344, 1000

Bundy, K. et al. 2015, ApJ, 798, 7, 1412.1482

Calzetti, D., Armus, L., Bohlin, R. C., Kinney, A. L., Koornneef, J., & Storchi-Bergmann, T. 2000, ApJ, 533, 682

Cappellari, M., & Copin, Y. 2003, MNRAS, 342, 345, astro-ph/0302262

Cappellari, M. et al. 2011, MNRAS, 413, 813

Cardelli, J. A., Clayton, G. C., & Mathis, J. S. 1989, ApJ, 345, 245

Chabrier, G. 2003, PASP, 115, 763

Chang, T.-C., van Gorkom, J. H., Zabludoff, A. I., Zaritsky, D., & Mihos, J. C. 2001, AJ, 121, 1965, astro-ph/0101353

Charlot, S., & Fall, S. M. 2000, ApJ, 539, 718

Chen, Y. M. et al. 2019, MNRAS, 489, 5709, 1909.01658

Choi, E., Naab, T., Ostriker, J. P., Johansson, P. H., & Moster, B. P. 2014, MNRAS, 442, 440, 1308.3719

Choi, E. et al. 2012, MNRAS, 442, 440, 1809.02143

Choi, J., Dotter, A., Conroy, C., Cantiello, M., Paxton, B., & Johnson, B. D. 2016, ApJ, 823, 102

Connolly, A., & Szalay, A. 1999, AJ, 117, 2052

Conroy, C., & Gunn, J. E. 2010, ApJ, 712, 833

Conroy, C., Gunn, J. E., & White, M. 2009, ApJ, 699, 486

Couch, W. J., & Sharples, R. M. 1987, MNRAS, 229, 423

Crenshaw, D. M., Kraemer, S. B., & George, I. M. 2003, ARA&A, 41, 117

Croton, D. J. et al. 2006, Monthly Notices of the Royal Astronomical Society, 365, 11

Davé, R., Anglés-Alcázar, D., Narayanan, D., Li, Q., Rafieferantsoa, M. H., & Appleby, S. 2019, MNRAS, 486, 2827

Davé, R., Thompson, R., & Hopkins, P. F. 2016, MNRAS, 462, 3265

Davis, T. A., van de Voort, F., Rowlands, K., McAlpine, S., Wild, V., & Crain, R. A. 2019, MNRAS, 484, 2447

De Kool, M., Arav, N., Becker, R. H., Gregg, M. D., White, R. L., Laurent-Muehleisen, S. A., Price, T., & Korista, K. T. 2001, ApJ, 548, 609

Di Matteo, T., Springel, V., & Ilernquist, L. 2005, Nature, 433, 604, 0809.3399

Dierckx, P. 1975, J Comput Appl Math, 1, 165

Dotter, A. 2016, ApJS, 222, 8

Dressler, A., & Gunn, J. 1983, ApJ, 270, 7

Dubois, Y. et al. 2020, arXiv preprint arXiv:2009.10578

Dunn, J. P. et al. 2010, ApJ, 709, 611

DEugenio, F. et al. 2020, MNRAS, 497, 389

Eisenreich, M., Naab, T., Choi, E., Ostriker, J. P., & Emsellem, E. 2017, MNRAS, 468, 751

Emsellem, E. et al. 2011, MNRAS, 414, 888

Fabian, A. C. 2012, ARA&A, 50, 455, 1204.4114

Fagotto, F., Bressan, A., Bertelli, G., & Chiosi, C. 1994a, A&AS, 104, 365

——. 1994b, A&AS, 105, 29

Falcón-Barroso, J., Sánchez-Blázquez, P., Vazdekis, A., Ricciardelli, E., Cardiel, N., Cenarro, A. J., Gorgas, J., & Peletier, R. F. 2011, A&A, 532, A95

Fensch, J. et al. 2017, MNRAS, 465, 1934, 1610.03877

Feruglio, C., Maiolino, R., Piconcelli, E., Menci, N., Aussel, H., Lamastra, A., & Fiore, F. 2010, A&A, 518, L155, 1006.1655

French, K. D. 2021, arXiv preprint arXiv:2106.05982

French, K. D., Yang, Y., Zabludoff, A., Narayanan, D., Shirley, Y., Walter, F., Smith, J.-D., & Tremonti, C. A. 2015, ApJ, 801, 1, 1501.00983

French, K. D., Yang, Y., Zabludoff, A. I., & Tremonti, C. A. 2018, ApJ, 862, 2

Gabor, J. M., & Davé, R. 2015, Monthly Notices of the Royal Astronomical Society, 447, 374

Gadotti, D. A. 2009, MNRAS, 393, 1531, 0810.1953

Gallagher III, J. S., & Ostriker, J. P. 1972, AJ, 77, 288

Gallazzi, A., Charlot, S., Brinchmann, J., White, S. D., & Tremonti, C. A. 2005, MNRAS, 362, 41

Girardi, L., Bressan, A., Chiosi, C., Bertelli, G., & Nasi, E. 1996, A&AS, 117, 113

Goto, T. 2005, MNRAS, 357, 937

Goto, T., Kawai, A., Shimono, A., Sugai, H., Yagi, M., & Hattori, T. 2008, MNRAS, 386, 1355

Goto, T. et al. 2003, PASJ, 55, 771

Grogin, N. A. et al. 2011, ApJS, 197, 35

Gunn, J. E., & Gott III, J. R. 1972, ApJ, 176, 1

Haardt, F., & Madau, P. 2001, arXiv preprint

Hernquist, L. 1990, ApJ, 356, 359

Hopkins, P. F. 2015, MNRAS, 450, 53

Hopkins, P. F. et al. 2010, The Astrophysical Journal, 715, 202

Hopkins, P. F., Hernquist, L., Cox, T. J., Di Matteo, T., Robertson, B., & Springel, V. 2006, A&AS, 163, 1

Hopkins, P. F., & Quataert, E. 2011, MNRAS, 415, 1027

Hoyle, F., & Lyttleton, R. A. 1939in , Cambridge University Press, 405–415

Hu, C.-Y., Naab, T., Walch, S., Moster, B. P., & Oser, L. 2014, MNRAS, 443, 1173

Ilbert, O. et al. 2013, A&A, 556, A55, 1301.3157

Iwamoto, K., Brachwitz, F., Nomoto, K., Kishimoto, N., Umeda, H., Hix, W. R., & Thielemann, F.-K. 1999, ApJS, 125, 439, astro-ph/0002337

Iyer, K. G. et al. 2020, MNRAS, 498, 430

Johansson, P. H., Burkert, A., & Naab, T. 2009, ApJ, 707, L184, 0910.2232

Johansson, P. H., Naab, T., & Burkert, A. 2009, ApJ, 690, 802, 0809.3399

Karakas, A. I. 2010, MNRAS, 403, 1413

Kauffmann, G. et al. 2003, MNRAS, 341, 33

Kaviraj, S., Kirkby, L. A., Silk, J., & Sarzi, M. 2007a, MNRAS, 382, 960, 0707.3570

——. 2007b, MNRAS, 382, 960

Kaviraj, S., Schawinski, K., Silk, J., & Shabala, S. S. 2011, MNRAS, 415, 3798

Kennicutt, R. C. 1998, ARA&A, 36, 189

Kennicutt Jr, R. C. 1998, The Astrophysical Journal, 498, 541

Kereš, D., Katz, N., Weinberg, D. H., & Davé, R. 2005, Monthly Notices of the Royal Astronomical Society, 363, 2

Khochfar, S., & Ostriker, J. P. 2008, The Astrophysical Journal, 680, 54

Kilian-Montenbruck, J., Gehren, T., & Nissen, P. 1994, A&A, 291, 757

Koekemoer, A. M. et al. 2011, ApJS, 197, 36

Krumholz, M. R., & Gnedin, N. Y. 2011, ApJ, 729, 36

Lahén, N., Johansson, P. H., Rantala, A., Naab, T., & Frigo, M. 2018, MNRAS, 475, 3934, 1709.00010

Lang, P. et al. 2014, ApJ, 788, 11

Larson, R., Tinsley, B., & Caldwell, C. N. 1980, ApJ, 237, 692

Lavery, R. J., & Henry, J. P. 1988, ApJ, 330, 596

Law, D. R. et al. 2016, AJ, 152, 83, 1607.08619

——. 2015, The Astronomical Journal, 150, 19

Lawrence, A. et al. 2007, MNRAS, 379, 1599

Le Borgne, J.-F. et al. 2003, A&A, 402, 433

Li, Z., French, K. D., Zabludoff, A. I., & Ho, L. C. 2019, ApJ, 879, 131, 1906.01890

Madau, P., & Dickinson, M. 2014, ARA&A, 52, 415

Madau, P., Pozzetti, L., & Dickinson, M. 1998, ApJ, 498, 106

Maltby, D. T., Almaini, O., Wild, V., Hatch, N. A., Hartley, W. G., Simpson, C., Rowlands, K., & Socolovsky, M. 2018, MNRAS, 480, 381, 1807.01325

Maoz, D., Mannucci, F., Li, W., Filippenko, A. V., Valle, M. D., & Panagia, N. 2011, MNRAS, 412, 1508

Martig, M., Bournaud, F., Teyssier, R., & Dekel, A. 2009, ApJ, 707, 250, 0905.4669

Masters, K. L. et al. 2010, MNRAS, 405, 783

McKee, C. F., & Ostriker, J. P. 1977, ApJ, 218, 148

Mendel, J. T., Simard, L., Ellison, S. L., & Patton, D. R. 2013, MNRAS, 429, 2212

Mihos, J. C., & Hernquist, L. 1994a, ApJ, 431, L9

——. 1994b, ApJ, 431, L9

——. 1996, ApJ, 464, 641, astro-ph/9512099

Mo, H., Mao, S., & White, S. D. 1998, MNRAS, 295, 319

Moe, M., Arav, N., Bautista, M. A., & Korista, K. T. 2009, ApJ, 706, 525

Moore, B., Lake, G., & Katz, N. 1998, ApJ, 495, 139

Moutard, T. et al. 2016, A&A, 590, A103

Muzzin, A. et al. 2013, ApJ, 777, 18

Muzzin, A. et al. 2013, ApJ, 777, 18, 1303.4409

Naab, T., & Burkert, A. 2003, ApJ, 597, 893

Nogueira-Cavalcante, J., Gonçalves, T., Menéndez-Delmestre, K., de la Rosa, I., & Charbonnier, A. 2019, MNRAS, 484, 3022

Owers, M. S. et al. 2019a, ApJ, 873, 52, 1901.08185

——. 2019b, ApJ, 873, 52

Ownsworth, J. R., Conselice, C. J., Mundy, C. J., Mortlock, A., Hartley, W. G., Duncan, K., & Almaini, O. 2016, MNRAS, 461, 1112

Paccagnella, A., Vulcani, B., Poggianti, B. M., Moretti, A., Fritz, J., Gullieuszik, M., & Fasano, G. 2019, MNRAS, 482, 881

Paccagnella, A., Vulcani, B., Poggianti, B. M., Moretti, A., Fritz, J., Gullieuszik, M., & Fasano, G. 2019, MNRAS, 482, 881, 1805.11475

Pacifici, C. et al. 2016, ApJ, 832, 79, 1609.03572

Pawlik, M. M., McAlpine, S., Trayford, J. W., Wild, V., Bower, R., Crain, R. A., Schaller, M., & Schaye, J. 2019, Nature Astronomy, 3, 440, 1903.11050

Pawlik, M. M. et al. 2018, MNRAS, 477, 1708

Paxton, B., Bildsten, L., Dotter, A., Herwig, F., Lesaffre, P., & Timmes, F. 2011, ApJS, 192, 3

Paxton, B. et al. 2013, ApJS, 208, 4

——. 2015, ApJS, 220, 15

Peng, Y., Maiolino, R., & Cochrane, R. 2015, Nature, 521, 192

Peng, Y.-j. et al. 2010, ApJ, 721, 193

Pillepich, A. et al. 2018, MNRAS, 473, 4077

Planck Collaboration et al. 2016, A&A, 594, A13

Poggianti, B. M. et al. 2009, ApJ, 693, 112, 0811.0252

Poggianti, B. M., Smail, I., Dressler, A., Couch, W. J., Barger, A. J., Butcher, H., Ellis, R. S., & Oemler Jr, A. 1999, ApJ, 518, 576

Poggianti, B. M., & Wu, H. 2000, ApJ, 529, 157

Powell, L. C., Bournaud, F., Chapon, D., & Teyssier, R. 2013, MNRAS, 434, 1028, 1306.2641

Pracy, M. B., Couch, W. J., Blake, C., Bekki, K., Harrison, C., Colless, M., Kuntschner, H., & de Propris, R. 2005, MNRAS, 359, 1421, astro-ph/0503062

Pracy, M. B., Kuntschner, H., Couch, W. J., Blake, C., Bekki, K., & Briggs, F. 2009, MNRAS, 396, 1349, 0903.4719

Quai, S., Hani, M. H., Ellison, S. L., Patton, D. R., & Woo, J. 2021, MNRAS, 504, 1888, 2104.03327

Quintero, A. D. et al. 2004, ApJ, 602, 190

Rodríguez Montero, F., Davé, R., Wild, V., Anglés-Alcázar, D., & Narayanan, D. 2019, MNRAS, 490, 2139, 1907.12680

Rowlands, K. et al. 2018a, MNRAS, 480, 2544, 1807.06066

——. 2018b, MNRAS, 473, 1168, 1707.07989

Rowlands, K., Wild, V., Nesvadba, N., Sibthorpe, B., Mortier, A., Lehnert, M., & da Cunha, E. 2015, MNRAS, 448, 258, 1412.6090

Saintonge, A. et al. 2016, MNRAS, 462, 1749, 1607.05289

Sánchez, S. et al. 2012, Astronomy & Astrophysics, 538, A8

Sánchez-Blázquez, P. et al. 2006, MNRAS, 371, 703

Sanders, D. B., Soifer, B. T., Elias, J. H., Madore, B. F., Matthews, K., Neugebauer, G., & Scoville, N. Z. 1988, ApJ, 325, 74

Scannapieco, C., Tissera, P. B., White, S. D. M., & Springel, V. 2005, MNRAS, 364, 552, astro-ph/0505440

——. 2006, MNRAS, 371, 1125, astro-ph/0604524

Schaller, M., Gonnet, P., Draper, P. W., Chalk, A. B., Bower, R. G., Willis, J., & Hausammann, L. 2018, Astrophysics Source Code Library, ascl

Schawinski, K. et al. 2009, MNRAS, 396, 818

——. 2014, MNRAS, 440, 889

Schaye, J. et al. 2015, MNRAS, 446, 521

Schmidt, M. 1959, The Astrophysical Journal, 129, 243

Sedov, L. I. 1959, Similarity and Dimensional Methods in Mechanics

Shakura, N. I., & Sunyaev, R. A. 1973, A&A, 24, 337

Sharp, R. et al. 2015, Monthly Notices of the Royal Astronomical Society, 446, 1551

Shioya, Y., Bekki, K., & Couch, W. J. 2004, ApJ, 601, 654

Smercina, A. et al. 2018, ApJ, 855, 51, 1802.04798

Smethurst, R. J., Lintott, C. J., Bamford, S. P., Hart, R. E., Kruk, S. J., Masters, K. L., Nichol, R. C., & Simmons, B. D. 2017, MNRAS, 469, 3670

Snyder, G. F., Cox, T. J., Hayward, C. C., Hernquist, L., & Jonsson, P. 2011, ApJ, 741, 77

Socolovsky, M., Almaini, O., Hatch, N. A., Wild, V., Maltby, D. T., Hartley, W. G., & Simpson, C. 2018, MNRAS, 476, 1242

Speagle, J. S., Steinhardt, C. L., Capak, P. L., & Silverman, J. D. 2014, ApJS, 214, 15

Springel, V. 2005, MNRAS, 364, 1105

Springel, V., Di Matteo, T., & Hernquist, L. 2005, MNRAS, 361, 776

Straatman, C. M. et al. 2014, ApJ, 783, L14

Taylor, G. I. 1950, Proceedings of the Royal Society of London. Series A. Mathematical and Physical Sciences, 201, 159

Teyssier, R., Chapon, D., & Bournaud, F. 2010, The Astrophysical Journal Letters, 720, L149

Tran, K. H., Franx, M., Illingworth, G. D., van Dokkum, P., Kelson, D. D., & Magee, D. 2004a, ApJ, 609, 683

Tran, K.-V. H., Franx, M., Illingworth, G. D., van Dokkum, P., Kelson, D. D., & Magee, D. 2004b, ApJ, 609, 683

Trayford, J. W. et al. 2015, MNRAS, 452, 2879

Tremonti, C. A., Moustakas, J., & Diamond-Stanic, A. a. M. 2007, ApJ, 663, L77, 0706.0527

Trussler, J., Maiolino, R., Maraston, C., Peng, Y., Thomas, D., Goddard, D., & Lian, J. 2020, MNRAS, 491, 5406

van den Bosch, R. 2016, ApJ, 831, 1, 1606.01246

Vergani, D. et al. 2010, A&A, 509, A42, 0909.1968

Wang, Z. et al. 2004, The Astrophysical Journal Supplement Series, 154, 193

Weaver, J. et al. 2018, A&A, 614, A32, 1801.09691

Westfall, K. B. et al. 2019, AJ, 158, 231, 1901.00856

Whitaker, K. E., Kriek, M., Van Dokkum, P. G., Bezanson, R., Brammer, G., Franx, M., & Labbé, I. 2012, ApJ, 745, 1, 1112.0313

Wiersma, R. P. C., Schaye, J., & Smith, B. D. 2009, MNRAS, 393, 99, 0807.3748

Wild, V. et al. 2014, MNRAS, 440, 1880, 1401.7878

Wild, V., Almaini, O., Dunlop, J., Simpson, C., Rowlands, K., Bowler, R., Maltby, D., & McLure, R. 2016, MNRAS, 463, 832, 1608.00588

Wild, V., Heckman, T., & Charlot, S. 2010, MNRAS, 405, 933

Wild, V., Kauffmann, G., Heckman, T., Charlot, S., Lemson, G., Brinchmann, J., Reichard, T., & Pasquali, A. 2007, MNRAS, 381, 543

Wild, V. et al. 2020, MNRAS, 494, 529

Wild, V., Walcher, C. J., Johansson, P. H., Tresse, L., Charlot, S., Pollo, A., Le Fèvre, O., & De Ravel, L. 2009, MNRAS, 395, 144, 0810.5122

Williams, R. J., Quadri, R. F., Franx, M., Van Dokkum, P., & Labbé, I. 2009, ApJ, 691, 1879

Wong, O. I. et al. 2012, MNRAS, 420, 1684

Woosley, S. E., & Weaver, T. A. 1995, ApJS, 101, 181

Worthey, G., & Ottaviani, D. L. 1997, ApJS, 111, 377

Wu, P.-F. et al. 2018, ApJ, 868, 37

Yan, R. et al. 2016, AJ, 152, 197, 1607.08613

Yan, R., Newman, J. A., Faber, S., Konidaris, N., Koo, D., & Davis, M. 2006, ApJ, 648, 281

Yang, Y., Zabludoff, A. I., Zaritsky, D., & Mihos, J. C. 2008, ApJ, 688, 945, 0801.1190

Yano, M., Kriek, M., van der Wel, A., & Whitaker, K. E. 2016, ApJ, 817, L21, 1601.02629

Zabludoff, A. I., Zaritsky, D., Lin, H., Tucker, D., Hashimoto, Y., Shectman, S. A., Oemler, A., & Kirshner, R. P. 1996, ApJ, 466, 104, astro-ph/9512058

Zaritsky, D., Kennicutt Jr, R. C., & Huchra, J. P. 1994, ApJ, 420, 87